MESHLESS BOUNDARY PARTICLE METHODS FOR BOUNDARY INTEGRAL EQUATIONS AND MESHFREE PARTICLE METHODS FOR PLATES

by

Christopher Bard Davis

A dissertation submitted to the faculty of
the University of North Carolina at Charlotte
in partial fulfillment of the requirements
for the degree of Doctor of Philosophy in
Applied Mathematics

Charlotte

2011

Approved by:

Dr. Hae-Soo Oh

Dr. Michael Klibanov

Dr. Thomas R. Lucas

Dr. Scott Smith

ABSTRACT

CHRISTOPHER BARD DAVIS. Meshless boundary particle methods for boundary integral equations and meshfree particle methods for plates.
(Under the direction of DR. HAE-SOO OH)

For approximating the solution of partial differential equations (PDE), meshless methods have been introduced to alleviate the difficulties arising in mesh generation using the conventional Finite Element Method (FEM). Many meshless methods introduced lack the Kronecker delta property making them inefficient in handling essential boundary conditions. Oh et al. developed several meshfree shape functions that have the Kronecker delta property. Boundary Element Methods (BEM) solve a boundary integral equation (BIE) which is equivalent to the PDE, thus reducing the dimensionality of the problem by one and the amount of computation when compared to FEM.

In this dissertation, three meshless collocation based boundary element methods are introduced: meshfree reproducing polynomial boundary particle method (RPBPM), patch-wise RPBPM, and patch-wise reproducing singularity particle method (RSBPM). They are applied to the Laplace equation for convex and non-convex domains in two and three dimensions for problems with and without domain singularities.

Electromagnetic wave propagation through photonic crystals is governed by Maxwell's equations in the frequency domain. Under certain conditions, it can be shown that the wave propagation is also governed by Helmholtz equation. Patch-wise RPBPM is applied to the two dimensional Helmholtz equation and used to model electromagnetic wave propagation though lattices of photonic crystals.

For thin plate problems, using the Kirchoff hypothesis, the three dimensional elasticity equations are reduced to a fourth order PDE for the vertical displacement. Conventional FEM has difficulties in solving this because the basis functions are re-

quired to have continuous partial derivatives. Suggestions are to use Hermite based elements which are difficult to implement. Using a partition of unity, some special shape functions are developed for thin plates with simple support or clamped boundary conditions. This meshless method for thin plates is then tested and the results are reported.

DEDICATION

To my wife, Beth.

ACKNOWLEDGMENTS

Faculty and family members have helped me complete this dissertation. I would like to express my sincere gratitude to these individuals for their support and assistance

I am heartily thankful to my adviser, Hae Soo Oh, whose encouragement, supervision and support from the beginning level enabled me to develop an understanding of meshless methods. Without his guidance this dissertation would not be possible.

I am also very grateful to the members of my committee. I would like to express special thanks to Dr. Klibanov for teaching me the beauty of partial differential equations and Sobolev spaces. I am also grateful to Dr. Lucas and Dr. Smith for generously taking time out of their busy schedules to help me improve my work.

I am thankful to my wife and parents for all the helpful suggestions and having patience with me as I completed my graduate studies.

TABLE OF CONTENTS

LIST OF FIGURES

LIST OF TABLES

CHAPTER 1: INTRODUCTION

Partial differential equations (PDE) can be used to model many different physical phenomena such as stress inside a body, propagation of waves, and much more. They are powerful tools in physics and engineering. Solving them analytically can be very difficult or impossible; hence, finding reasonable approximate solutions is a practical alternative.

When solving a PDE numerically, there are many methods to choose from such as the Finite Element Method (FEM), the Boundary Element Method (BEM), and much, much more. FEM uses a variational form of the PDE to find a weak solution over some approximation space. BEM uses an equivalent boundary integral equation (BIE) to find an approximate solution. Each method has its advantages and its drawbacks. FEM requires a mesh throughout the domain to be constructed which is an expensive and difficult task to do. BEM has the advantage that it only requires a mesh to be constructed throughout the boundary of the domain, however BEM also requires the use of a fundamental solution to the PDE which does not exist in some cases. To help alleviate the difficulties arising from mesh generation, meshless methods have been introduced.

Meshless methods have advantages over conventional FEM. However, these methods also have some difficulties such as inefficiency in handling essential boundary conditions, large matrix condition numbers and so on. Recently, Oh et al. ([41],[42],[43], [44],[45],[46],[47]) introduced various meshless methods that alleviate these difficulties. Specifically, the following have been introduced:

1. Highly regular (piecewise polynomial) reproducing polynomial particle(RPP) shape functions corresponding to uniformly spaced particles ([45]).

2. Constructions of various piecewise polynomial partition of unity (PU) functions: convolution PU functions, almost everywhere PU functions, and generalized product PU functions ([41],[42],[44]).
3. Using these partitions of unity, patch-wise reproducing polynomial particle shape functions are constructed that correspond to patch-wise uniformly (or non-uniformly) spaced particles ([46]).
4. Reproducing singularity particle (RSP) shape functions that can effectively handle elliptic boundary value problems containing singularities ([43],[47]).

It is important to note that almost all particle shape functions mentioned above satisfy the Kronecker delta property. In this dissertation, using these shape functions, two different reproducing polynomial boundary particle methods (RPBPM) and a reproducing singularity boundary particle method (RSPBM) are proposed to solve BIEs of elliptic problems with or without singularities.

1. Meshfree RPBPM that uses meshfree RPP shape functions.
2. Patch-wise RPBPM in which patch-wise RPP shape functions are assigned to each particle on the boundary.
3. Patch-wise RSBPM that uses patch-wise RSP shape functions for BIE containing singularities.

Electromagnetic wave propagation through photonic crystals is governed by Maxwell's equations in the frequency domain. In considering electromagnetic wave propagation, we will consider transverse magnetic (TM) waves which means in the direction of propagation of the wave there will be no magnetic field, i.e. only magnetic field components which are perpendicular to the direction of propagation will be there. We could similarly consider transverse electric (TE) waves, which are the same as TM waves but with the roles of the electric field and the magnetic field swapped. It can be shown that TM and TE wave propagation is governed by Helmholtz equation. Patch-wise RPBPM is applied to the two dimensional Helmholtz equation and used

to model electromagnetic (TM) wave propagation though various lattices of photonic crystals.

Another application of RPP shape functions is the elasticity problem for a thin plates. A large number of structural components in engineering can be classified as plates. Typical examples in civil engineering structures are floor and foundation slabs, lock-gates, thin retaining walls, bridge decks, and slab bridges. Plates are indispensable in ship building, automobile, and aerospace industries. If a plate is thin, by the Kirchoff hypothesis, the three dimensional elasticity equations for the displacements (u, v, w) can be reduced to a scalar two dimensional fourth order elliptic equation for w. Thus, the shape functions for FEM are required to have continuous partial derivatives. ([8],[11]) suggest using the Argyris and Bell triangles, or the Bogner-Fox-Schmit rectangle which are $\mathcal{C}^1$ continuous finite elements. These Hermite-type finite elements are difficult to implement. We will show the effectiveness of the RPP shape functions in the context of the classical plate theory governed by the Kirchoff hypothesis.

After introducing definitions and terminologies in chapter 2, discussion about derivation of the boundary integral equation and various boundary element methods are introduced in chapter 3. Chapters 4 and 5 introduce meshless boundary element methods for the two and three dimensional Laplace equation respectively. Chapter 6 demonstrates a variation of patch-wise RPBPM to Helmholtz equation. Chapter 7 introduces the RPPM for thin plates. Chapter 8 is the conclusions.

CHAPTER 2: PRELIMINARIES

Throughout this dissertation, $\alpha, \beta \in \mathbb{Z}^d$ are multi indices and $x = ({}^1x, {}^2x, \ldots, {}^dx)$, $x_j = ({}^1x_j, {}^2x_j, \ldots, {}^dx_j)$ denote points in $\mathbb{R}^d$. However, without confusion, we also use the conventional notation for the points in $\mathbb{R}^d$ or $\mathbb{Z}^d$ as $x = (x_1, x_2, \ldots, x_d)$ and $\alpha = (\alpha_1, \alpha_2, \ldots, \alpha_d)$. By $\alpha \leq \beta$, we mean $\alpha_1 \leq \beta_1, ..., \alpha_d \leq \beta_d$. We also use the following notations: $(x - x_j)^\alpha := ({}^1x - {}^1x_j)^{\alpha_1} ... ({}^dx - {}^dx_j)^{\alpha_d}$, $|\alpha| := \alpha_1 + \alpha_2 + \cdots + \alpha_d$. Let Ω be a domain in $\mathbb{R}^d$. For any nonnegative integer m, $\mathcal{C}^m(\Omega)$ denotes the space of all functions ϕ such that ϕ together with all their derivatives $D^\alpha\phi$ of orders $|\alpha| \leq m$, are continuous on $\overline{\Omega}$. The support of ϕ is defined by the following:

$$\text{supp}(\phi) = \overline{\{x \in \Omega : \phi(x) \neq 0\}}.$$

In the following, a function $\phi \in \mathcal{C}^m(\Omega)$ is said to be a $\mathcal{C}^m$- function.

A family $\{U_k : k \in \mathcal{D}\}$ of open subsets of $\mathbb{R}^d$ is said to be a point finite open covering of $\Omega \subseteq \mathbb{R}^d$ if there is M such that any $x \in \Omega$ lies in at most M of the open sets U_k and $\Omega \subseteq \bigcup_k U_k$.

For a point finite open covering $\{U_k : k \in \mathcal{D}\}$ of a domain Ω, suppose there is a family $\{\psi_k : k \in \mathcal{D}\}$ of Lipschitz functions on Ω satisfying the following conditions:

1. For $k \in \mathcal{D}$, $0 \leq \psi_k(x) \leq 1, \quad x \in \mathbb{R}^d$.
2. The support of ψ_k is contained in $\overline{U}_k$, for each $k \in \mathcal{D}$.
3. $\sum_{k \in \mathcal{D}} \psi_k(x) = 1$ for each $x \in \Omega$.

Then $\{\psi_k : k \in \mathcal{D}\}$ is called a partition of unity (PU) subordinate to the covering $\{U_k : k \in \Lambda\}$. The covering sets $\{U_k\}$ are called patches.

By almost everywhere partition of unity, we mean $\{\psi_k : k \in \mathcal{D}\}$ such that the condition 3 of a partition of unity is not satisfied only at finitely many points (2D)

or lines (3D) on a part of the boundary.

A weight function (or window function) is a non-negative continuous function with compact support and is denoted by $w(x)$. Consider the following conical window function: For $x \in \mathbb{R}$,

$$w(x) = \begin{cases} (1-x^2)^l, & |x| \le 1, \\ 0, & |x| > 1, \end{cases} \tag{2.1}$$

where l is an integer. Then $w(x)$ is a $\mathcal{C}^{l-1}$-function. In $\mathbb{R}^d$, the weight function $w(x)$ can be constructed from a one-dimensional weight function as $w(x) = \prod_{i=1}^{d} w(x_i)$, where $x = (x_1, \ldots, x_d)$.

Here, we use the normalized window function defined by

$$w_\delta^l(x) = Aw\left(\frac{x}{\delta}\right), \tag{2.2}$$

where $A = [(2l+1)!]/[2^{2l+1}(l!)^2\delta]$ ([16]) is the constant that makes $\int_{\mathbb{R}} w_\delta^l(x)dx = 1$.

2.1 Meshfree Particle Shape Functions

Adopting the terminologies and notations of ([4],[29],[30],[31],[23]), we have the following: For $j = (j_1, j_2, \ldots, j_d) \in \mathbb{Z}^d$, and the mesh size $0 < h \le 1$, let

$$x_j^h = (j_1 h, \ldots, j_d h) = hj.$$

Then the points x_j^h are called uniformly distributed particles. Let ϕ be a continuous function with compact support that contains the origin 0. Then the particle shape functions associated to the uniformly distributed particles are defined by

$$\phi_j^h(x) = \phi(\frac{x - jh}{h}) = \phi(\frac{x_1 - j_1 h}{h}, \ldots, \frac{x_d - j_d h}{h}),$$

for $j \in \mathbb{Z}^d$ and $0 < h \le 1$. Then, these particle shape functions are translation invariant in the sense that

$$x_{i+j}^h = x_i^h + x_j^h, \quad \phi_j^h(x - ih) = \phi_{i+j}^h(x).$$

In this dissertation, we assume that the meshfree particle shape functions are

translation invariant on the uniformly distributed particles, unless stated otherwise. Moreover, using a partition of unity on a background mesh of Ω, particle shape functions associated with non-uniformly distributed particles are constructed in chapters 4 and 5.

Without loss of generality, in the construction of meshfree particle shape functions, we assume that $h = 1$ and hence $\phi_j^h(x) = \phi(x - j)$. Let Λ be an index set and Ω denote a bounded domain in $\mathbb{R}^d$. Let $\{x_j : j \in \Lambda\}$ be a set of uniformly (or non-uniformly) distributed points in $\mathbb{R}^d$. These are what we call particles.

Let k be a nonnegative integer. Then the functions $\phi_j(x)$ corresponding to the particles $x_j, j \in \Lambda$, are called the Reproducing Kernel Particle (RKP) shape functions with the reproducing property of order k (or simply, "of reproducing order k") if and only if it satisfies the following condition: for $x \in \Omega \subset \mathbb{R}^d$,

$$\sum_{j\in\Lambda}(x_j)^\alpha \phi_j(x) = x^\alpha, \text{ and for } 0 \le |\alpha| \le k, |\alpha| = \alpha_1 + \cdots + \alpha_d, \tag{2.3}$$

([4],[16],[22],[29]).

By applying a similar argument to ([4],[16]), one can show that (2.3) is equivalent to

$$\sum_{j\in\Lambda}(x - x_j)^\beta \phi_j(x) = \delta^0_{|\beta|}, \qquad \text{for } 0 \le |\beta| \le k \text{ and } x \in \mathbb{R}^d. \tag{2.4}$$

This characterization of meshfree shape functions has no direct relation with the window functions. Using (2.4), Oh et al.([45]) constructed piecewise polynomial meshfree particle shape functions that have the polynomial reproducing property. These meshfree shape functions constructed without using window function are called Reproducing Polynomial Particle(RPP) shape functions. One of the salient features of RPP shape functions is that they satisfy the Kronecker delta property ([42],[44],[45],[46],[47])

We refer to [45] for various closed form RPP shape functions with high polynomial reproducing order and high order of regularity. For example, 1-dimensional $\mathcal{C}^0$-RPP

shape functions, $\phi_j(x), j \in \mathbb{Z}$, of reproducing order 3 can be constructed as follows: Suppose the particles x_j are the integer points and $\phi_j(x) = \phi(x-j)$ for $j \in \mathbb{Z}$. Then, from (2.4), we have a system of functional equations,

$$\begin{bmatrix} 1 & 1 & 1 & 1 \\ (x+1) & x & (x-1) & (x-2) \\ (x+1)^2 & x^2 & (x-1)^2 & (x-2)^2 \\ (x+1)^3 & x^3 & (x-1)^3 & (x-2)^3 \end{bmatrix} \begin{bmatrix} \hat{\phi}(x+1) \\ \hat{\phi}(x) \\ \hat{\phi}(x-1) \\ \hat{\phi}(x-2) \end{bmatrix} = \begin{bmatrix} 1 \\ 0 \\ 0 \\ 0 \end{bmatrix} \text{ for } x \in (0,1).$$

Now using the solutions of this system, we construct the basic RPP shape function $\phi(x)$, from which other particle shape functions are obtained by translations, in the following way:

$$\begin{cases} \phi(x)|_{(-2,-1)} &= \hat{\phi}(x+1) \text{ shifted by } +1, \\ \phi(x)|_{(-1,0)} &= \hat{\phi}(x+1) \text{ shifted by } -1, \\ \phi(x)|_{(0,1)} &= \hat{\phi}(x), \\ \phi(x)|_{(1,2)} &= \hat{\phi}(x-2) \text{ shifted by } -2, \\ \phi(x) &= 0 \text{ for } x \notin [-2,2]. \end{cases}$$

Connecting these pieces together at $-2, -1, 0, 1, 2$, we have the following piecewise polynomial $\mathcal{C}^0$-RPP shape function defined by

$$\phi_{([-2,2];0;3)}(x) = \begin{cases} \frac{1}{6}(x+1)(x+2)(x+3) & x \in [-2,-1] \\ -\frac{1}{2}(x-1)(x+1)(x+2) & x \in [-1,0] \\ \frac{1}{2}(x-2)(x-1)(x+1) & x \in [0,1] \\ -\frac{1}{6}(x-3)(x-2)(x-1) & x \in [1,2] \\ 0 & x \notin [-2,2], \end{cases} \tag{2.5}$$

where the subscripts $[-2,2], 0, 3$, respectively, stand for the support, the regularity, and the order of reproducing polynomial property of $\phi_{([-2,2];0;3)}$.

By reducing the polynomial reproducing order, we can increase the order of regularity. For instance, from $\phi_{([-2,2];0;3)}(x)$, we construct the $\mathcal{C}^1$-RPP shape function $\phi_{([-2,2];1;2)}(x)$

$$\phi_{([-2,2];1;2)}(x) = \begin{cases} \frac{1}{2}(x+1)(x+2)^2 & x \in [-2,-1] \\ -\frac{1}{2}(x+1)(3x^2+2x-2) & x \in [-1,0] \\ \frac{1}{2}(x-1)(3x^2-2x-2) & x \in [0,1] \\ -\frac{1}{2}(x-2)^2(x-1) & x \in [1,2] \\ 0 & x \notin [-2,2] \end{cases} \tag{2.6}$$

We refer to [45] for the proof. Let us note that the higher dimensional piecewise polynomial RPP shape functions constructed by solving the system (2.4) are actually the same as the tensor product of 1-dimensional RPP shape functions.

2.2 One-Dimensional Partition of Unity Functions with Flat-Top

In this section, we briefly review one dimensional partition of unity with flat-top. For details of this construction, we refer to ([44]), in which we showed that PU functions with flat-top lead to a small matrix condition number.

We reserve the small real number δ, usually, $0.01 \leq \delta \leq 0.1$, for the width of non flat-top part of the PU functions with flat-top.

For any positive integer n, $\mathcal{C}^{n-1}$- piecewise polynomial basic PU functions are constructed as follows: For integers $n \geq 1$, we define a piecewise polynomial function by

$$\phi_{g_n}^{(pp)}(x) = \begin{cases} \phi_{g_n}^L(x) := (1+x)^n g_n(x) & \text{if} \quad x \in [-1,0] \\ \phi_{g_n}^R(x) := (1-x)^n g_n(-x) & \text{if} \quad x \in [0,1] \\ 0 & \text{if} \quad |x| \geq 1, \end{cases} \tag{2.7}$$

where $g_n(x) = a_0^{(n)} + a_1^{(n)}(-x) + a_2^{(n)}(-x)^2 + \cdots + a_{n-1}^{(n)}(-x)^{n-1}$ whose coefficients are

inductively constructed by the following recursion formula:

$$a_k^{(n)} = \begin{cases} 1, & \text{if} \quad k = 0 \\ \sum_{j=0}^{k} a_j^{(n-1)}, & \text{if} \quad 0 < k \leq n-2, \\ 2(a_{n-2}^{(n)}), & \text{if} \quad k = n-1. \end{cases} \tag{2.8}$$

For example, from the recurrence relation (2.8), we have

$$g_1(x) = 1; \quad g_2(x) = 1 - 2x; \quad g_3(x) = 1 - 3x + 6x^2.$$

Then, $\phi_{g_n}^{(pp)}$ has the following properties whose proofs can be found in ([44]).

- $\phi_{g_n}^{(pp)}(x) + \phi_{g_n}^{(pp)}(x-1) = 1$ for all $x \in [0,1]$. Hence, $\{\phi_{g_n}^{(pp)}(x-j) | j \in \mathbb{Z}\}$ is a partition of unity on $\mathbb{R}$.
- $\phi_{g_n}^{(pp)}(x)$ is a $\mathcal{C}^{n-1}$- function.
- The gradient of the scaled basic PU function is bounded as follows:

$$\frac{d}{dx}\left[\phi_{g_n}^{(pp)}(\frac{x}{2\delta})\right] \leq \frac{C}{\delta}. \tag{2.9}$$

  Note that the constant C is ≤ 0.9 for $n \leq 3$.

2.3 Generalized Two Dimensional Product Partition of Unity with Flat-Top

Using the basic PU function $\phi_{g_n}^{(pp)}$ defined by (2.7), we construct a $\mathcal{C}^{n-1}$- PU function with flat-top whose support is $[a-\delta, b+\delta]$ with $(a+\delta) < (b-\delta)$ in a closed form as follows:

$$\psi_{[a,b]}^{(\delta,n-1)}(x) = \begin{cases} \phi_{g_n}^{L}(\frac{x-(a+\delta)}{2\delta}) & \text{if} \quad x \in [a-\delta, a+\delta] \\ 1 & \text{if} \quad x \in [a+\delta, b-\delta] \\ \phi_{g_n}^{R}(\frac{x-(b-\delta)}{2\delta}) & \text{if} \quad x \in [b-\delta, b+\delta] \\ 0 & \text{if} \quad x \notin [a-\delta, b+\delta]. \end{cases} \tag{2.10}$$

Here, in order to make a PU function have a flat-top, we assume $\delta \leq (b-a)/3$. Let us note that $\psi_{[a,b]}^{(\delta,n-1)}(x)$ is actually the convolution, $\chi_{[a,b]}(x) * w_\delta^{n-1}(x)$, of the characteristic function $\chi_{[a,b]}$ and the scaled window function w_δ^{n-1}, defined by (2.2)

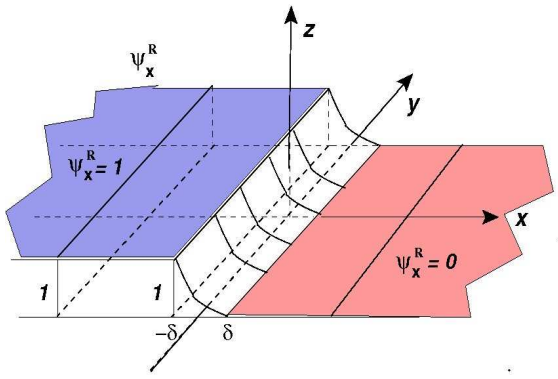

Figure 2.1: Sketch of Ψ_x^R.

(Corollary 3.1 of [44]).

Since the two functions $\phi_{g_n}^R, \phi_{g_n}^L$, defined by (2.7), satisfy the following relation:

$$\phi_{g_n}^R(\xi) + \phi_{g_n}^L(\xi - 1) = 1, \text{ for } \xi \in [0, 1], \tag{2.11}$$

if $\varphi : [-\delta, \delta] \to [0, 1]$ is defined by

$$\varphi(x) = (x + \delta)/(2\delta),$$

then we have

$$\phi_{g_n}^R(\varphi(x)) + \phi_{g_n}^L(\varphi(x) - 1) = 1, \text{ for } x \in [-\delta, \delta].$$

Using the latter equation gives two basic one-dimensional $\mathcal{C}^{n-1}$ functions

$$\psi_0^R(x) = \begin{cases} 1 & \text{if } \ x \le -\delta \\ \phi_{g_n}^R(\frac{x+\delta)}{2\delta}) & \text{if } \ x \in [-\delta, \delta] \\ 0 & \text{if } \ x \ge \delta, \end{cases} \tag{2.12}$$

$$1 - \psi_0^R(x) = \psi_0^L(x) = \begin{cases} \phi_{g_n}^L(\frac{x-\delta}{2\delta}) & \text{if } \ x \in [-\delta, \delta] \\ 1 & \text{if } \ x \ge \delta, \\ 0 & \text{if } \ x \le -\delta. \end{cases} \tag{2.13}$$

such that

$$0 \le \psi_0^L(x), \psi_0^R(x) \le 1, \quad \psi_0^R(x) + \psi_0^L(x) = 1, \text{ for all } x \in \mathbb{R}.$$

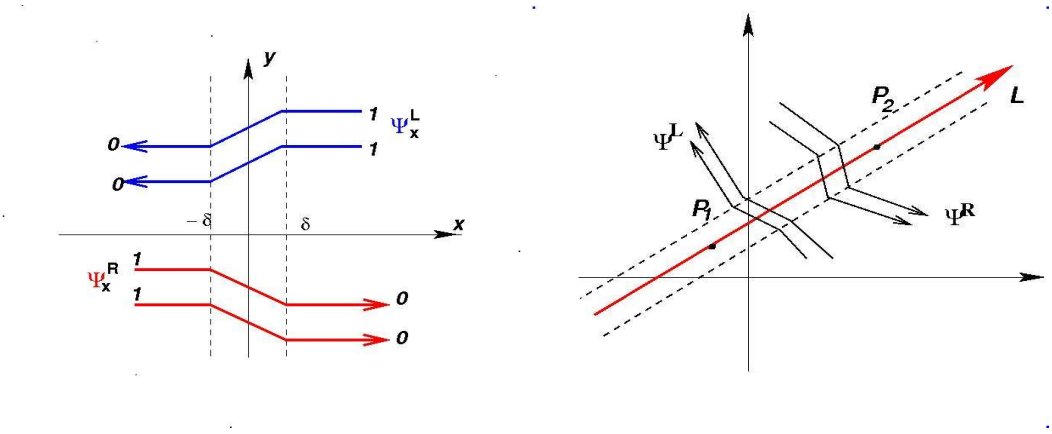

Figure 2.2: Schematic diagram of basic PU functions, $\Psi_x^R = \Psi_{x=0}$ and $\Psi_x^L = \Psi_{x=0}^*$ in two dimensions(Left).Schematic diagram of transformed PU functions about the line L, Ψ^R and Ψ^L in two dimensions(Right).

To extend these PU functions (2.12) and (2.13) to basic two-dimensional $\mathcal{C}^{n-1}$-PU functions on $\mathbb{R}^2$, condiser the following. Suppose $\overleftrightarrow{P_1P_2}$ is a straight line connecting two points $P_1(x_1, y_1)$ and $P_2(x_2, y_2)$ with $x_1 \leq x_2$ such that $y_1 < y_2$ if $x_1 = x_2$. Then the angle between the positive x-axis and $\overleftrightarrow{P_1P_2}$ is determined by the following formula.

$$\begin{cases} \theta = \tan^{-1}(\dfrac{y_2 - y_1}{x_2 - x_1}), & \text{if } x_2 \neq x_1, \\ \theta = \pi/2, & \text{if } x_2 = x_1. \end{cases} \tag{2.14}$$

Let $T_{P_1P_2}$ be an affine transformation on $\mathbb{R}^2$ that transforms the straight line $\overleftrightarrow{P_1P_2}$ onto the y-axis with $T(P_1) < T(P_2)$ defined by

$$T_{P_1P_2}(x, y) = \begin{bmatrix} \cos(\pi/2 - \theta) & -\sin(\pi/2 - \theta) \\ \sin(\pi/2 - \theta) & \cos(\pi/2 - \theta) \end{bmatrix} \begin{bmatrix} x - x_1 \\ y - y_1 \end{bmatrix} = (\hat{x}, \hat{y}) \tag{2.15}$$

Then we define two PU functions by

$$\Psi_{P_1P_2}(x, y) \;=\; \psi_0^R(\hat{x}), \quad \Psi^\star_{P_1P_2}(x, y) = \psi_0^L(\hat{x}) = 1 - \Psi_{P_1P_2}(x, y), \tag{2.16}$$

that satisfy

$$\Psi^\star_{P_1P_2}(x, y) + \Psi_{P_1P_2}(x, y) = 1, \text{ for all } (x, y) \in \mathbb{R}^2.$$

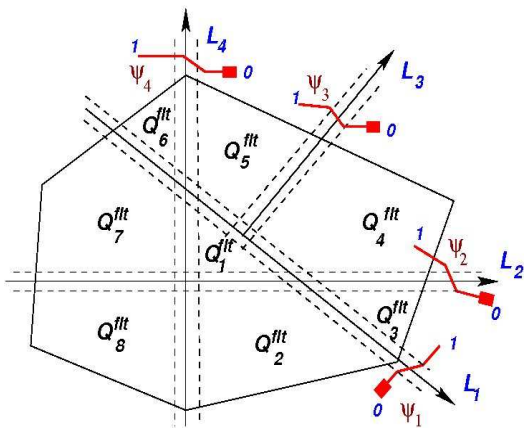

Figure 2.3: Domain Ω is partitioned into eight patches $Q_1, \ldots, Q_8$ and the flat-top parts of corresponding product PU functions are denoted by $Q_1^{flt}, \ldots, Q_8^{flt}$ respectively.

For example, if the line $\overleftrightarrow{P_1P_2}$ is the y-axis, then the two-dimensional $\mathcal{C}^{n-1}$ functions are

$$\Psi_{x=0}(x,y) = \psi_0^R(x) \text{ and } \Psi^\star_{x=0}(x,y) = \psi_0^L(x), \text{ for all } (x,y) \in \mathbb{R}^2. \tag{2.17}$$

In other words, two step-like-functions are the composition of the coordinate projection, $(x,y) \longrightarrow x$, and ψ_0^R, ψ_0^L, respectively. The graph of $\Psi_{x=0}$ (simply denoted by Ψ_x^R) is sketched in Figure 2.1. The schematic diagram for $\Psi_{x=0}$ and $\Psi^\star_{x=0}$ is shown in Figure 2.2. That is,

$$\begin{cases} \Psi^\star_{x=0}(x,y) = 1 & \text{if } x \geq \delta \\ \Psi^\star_{x=0}(x,y) = 0 & \text{if } x \leq -\delta \\ 0 \leq \Psi^\star_{x=0}(x,y) \leq 1 & \text{if } |x| \leq \delta \end{cases} \text{ and } \begin{cases} \Psi_{x=0}(x,y) = 0 & \text{if } x \geq \delta \\ \Psi_{x=0}(x,y) = 1 & \text{if } x \leq -\delta \\ 0 \leq \Psi_{x=0}(x,y) \leq 1 & \text{if } |x| \leq \delta. \end{cases} \tag{2.18}$$

2.4 Generalized Product Partition of Unity

Suppose the given domain Ω is partitioned into patches $Q_j, j = 1, \ldots, n$ (background mesh) by lines and rays as shown in Figure 2.3. Then the closed form partition of unity functions $\Psi_j^P, j = 1, \ldots, n$ with flat-top, called the generalized product partition of unity, are introduced in [48]. In the following, we briefly review the generalized product partition of unity for those patches shown in Figure 2.3. Here δ is a small

number, usually in $[0.01, 0.1]$ that depends on the sizes of patches.

1. The triangular patch Q_1 of Figure 2.3 is surrounded by lines L_1, L_2, L_4. Using (2.16), the step-like-basic PU functions of (2.17) on $\mathbb{R}^2$ are transformed onto lines L_1, L_2, L_4 :

$$\Psi_{L_1}, 1-\Psi_{L_1} := \Psi^{\star}_{L_1}; \Psi_{L_2}, 1-\Psi_{L_2} := \Psi^{\star}_{L_2}; \Psi_{L_4}, 1-\Psi_{L_4} := \Psi^{\star}_{L_4}.; \qquad (2.19)$$

   to get three pairs of PU functions.

2. The flat-top part of each patch Q_j that is outside the dotted lines is denoted by Q_j^{flt} on which only one of each pairs of basic PU functions is one.

3. Among the six PU functions in (2.19) related to lines enclosing Q_1, those which are one on Q_1^{flt} are $\Psi^{\star}_{L_1}, \Psi_{L_2}$, and $\Psi^{\star}_{L_4}$. A closed form PU function corresponding to the patch Q_1 is the product of these basic PU functions, that is, $\Psi_1^P = \Psi^{\star}_{L_1} \cdot \Psi_{L_2} \cdot \Psi^{\star}_{L_4}$.

4. Similarly, the closed form PU functions with wide flat-top corresponding to patches $Q_j, j = 2, \ldots, 8$, respectively, are

$$\begin{aligned}
\Psi_2^P &= \Psi^{\star}_{L_1} \cdot \Psi^{\star}_{L_2} \cdot \Psi^{\star}_{L_4}, \quad \Psi_3^P = \Psi_{L_1} \cdot \Psi^{\star}_{L_2}, \quad \Psi_4^P = \Psi_{L_1} \cdot \Psi_{L_2} \cdot \Psi^{\star}_{L_3}, \\
\Psi_5^P &= \Psi_{L_1} \cdot \Psi_{L_3} \cdot \Psi^{\star}_{L_4}, \quad \Psi_6^P = \Psi_{L_1} \cdot \Psi_{L_4}, \quad \Psi_7^P = \Psi^{\star}_{L_1} \cdot \Psi_{L_2} \cdot \Psi_{L_4}, \\
\Psi_8^P &= \Psi^{\star}_{L_2} \cdot \Psi_{L_4}.
\end{aligned}$$

   such that

$$\sum_{j=1}^{8} \Psi_j^P(x, y) = 1, \text{ for all } (x, y) \in \Omega.$$

   These functions with flat-top are called the generalized product PU functions (we refer to [48] for the proof and the constructions for general cases).

If a patch Q_j is a rectangle $[a, b] \times [c, d]$, then Ψ_j^P is the tensor product $\psi^{(\delta,n-1)}_{[a,b]} \times \psi^{(\delta,n-1)}_{[c,d]}$, of one-dimensional functions defined by (2.10).

CHAPTER 3: BOUNDARY ELEMENT METHODS

3.1 Derivation of the Boundary Integral Equation for Laplace Equation

In this section, we will derive the boundary integral equation (BIE) used to approximate the solution of the Laplace equation in a bounded domain Ω in $\mathbb{R}^2$ or $\mathbb{R}^3$. Let u be the solution of Laplace's equation

$$\Delta u = 0 \text{ in } \Omega \subset \mathbb{R}^d \tag{3.1}$$

where $d = 2, 3$. Let $G(x, P)$ the fundamental solution of the Laplace equation that solves

$$-\Delta G(x, P) = \delta(x - P). \tag{3.2}$$

Here $x = (x, y), P = (\xi, \eta)$, if $d = 2$ and $x = (x, y, z), P = (\xi, \eta, \zeta)$, if $d = 3$ and $\delta(x - P)$ is the Dirac delta function centered at P. By multiplying (3.1) by $G(x, P)$ and multiplying (3.2) by $u(x)$, adding and then integrating over Ω with respect to x we have:

$$\int_\Omega \Delta u(x) G(x, P) dx - \int_\Omega \Delta G(x, P) u(x) dx = \int_\Omega \delta(x - P) u(x) dx.$$

Then, using Green's second identity, and assuming that $P \in \Omega$ for $\Gamma = \partial\Omega$ we have the following BIE:

$$u(P) = \int_\Gamma \frac{\partial u(x)}{\partial n} G(x, P) ds(x) - \int_\Gamma \frac{\partial G(x, P)}{\partial n} u(x) ds(x) \quad \text{for } P \in \Omega. \tag{3.3}$$

Now, by using the mean value theorem, we find the following BIE for any point $P \in \mathbb{R}^d$ to be:

$$c(P)u(P) + \int_\Gamma u(x) \frac{\partial G(x, P)}{\partial n} ds(x) = \int_\Gamma \frac{\partial u(x)}{\partial n} G(x, P) ds(x). \tag{3.4}$$

When $d = 2$ we have

$$G(x, P) \;=\; -\frac{1}{2\pi} \log r, \quad r = \sqrt{(\xi - x)^2 + (\eta - y)^2}$$

$$c(P) = \begin{cases} 0 & \text{if } P \text{ is outside } \Omega \\ 1 & \text{if } P \in \Omega \\ \frac{1}{2} & \text{if } P \in \Gamma \text{ and } \Gamma \text{ is smooth at } P \\ \frac{\alpha}{2\pi} & \text{if } P \in \Gamma \text{ and } \Gamma \text{ is not smooth at } P \end{cases} \tag{3.5}$$

where α is the internal angle of Ω at P. When $d = 3$ we have

$$G(x, P) = \frac{1}{4\pi r}, \quad r = \sqrt{(\xi - x)^2 + (\eta - y)^2 + (\zeta - z)^2}$$

$$c(P) = \begin{cases} 0 & \text{if } P \text{ is outside } \Omega \\ 1 & \text{if } P \in \Omega \\ \frac{1}{2} & \text{if } P \in \Gamma \text{ and } \Gamma \text{ is smooth at } P \\ \frac{\alpha}{4\pi} & \text{if } P \in \Gamma \text{ and } \Gamma \text{ is not smooth at } P \end{cases} \tag{3.6}$$

where α is the innner solid angle of Ω at P (refer to [17] for proof).

In (3.4), the unknowns are u and $\frac{\partial u}{\partial n}$ on the boundary and $u(P)$ for $P \in \mathbb{R}^d$. If $P \in \Omega$, then (3.4) has no singular integral. However, if $P \in \partial\Omega$ and $\partial\Omega$ is smooth at P, then (3.4) becomes:

$$\frac{1}{2}u(P) + \int_\Gamma u(x)\frac{\partial G(x, P)}{\partial n}ds(x) = \int_\Gamma \frac{\partial u(x)}{\partial n}G(x, P)ds(x) \tag{3.7}$$

which contains a singular integral that diverges. For this integral, if $d = 2$ we use the Cauchy principal value (CPV) formula to assign a finite definite value, if $d = 3$ we use Haddamard finite part integral to assign a finite definite value.

Using (3.7), $u|_\Gamma$ and $\frac{\partial u}{\partial n}|_\Gamma$ can be determined. Together with these boundary values, one can use (3.4) to get the value of u at all points in Ω (the solution of Laplace's equation). In other words, first, we solve for the boundary data (u and its normal derivative along the boundary Γ). Then, the volume data can be found through post processing.

Numerical methods to compute $u|_\Gamma$ and $\frac{\partial u}{\partial n}|_\Gamma$ are called boundary element methods (BEM) which obviously, have advantages over the finite element method whenever

the fundamental solution could be found in a simple form. However, fundamental solutions are not known except for some special differential equations, whereas the finite element method does not have such restrictions.

To solve a BIE for the Laplace equation, there are essentially three categories of Boundary Element Methods to choose from: the Nyström method, the Collocation method, and the Galerkin method.

3.2 Nyström Method

The Nyström method, also known as the quadrature method, replaces the integrations by a quadrature formula. This means that if we have a quadrature rule such that

$$\int_\Gamma f(x)ds(x) \approx \sum_{k=1}^{N_q} w_k f(x_k),$$

where w_k is the weight and x_k is the abscissa $k = 1, \ldots, N_q$. Then (3.7) would become

$$\frac{1}{2}u(P) + \sum_{k=1}^{N_q} w_k u(x_k)\frac{\partial G(x_k, P)}{\partial n} = \sum_{k=1}^{N_q} w_k \frac{\partial u(x_k)}{\partial n} G(x_k, P). \tag{3.8}$$

One may obtain a linear system by letting $P = x_j$ where $j = 1, \ldots, N_q$. A benefit of using the Nyström method is that the entries of the coefficient matrices only contain function evaluations of the fundamental solution. Compared with the other two methods, this is much less computation for each entry. However, in practice, large systems must be solved. The Nyström method heavily relies on the quadrature formula and does not require any basis function. For this last reason, we do not use the Nyström method since we cannot apply our meshfree basis functions.

We are concerned with the second and third options to solve BIE, which rely on approximating the unknowns on the boundary by basis functions.

3.3 Collocation Method

Suppose Ω is a polygonal (or polyhedral domain) with sides (or faces) $\Gamma_1, \ldots, \Gamma_N$. That is

$$\Gamma = \bigcup_{j=1}^{N} \Gamma_j.$$

Then (3.7) becomes

$$\frac{1}{2}u(P) + \sum_{j=1}^{N} \int_{\Gamma_j} u(x) \frac{\partial G(x,P)}{\partial n} ds(x) = \sum_{j=1}^{N} \int_{\Gamma_j} \frac{\partial u(x)}{\partial n} G(x,P) ds(x). \tag{3.9}$$

To ease the notation let us introduce the layer potential integral operators. Let

$$D_j u(P) = \int_{\Gamma_j} u(x) \frac{\partial G(x,P)}{\partial n} ds(x) \tag{3.10}$$

be the double layer potential on Γ_j. Let $q(x) = \frac{\partial u(x)}{\partial n}$ and then define

$$S_j q(P) = \int_{\Gamma_j} q(x) G(x,P) ds(x) \tag{3.11}$$

as the single layer potential on Γ_j. Then (3.9) becomes

$$\frac{1}{2}u(P) + \sum_{j=1}^{N} D_j u(P) = \sum_{j=1}^{N} S_j q(P). \tag{3.12}$$

Let P_α, $\alpha = 1, \ldots, M$, be chosen boundary particles and let Φ_α, $\alpha = 1, \ldots, M$, be approximation functions corresponding to these boundary particles such that

$$\Gamma \subset \bigcup_{j=1}^{N} \text{supp}(\Phi_j) \text{ and } \Phi_\alpha(P_\beta) = \delta_\alpha^\beta. \tag{3.13}$$

For each element Γ_j, suppose $P_{j_1}, \ldots, P_{j_{n(j)}}$ are those nodes among P_α that lie on Γ_j. Then u and $\dfrac{\partial u}{\partial n}$ are approximated by

$$u|_{\Gamma_j} \approx \sum_{k=1}^{n(j)} \Phi_{j_k}(x) u_{j_k}, \text{ and} \tag{3.14}$$

$$q|_{\Gamma_j} \approx \sum_{k=1}^{n(j)} \Phi_{j_k}(x) q_{j_k}. \tag{3.15}$$

Where u_{j_k} and q_{j_k} are values of u and q at node P_{j_k} on element Γ_j. From Eq. (3.13), we have

$$u(P_\alpha) = \sum_{j=1}^{N}\sum_{k=1}^{n(j)} \Phi_{j_k}(P_\alpha)u_{j_k} = \sum_{j=1}^{N}\sum_{k=1}^{n(j)} \delta^\alpha_{j_k} u_{j_k} = u_\alpha.$$

Substituting Eqns (3.14) and (3.15) into Eqn (3.4) we have

$$c(P_\alpha)u_\alpha + \sum_{j=1}^{N}\sum_{k=1}^{n(j)} u_{j_k} D_j\Phi_{j_k}(P_\alpha) = \sum_{j=1}^{N}\sum_{k=1}^{n(j)} q_{j_k} S_j\Phi_{j_k}(P_\alpha). \tag{3.16}$$

Let

$$a^\alpha_{j_k} = D_j\Phi_{j_k}(P_\alpha) \text{ and } b^\alpha_{j_k} = S_j\Phi_{j_k}(P_\alpha). \tag{3.17}$$

Then (3.16) can be written as follows:

$$c(P_\alpha)u_\alpha + \sum_{j=1}^{N}\sum_{k=1}^{n(j)} u_{j_k} a^\alpha_{j_k} = \sum_{j=1}^{N}\sum_{k=1}^{n(j)} q_{j_k} b^\alpha_{j_k} \tag{3.18}$$

which holds for each particle P_α. This is the linear system we will construct for solving the second type of BEM, the collocation method.

Depending on the given boundary conditions on Γ, at each α, either u_α or q_α is unknown. Equation (3.18) has M-unknowns and considering this for each particle $P_\alpha, \alpha = 1, \ldots, M$, we have the M-equations for M-unknowns. The only problem left is to calculate the coefficients $a^\alpha_{j_k}$ and $b^\alpha_{j_k}$. Once these are calculated, and the system is solved, u can be evaluated at any point in Ω using Eqn (3.4).

3.3.1 Calculating the Coefficients for d=2

In calculating the coefficients for $d = 2$, let us note the following: Suppose S is the line segment on some part of Γ connecting $P_1 = (x_1, y_1)$ and $P_2 = (x_2, y_2)$. That is, $S = \overleftrightarrow{P_1P_2} \subset \Gamma$. The integrals for the coefficients $a^\alpha_{j_k}, b^\alpha_{j_k}$ are of the form

$$\begin{aligned} I(P) &= \int_S \frac{h(x)}{|x-P|} ds(x), \text{ or} \\ I_{log}(P) &= \int_S h(x)\log|x-P| ds(x), \text{ where } P \in \Gamma. \end{aligned}$$

When $P \in S$ these integrals become singular and special techniques must be used to evaluate them. For polygonal domains in $\mathbb{R}^2$, $a_{j_k}^{\alpha} = 0$ because

$$\frac{\partial G(x,P)}{\partial n}|_S = \nabla G(x,P) \cdot n = 0. \tag{3.19}$$

So the only singular integral to consider comes from $b_{j_k}^{\alpha}$ which is of the form $I_{log}(P)$. To evaluate this, we split S at the point P so that S_1 connects P_1 to P and S_2 connects P to P_2. Then

$$I_{log}(P) = \int_{S_1} h(x) \log|x-P| ds(x) + \int_{S_2} h(x) \log|x-P| ds(x).$$

Consider only the first integral, the second may be evaluated similarly. Here

$$x(t) = (P_1 - P)t + P \text{ where } t \in [0,1].$$

Then if we set $L = |P_1 - P|$ we have

$$\begin{aligned} \int_{S_1} h(x) \log|x-P| ds(x) &= \int_0^1 h((P_1-P)t+P) \log|(P_1-P)t| L dt \\ &= L \log L \int_0^1 h((P_1-P)t+P) dt \\ &+ L \int_0^1 h((P_1-P)t+P) \log t dt. \end{aligned}$$

The first integral may be computed by standard Gaussian quadrature rules, whereas the second integral should be computed using Logarithmic Gaussian quadrature rules. Without taking special care in the treatment of the singular integrals, the high accuracy of the numerical solution will be lost.

3.3.2 Calculating the Coefficients for d=3

In calculating the coefficients for $d = 3$, let us note the following: Suppose S is polygonal patch on some part of Γ. The integrals for the coefficients $a_{j_k}^{\alpha}, b_{j_k}^{\alpha}$ are of the form

$$I_n(P) = \int_S \frac{h(x)}{|x-P|^n} ds(x), \text{ where } n = 1, 2 \text{ and } P \in \Gamma.$$

When $P \in S$ these integrals become singular and special techniques must be used to evaluate them, whereas if $P \notin S$ there is no singularity and standard Gaussian quadrature may be used. For polyhedral domains in $\mathbb{R}^3$, $a_{j_k}^{\alpha} = 0$ because of Eqn.

(3.19).

Again, the only singular integral to consider comes from $b^{\alpha}_{j_k}$ which is of the form $I_1(P)$. To evaluate this integral we followed two different ideas. First, we used the Duffy transform. The Duffy transform takes the unit triangle centered at the origin, where it has a singularity, and maps it to the unit square moving the singularity to one side of the square. This map weakens the singularity and improves the accuracy of numerical integration. See Figure 3.1 and refer to [14].

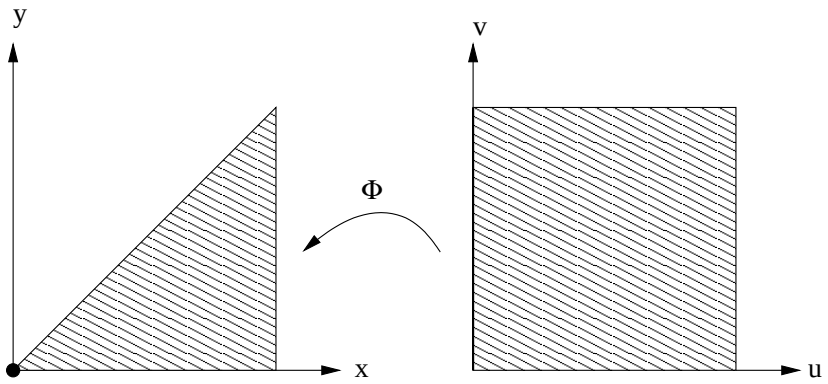

Figure 3.1: The Duffy transformation maps the unit triangle with singularity at origin to unit square moving the singularity to one side with the map $(x, y) = \Phi(u, v) = (u, uv)$.

To use this, we consider the position of P on S. If P is far enough away from the boundary of S or exactly on the boundary, we may split S into triangles and evaluate the integrals using the Duffy transform. If P is near the boundary of S, performing this process can create distorted triangles. This can cause the Jacobian of the transformation to become large and decrease the accuracy of integration. Because of this, we create a quadrangle around P and decompose this into four triangles and integrate the rest of the region using standard Gaussian Quadrature. See Figure 3.2.

The second idea is somewhat simpler. As before, we decompose S into several different patches. This time we break S into a disc centered at P and quadrangles. By this decomposition, the Jacobian from the transformation into the disc removes the singularity in this region and regular Gaussian quadrature can be used. In the

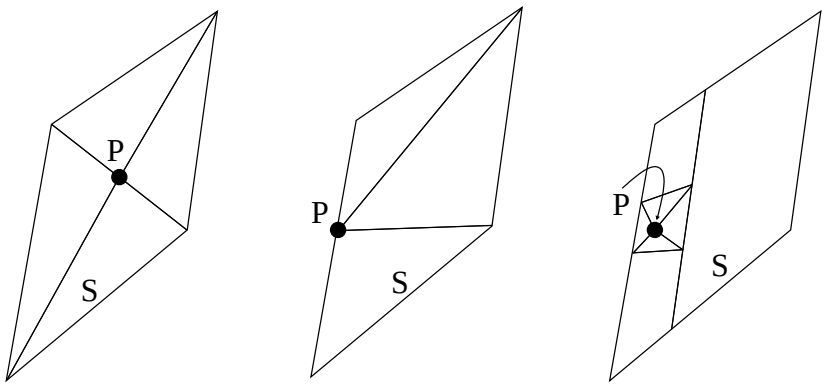

Figure 3.2: Cases for splitting S using the Duffy transform. P is away from the boundary of S (Left). P is on the boundary of S (Middle). P is near the boundary of S(Right).

quadrangles, the integral is not singular and Gaussian quadrature can also be used. If P is on the boundary of S, we may use just a portion of the disc, in which, the Jacobian will still weaken the singularity. If P is close to the boundary of S then we create a quadrangle around P and proceed similarly. See Figure 3.3.

This approach is simpler than the Duffy transformation, however, some quadrangles will have a curved side; hence a blending type transformation ([54]) should be used for Gaussian quadrature rules.

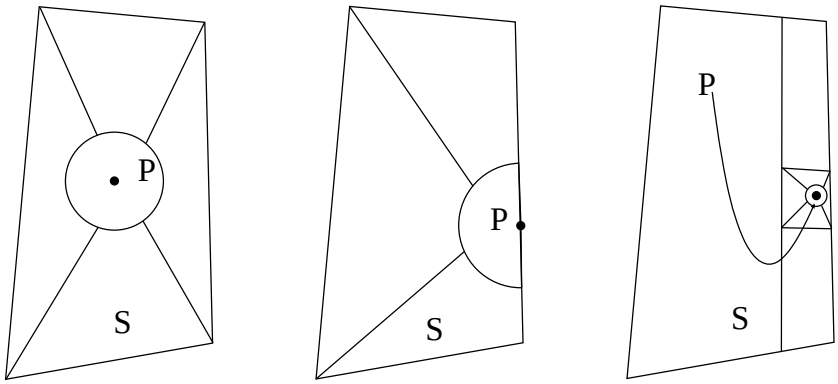

Figure 3.3: Cases for splitting S using the second method. P is away from the boundary of S (Left). P is on the boundary of S (Middle). P is near the boundary of S(Right).

The collocation method generates a full non-symmetric stiffness matrix which

can be solved directly or iteratively. When the number of unknowns is large, it is recommended to use an iterative solver such as GMRES.

3.4 Galerkin Method

For the Galerkin method, much of our assumptions stay the same as for the collocation method, however we only present the case when $d = 2$. First, we will once again consider boundary particles P_α ,$\alpha = 1, \ldots, M$ and the corresponding basis functions $\Phi_\alpha(x)$. As before, let

$$u|_\Gamma \approx \sum_{\alpha=1}^{M} \Phi_\alpha(x) u_\alpha, \text{ and} \tag{3.20}$$

$$q|_\Gamma \approx \sum_{\alpha=1}^{M} \Phi_\alpha(x) q_\alpha. \tag{3.21}$$

Multiplying (3.4) by Φ_β,$\beta = 1, \ldots, M$, and integrating over Γ with respect to P, we see

$$\begin{aligned} \sum_{j=1}^{N} u_\alpha \int_{\Gamma(P)} c(P)\Phi_\alpha(P)\Phi_\beta(P) ds(P) &+ \sum_{j=1}^{N} u_\alpha \int_{\Gamma(P)} D_j \Phi_\alpha(P)\Phi_\beta(P) ds(P) \\ &= \sum_{j=1}^{N} q_\alpha \int_{\Gamma(P)} S_j \Phi_\alpha(P)\Phi_\beta(P) ds(P). \end{aligned}$$

Which can be rewritten as

$$(A + B)\mathbf{u} = C\mathbf{q},$$

where

$$\begin{aligned} A_{\alpha\beta} &= \int_{\Gamma(P)} c(P)\Phi_\alpha(P)\Phi_\beta(P) ds(P), \\ B_{\alpha\beta} &= \int_{\Gamma(P)} \int_{\Gamma(x)} \frac{\partial G(x,P)}{\partial n} \Phi_\alpha(x)\Phi_\beta(P) ds(x) ds(P), \text{ and} \\ C_{\alpha\beta} &= \int_{\Gamma(P)} \int_{\Gamma(x)} G(x,P)\Phi_\alpha(x)\Phi_\beta(P) ds(x) ds(P). \end{aligned}$$

Entries of the coefficient matrix A contain no singular integrals, however entries of B and C do. Hence, integrals for the entries of the coefficient matrices B and C must be carefully analyzed.

Entries of the coefficient matrix B contain singular integrals of the type $\frac{1}{r}$, but since there is an extra integration being performed, it is only a weak singularity. Consider the two basis functions $\Phi_\alpha(x)$ and $\Phi_\beta(P)$. We have three cases.

1. If $\text{supp}(\Phi_\alpha) \bigcap \text{supp}(\Phi_\beta) = 0$, there is no singularity and standard Gaussian quadrature may be used.
2. If $\text{supp}(\Phi_\alpha) \subset \Gamma_i$ and $\text{supp}(\Phi_\beta) \subset \Gamma_i$, $i = 1, \ldots, M$, then $B_{\alpha\beta} = 0$ since $\nabla G(x, P) \cdot \mathbf{n} = 0$.
3. From the two cases above, the only way for $B_{\alpha\beta}$ to contain a singularity is for the supports of each basis function to intersect, but not be on the same side of the boundary. This occurs only at the vertices of Ω.

To handle this singularity we consider the segment $L_1 = (P_1, P_2) = \text{supp}(\Phi_\alpha)$ and the segment $L_2 = (P_2, P_3) = \text{supp}(\Phi_\beta)$ so that $L_1 \bigcap L_2 = \{P_2\}$. Then we set $x(t) = (P_1 - P_2)t + P_2$ and $P(s) = (P_3 - P_2)s + P_2$ where $s, t \in [0, 1]$. With this, we see the following:

$$\begin{aligned} B_{\alpha\beta} &= \int_{\Gamma(P)} \int_{\Gamma(x)} \frac{\partial G(x,P)}{\partial n} \Phi_\alpha(x) \Phi_\beta(P) ds(x) ds(P) \\ &= \int_0^1 \int_0^1 -\frac{((P_1 - P_2)t - (P_3 - P_2)s) \cdot \mathbf{n}}{2\pi |(P_1 - P_2)t - (P_3 - P_2)s|^2} \Phi_\alpha(x(t)) \Phi_\beta(P(s)) |L_1||L_2| ds dt \end{aligned}$$

where the singular point is now at the origin in the parameter space. We now split the square into triangles and use the Duffy transform to evaluate this integral.

The coefficient matrix C contains singular integrals of the type $\log r$. We follow the same logic we did for B. This time, whenever $\text{supp}(\Phi_\alpha) \bigcap \text{supp}(\Phi_\beta) \neq 0$ there is a singularity. For this case, we use the Duffy transform with logarithmic quadrature to handle the integration.

Once A, B, and C are calculated, the linear system can then be solved. For the Dirichlet problem, the stiffness matrix is symmetric and one can use a symmetric linear solver. Once the system is solved, u can be evaluated inside Ω using Eqn (3.16) as with the collocation method.

CHAPTER 4: MESHLESS BEM IN TWO DIMENSIONS

In this section, we introduce three collocation based meshless BEM called Reproducing Polynomial Boundary Particle Methods (RPBPM) which yield numerical solutions of BIEs in two dimensions. We also demonstrate that these proposed methods are superior to the boundary node method ([38]) when the true solution is a polynomial. It should be noted, even though these methods are developed with the collocation method in mind, the basis functions and node placement holds exactly the same for the Galerkin method, as will be seen in a Numerical example.

4.1 Meshfree RPBPM

Suppose $\Omega \subset \mathbb{R}^2$ is a convex polygonal domain as shown in Figure 4.1 in which particles are edge-wise uniformly spaced. That is, the width between two adjacent particles on different edges are allowed to be different.

Plant uniformly spaced particles on each edge so that no particles are vertices of the polygonal domain Ω. Determine the number of particles so that the width h between two adjacent particles becomes small enough for the required accuracy to be obtained. Pick a basic RPP shape function $\phi_{([-K,K];0;2K-1)}(x)$ whose support is $[-K, K]$ among those listed in ([45]). For each edge Γ_j, set up a parametrization φ_j from an interval $[-K, K]$ into an extended edge $\hat{\Gamma}_j$ so that the integer points in $[-K, K]$ are mapped onto equally spaced nodes on $\hat{\Gamma}_j$, as shown in Figure 4.1. Construct particle shape functions corresponding to each particle P_{j_k} along $\hat{\Gamma}_j$ by a translation of $\phi_{([-K,K];0;2K-1)} \circ \varphi_j$. For example, suppose h is the width of uniformly spaced particles in Figure 4.2. Then, for each $k = 1, 2, \ldots, 12$, the RPP shape function corresponding to the particle x_k is

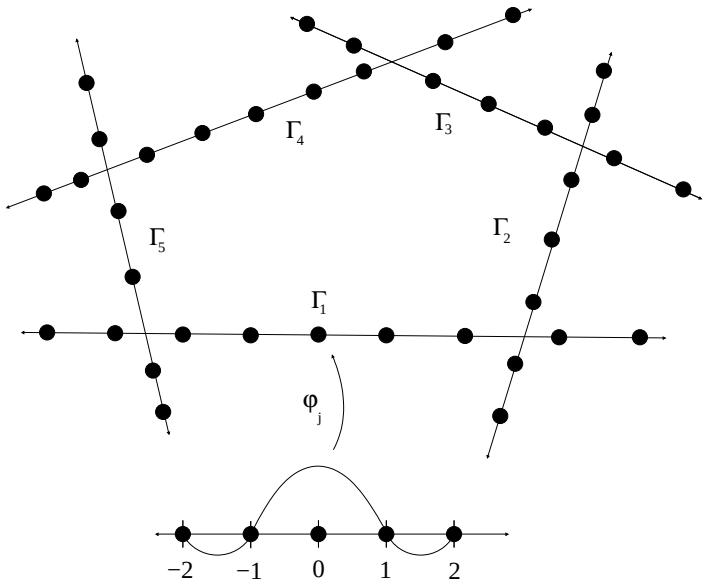

Figure 4.1: Diagram of meshfree particles planted on edges of polygonal domain Ω and basic RPP shape functions $\phi_{([-2,2];0;3)}(x)$ with RPP order 3.

$$\phi_{x_k}(x) = \phi_{([-K,K];0;2K-1)}(\frac{x - x_k}{h}). \tag{4.1}$$

Then, in order to keep the reproducing order for all points in Γ_j, $2K$ particles should be outside of the edge Γ_j. For those nodes shown in Figure 4.2, no boundary conditions are available; hence the boundary data on the external particles can be extrapolated by least squares method and the property of reproducing polynomials as described below.

Without loss of generality, we may assume that $K = 2$, and $P_{ik} = P_{i1} + h(k-1)$ for each $k = 1, \ldots, N_i$. Then the four particles $P_{i1}, P_{i2}, P_{i(N_i-1)}, P_{iN_i}$ go outside the ith edge as shown in Figure 4.2. Suppose the Dirichlet boundary condition is imposed along the edge Γ_i. Then for the approximation $u|_{\Gamma_i} \approx \sum_{k=1}^{N_i} u_{ik}\psi_{ik}(x)$, the amplitudes u_{ik} are known for $k = 3, 4, \ldots, N_i - 2$.

We want to extrapolate the boundary conditions $u_{i1}, u_{i2}, u_{i(N_i-1)}, u_{iN_i}$ corresponding to the four external (active) particles by the least squares method. For example, u_{i2} minimizes $E(u_{i2})$ defined by,

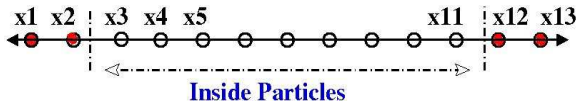

Figure 4.2: Diagram of particles on line segment Γ_j.

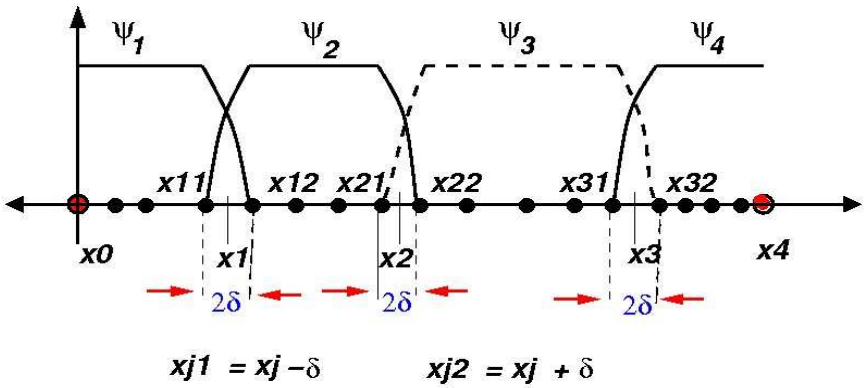

Figure 4.3: Schematic Diagram of Partition of Unity functions $\psi_i, i = 1, 2, 3, 4$.

$$E(u_{i2}) = \int_{x(P_{i3})}^{x(P_{i4})} \left[\sum_{k=2}^{5} u_{ik}\phi_{ik}(x) - u(x) \right]^2 dx$$

In other words,

$$u_{i2} = \int_{x(P_{i3})}^{x(P_{i4})} [u(x) - \sum_{k=3}^{5} u_{ik}\phi_{ik}(x)]\phi_{i2}dx / [\int_{x(P_{i3})}^{x(P_{i4})} \phi_{i2}(x)dx] \tag{4.2}$$

where $u_{i2} = 0$ if the denominator vanishes, and $x(P_{i3})$ is the coordinate of particle P_{i3} in a parametrization of edge Γ_i. Similarly, the boundary condition u_{i1} corresponding to the external node P_{i1} minimizes

$$E(u_{i1}) = \int_{x(P_{i2})}^{x(P_{i3})} \left[\sum_{k=1}^{4} u_{ik}\phi_{ik}(x) - u(x,y) \right]^2 dx$$

As mentioned earlier, in order to obtain highly accurate numerical solutions, special care must be used when evaluating the coefficient matrices.

In order to use particle shape functions with high order reproducing polynomial property defined by (2.5), we placed edge-wise uniformly spaced particles along the boundary. This uniformly spaced particle method uses no mesh at all. However, it

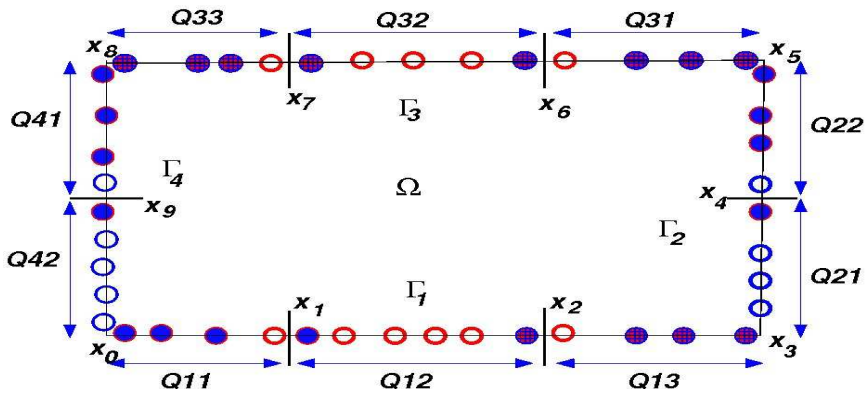

Figure 4.4: Schematic Diagram of particle placement for patch-wise RPBPM.

has a domain restriction and some active particles go outside the domain as shown in Figure 4.1.

These difficulties can be fixed by introducing background meshes as shown in Figures 4.3 and 4.4. Using partition of unity shape functions with flat-top, one can construct the particle shape functions corresponding to particles with arbitrary spacing, as will be seen in the coming sections where the support of each PU function is the corresponding background mesh and each particle shape functions also have the Kronecker delta property and the reproducing polynomial property.

4.2 Patch-wise RPBPM

In order to avoid extrapolating the boundary values corresponding to those nodes that are outside of the boundary, we construct patch-wise RPP shape functions that correspond to patch-wise uniformly (or non-uniformly) spaced particles.

Suppose $\partial\Omega = \cup_{k=1}^{n}\Gamma_k$ is union of the edges of a polygonal domain Ω.

Suppose $\Gamma_k = [x_0, x_1]\cup[x_1, x_2]\cup[x_2, x_3]\cup[x_3, x_4]$ as shown in Figure 4.3 and x_0, x_4 are vertex nodes of the polygonal domain. For example, $\Gamma_1 = Q_{11}\cup Q_{12}\cup Q_{13}; \Gamma_2 = Q_{21}\cup Q_{22}; \Gamma_3 = Q_{31}\cup Q_{32}\cup Q_{33}; \Gamma_4 = Q_{41}\cup Q_{42}$, in Figure 4.4. Let us choose a small number δ with $0.01 \leq \delta < \min\{0.1, (x_j - x_{j-1})/3, j = 1, 2, 3, 4\}$. If $\chi_{[x_{j-1},x_j]}$ is the characteristic function of an interval $[x_{j-1}, x_j]$ defined by

$$\chi_{[x_{j-1},x_j]}(x) = \begin{cases} 1 & : x \in [x_{j-1}, x_j] \\ 0 & : \text{ otherwise} \end{cases}$$

then for $x \in \Gamma_k$,

$$\chi_{[x_0-\delta,x_1]}(x) + \chi_{(x_1,x_2]}(x) + \chi_{(x_2,x_3]}(x) + \chi_{(x_3,x_4+\delta]}(x) = 1;$$

hence, the convolutions of these functions with window function $w_\delta^l(x)$, $\psi_1 = \chi_{[x_0-\delta,x_1]} * w_\delta^l$, $\psi_2 = \chi_{(x_1,x_2]} * w_\delta^l$, $\psi_3 = \chi_{(x_2,x_3]} * w_\delta^l$, $\psi_4 = \chi_{(x_3,x_4+\delta]} * w_\delta^l$ shown in Figure 4.3, become a partition of unity subordinate to the patches

$$[x_0 - 2\delta, x_1 + \delta], \quad [x_1 - \delta, x_2 + \delta], \quad [x_2 - \delta, x_3 + \delta], \quad [x_3 - \delta, x_4 + 2\delta].$$

Specifically, with (2.10), these PU functions with flat-top can be written as $\psi_1(x) = \psi^{(\delta,n-1)}_{[x_1-\delta,x_1]}(x)$, $\psi_2(x) = \psi^{(\delta,n-1)}_{[x_1,x_2]}(x)$, $\psi_3(x) = \psi^{(\delta,n-1)}_{[x_2,x_3]}(x)$, $\psi_4(x) = \psi^{(\delta,n-1)}_{[x_3,x_4+\delta]}(x)$. Let $\{x_{11}, x_{12}, \ldots, x_{1K_1}\}$, $\{x_{21}, x_{22}, \ldots, x_{2K_2}\}$, $\{x_{31}, x_{32}, \ldots, x_{3K_3}\}$, and $\{x_{41}, x_{42}, \ldots, x_{4K_4}\}$, be distinct particles planted (not necessary uniformly spaced) in the intervals $[x_0 + \delta, x_1 + \delta]$, $[x_1 - \delta, x_2 + \delta]$, $[x_2 - \delta, x_3 + \delta]$, and $[x_3 - \delta, x_4 - \delta]$, respectively. We assume that all $(K_1 + K_2 + K_3 + K_4)$-particles are distinct.

Recall that the Chebyshev polynomial $T_n(x)$ of degree $n \geq 1$ has n simple roots in $[-1, 1]$ at $x_k = \cos((2k-1)\pi/2n)$, for each $k = 1, 2, \ldots, n$. It is known that these zeros are an optimal choice for nodes for the Lagrange interpolating polynomial. Thus, we suggest to use the shifted $x_k = \cos((2k-1)\pi/2n)$ into appropriate intervals for particles $x_{k,j}, j = 1, \ldots, K_k, k = 1, 2, 3, 4$. However, for this work we simply use equally spaced nodes in the reference domain for Lagrange polynomials.

For $j = 1, \ldots, K_1$, let $L_{1j}(x)$ be the j-th Lagrange interpolating polynomial of degree $(K_1 - 1)$ corresponding to particles $x_{11}, x_{12}, \ldots, x_{1K_1}$. Then these functions have the reproducing polynomial property of order $(K_1 - 1)$. Similarly, we construct the Lagrange interpolating polynomials $L_{ij}(x)$ for $j = 1, \ldots, K_i$ and $i = 2, 3, 4$

Using $\sum_{i=1}^4 \psi_i(x) = 1$, we prove the following theorem.

Theorem 4.1. *On* $[x_0, x_4]$, *the functions* $\psi_i(x)L_{ij}(x)$ *for* $j = 1, \ldots, K_i$ *and* $i = 1, \ldots, 4$ *are* $\mathcal{C}^{l-1}$ *piecewise polynomial RPP shape functions with reproducing order* k, *where*

$$k = \min\{K_1 - 1, K_2 - 1, K_3 - 1, K_4 - 1\}.$$

Then, on the boundary Γ_j, u and $\dfrac{\partial u}{\partial n}$ are approximated by

$$u|_{\Gamma_i} \approx \sum_{k=1}^{4} \sum_{l=1}^{K_k} \psi_k(x) L_{kl}(x) u_{ikl} \tag{4.3}$$

$$q|_{\Gamma_i} = \frac{\partial u}{\partial n}|_{\Gamma_i} \approx \sum_{k=1}^{4} \sum_{l=1}^{K_k} \psi_k(x) L_{kl}(x) q_{ikl}. \tag{4.4}$$

Similarly, for each $i = 1, \ldots, n$, we construct highly smooth patch-wise RPP shape functions corresponding to particles planted on patches of edge Γ_i as shown in Figure 4.4.

4.3 Patch-wise RSBPM

Here, we introduce a patch-wise reproducing singularity boundary particle method (RSPBM). Suppose an isotropic non-convex polygonal domain Ω has a corner point at which the internal angle is π/α, where α is a real number with $0 < \alpha < 1$. An elliptic equation on Ω contains a singularity of type $r^\alpha f(\theta)$. The number α is called the intensity of a singularity. To deal with elliptic problems containing singularities, Oh et al. ([47]) constructed Reproducing Singularity Particle(RSP) shape functions that reproduce polynomials as well as singular functions that resemble the singularities.

In this section, we are concerned with BEM for elliptic equations containing corner singularities or jump boundary data singularity (Motz problem). Since we consider problems on polygonal domains, we may assume that $f(\theta)$ is constant, and hence the singularity along edges is of type r^α with $0 < \alpha < 1$.

Let us note that $\alpha = 1/2$ for the crack and the jump boundary data (Motz Problem) singularities.

Define $T : [0, b] \longrightarrow [0, b^\alpha]$ to be a singular mapping defined by $\xi = T(x) = x^\alpha$.

Let $0 < \xi_0 < \xi_1 < \cdots < \xi_{2N} \leq b^\alpha$ be particles in $[0, b^\alpha]$. If $L_j(\xi)$ is the j-th Lagrange interpolating polynomial associated with above $2N + 1$ nodes, then $L_j(\xi), j = 0, 1, \ldots, 2N$, have the polynomial reproducing property with reproducing order $2N$. That is,

$$\sum_{j=0}^{2N} \xi_j^k L_j(\xi) = \xi^k, \text{ for } 0 \leq k \leq 2N. \tag{4.5}$$

Using the arguments in ([47]), one can easily prove the following: For $j = 0, 1, \ldots, 2N$, let $\Phi_j^*(x) = L_j(T(x))$ and $x_j = T^{-1}(\xi_j)$. Then

1. $\Phi_j^*(x_i) = \delta_i^j$ (Kronecker delta property).
2. If $\alpha = 1/2$ then meshfree particle shape functions: $\Phi_j^*, j = 0, 1, \ldots, 2N$, generate the polynomials

   $$1, x, x^2, \ldots, x^N$$

   and the singular functions

   $$x^{1/2+k}, k = 0, 1, 2, \ldots, (N-1).$$

We now modify the basic PU function (2.10) as follows:

$$\psi_0(x) = \begin{cases} 1 & \text{if } \; x \in (0, b-\delta] \\ \phi_{g_n}^R(\frac{x-(b-\delta)}{2\delta}) & \text{if } \; x \in [b-\delta, b+\delta] \\ 0 & \text{if } \; x \notin (0, b+\delta], \end{cases} \tag{4.6}$$

which is a one-dimensional version of the almost everywhere partition of unity introduced in ([42]). A schematic diagram for $\psi_0(x)$ is shown in Figure 4.5. Note that $\psi_0(x)$ is undefined at $(0, 0)$, the singularity point.

Now RSP shape functions to deal with singularity of type r^α are defined as follows:

$$\Phi_j(x) = \psi_0(x) \times \Phi_j^*(x), \quad j = 0, 1, \ldots, 2N. \tag{4.7}$$

4.4 Numerical Examples

An application of a meshless method to BEM, the boundary node method, in which Moving Least Squares (MLS) method was applied to construct nodal approximation functions, was introduced in ([25],[38], and reference cited there). However, these meshless approximation functions constructed by MLS do not satisfy the Kronecker delta property and hence this meshless boundary node method(BNM) fail to capture the traction (Neumann) boundary values when there are jump discontinuities.

However, in this section, we demonstrate that our methods exactly capture the traction boundary values even when the traction functions have large jump discontinuities at the corners whenever the true solutions are polynomials. Moreover, our methods also correctly approximate the true solution and its derivatives at the interior points near boundary.

In the following examples, we consider polynomial solutions of the Laplace equation.

Example 4.4.1. Let $z = x + iy$. Consider Laplace's equation $\Delta u = 0$ on $\Omega = [0,4] \times [0,4]$ whose true solutions are polynomials and boundary conditions are as follows:

(I: Dirichlet problem) The true solution is $u(x,y) = \mathcal{I}m\left(\frac{z^2}{2}\right) = xy$. Displacement (Dirichlet) boundary conditions are prescribed from the true solution along the entire boundary. Exact Dirichlet boundary values are continuous along the entire boundary, whereas the exact traction boundary values have jump discontinuities, $[\frac{\partial u}{\partial n}] = 4$, at the corner points $(4,0)$ and $(0,4)$.

(II: Mixed problem 1) The exact solution is $u(x,y) = \mathcal{R}e(z^2) = x^2 - y^2$. Mixed boundary conditions are prescribed from the true solution on the boundary as follows:

$$\begin{aligned} \frac{\partial u}{\partial n} &= 0 \text{ on the lines } x = 0 \text{ and } y = 0 \\ u &= \mathcal{R}e(z^2) \text{ on the lines } x = 4 \text{ and } y = 4 \end{aligned}$$

The traction boundary values q have the large jump discontinuities, $[\frac{\partial u}{\partial n}] = 16$, at the

corner points $(4, 0)$ and $(0, 4)$.

Examples (I) and (II), respectively, are examples 5 and 6 of ([38]).

(III: Mixed problem 2) The true solution is $u(x, y) = \mathcal{R}e(z^4) = x^4 - 6x^2y^2 + y^4$. The boundary conditions are similar to (II). Traction boundary values q have even larger jump discontinuities, $[\frac{\partial u}{\partial n}] = 256$, at the corner points $(4, 0)$ and $(0, 4)$.

From our numerical tests of the above three examples, we observe the following:

1. Meshfree RPP shape functions and patch-wise RPP shape functions with reproducing order k, respectively, are able to interpolate polynomials of degree k exactly. Hence, our methods can get the exact boundary values as shown in Table 4.1 (for Dirichlet problem), Tables 4.2 and 4.3 (for mixed problem 1), and Table 4.4 (for mixed problem 2) even when the boundary data have a large jump.
2. However, Figures 8 an 9 of ([38]) show that the computed traction boundary values are quite different from the true traction boundary values (the maximum difference ≥ 0.5 for problem I and the maximum difference ≥ 2 for problem II) when moving least squares approximation functions are used at boundary nodes.
3. If the Degree of Freedom (DOF) in meshfree RPP decreases, then the space between uniformly spaced particles increases. Thus, the boundary extrapolations (4.2) for particles outside of the boundary could be less accurate.
4. Since our methods are able to calculate the boundary values exactly, via post processing, our methods can accurately calculate the solutions and their derivatives inside and near the boundary of the domain as seen in Table 4.3.
5. Examples 5 and 6 of ([38]) state that their meshless boundary node method is unable to handle those problems whose traction boundary data have jumps at corners. Moreover, it is worse when the traction data have larger jump discontinuities. However, Table 4.4 shows that our method yields the exact

Table 4.1: Absolute error in maximum norm of the computed traction boundary values $\tilde{q}$ of case (I) of Example 4.4.1. The true traction boundary values q have jump discontinuities $[\frac{\partial u}{\partial n}] = 4$, at the corner points $(4, 0)$ and $(0, 4)$.

Methods	RPP order	DOF	$\|q - \tilde{q}\|_{\infty,\Gamma}$
Meshfree RPP	3	48	1.345E-12
Patch-wise RPP	2	24	1.408E-13
MLS (Fig. 8 of [38])		64	larger than 0.5

Table 4.2: Absolute errors of computed traction boundary data $\tilde{q}$ in maximum norm and computed Dirichlet data $\tilde{u}$ of case (II) of Example 4.4.1. The true traction boundary values have jump discontinuities $[\frac{\partial u}{\partial n}] = 16$, at the corner points $(4, 0)$ and $(0, 4)$.

Methods	RPP order	DOF	$\|u - \tilde{u}\|_{\infty,\Gamma}$	$\|q - \tilde{q}\|_{\infty,\Gamma}$
Meshfree RPP	3	48	8.171E-14	4.832E-13
Patch-wise RPP	2	24	1.865E-14	6.573E-14
MLS(Fig. 9 of [38])	2	128		larger than 2.0

boundary values even when the traction jumps are as big as $[q] = 256$ at the corner points.

6. Since in case (III) of Example 4.4.1, $u|_\Gamma$ is a polynomial of degree 4, the RPP shape functions of reproducing order 2 can not exactly interpolate neither u nor q as shown in Table 4.4. However, the RPP shape functions of reproducing order 4 generate $x^k, k = 0, 1, 2, 3, 4$, hence, they can exactly capture the true boundary values as shown in Table 4.4.

Thus far, we have shown that our methods are able to get the exact boundary values when the true solutions are harmonic polynomials. In the following example, we test the performance of patch-wise RPBPM when the true solution is not a polynomial, but a smooth function (Example 1 of [25]).

Example 4.4.2. Consider Laplace's equation $\Delta u = 0$ on a square $\Omega = [-1, 1] \times [-1, 1]$ with essential boundary condition prescribed from the exact solution $u(x, y) = \sin(x^2 - y^2)\exp(2xy)$ on all boundary.

Table 4.3: Absolute errors of the computed solutions of case (II) of Example 4.4.1 at interior points along the line $y = 4 - x$ connecting corner points $(0, 4)$ and $(4, 0)$ where q has jump discontinuities $[\frac{\partial u}{\partial n}] = 16$. u and $\tilde{u}$, respectively, represent the true and the computed solutions at $(x, 4 - x)$. u_x and u_{xx} are the first and the second derivative of u, respectively.

(x, y)	$\lvert u - \tilde{u}\rvert$	$\lvert u_x - \tilde{u}_x\rvert$	$\lvert u_{xx} - \tilde{u}_{xx}\rvert$
(0.01, 3.99)	2.309E-14	7.572E-13	1.215E-8
(0.10, 3.90)	1.066E-14	2.178E-11	3.702E-8
(0.20, 3.80)	1.243E-14	9.323E-13	9.161E-9
(0.30, 3.70)	0.000E-14	1.637E-11	6.826E-9
(0.70, 3.30)	3.553E-15	2.899E-13	1.497E-9
(1.00, 3.00)	3.553E-15	6.438E-12	1.497E-8
(2.00, 2,00)	1.178E-15	2.273E-12	2.092E-9
(2.50, 1.50)	3.553E-15	7.443E-12	8.158E-9
(3.00, 1.00)	1.776E-15	2.274E-13	1.005E-8
(3.20, 0.80)	3.553E-15	6.400E-12	2.056E-9
(3.30, 0.70)	8.882E-15	4.723E-12	1.393E-8
(3.70, 0.30)	3.553E-15	2.183E-11	3.832E-8
(3.80, 0.20)	3.553E-15	3.604E-12	1.271E-8
(3.90, 0.10)	1.776E-15	9.297E-12	1.271E-8
(3.99, 0.01)	2.487E-14	9.981E-12	3.273E-9

Table 4.4: Absolute error of the computed boundary values of case (III) of Example 4.4.1 in maximum norm. The true traction q has large jump discontinuities $[\frac{\partial u}{\partial n}] = 256$, at the corner points $(4, 0)$ and $(0, 4)$.

Methods	RPP order	DOF	$\lVert u - \tilde{u}\rVert_{\infty,\Gamma}$	$\lVert q - \tilde{q}\rVert_{\infty,\Gamma}$
Patch-wise RPP	2	24	4.763E+00	2.256E+00
Patch-wise RPP	4	40	3.411E-13	8.242E-14

From this example, we observe the following:

1. Even though the boundary values obtained by patch-wise RPP shape functions are the same as the true boundary values at particles, the interpolation function by the RPP shape functions can not be the same as the true boundary values. Therefore, unlike the previous examples, our method can not exactly get the true boundary values.
2. However, the results in Table 4.5 show that our method yields a good approximation at various inside points of the domain. The computed solutions, its first and second derivatives are evaluated in Table 4.5. From Table 4.5, one can see that our method also gives good results at points near the boundary.
3. Since RPP shape functions for our method satisfy the Kronecker delta property, our method gives highly accurate computed solutions when the polynomial reproducing order is high (see, Table 4.5).
4. It is known that p-FEM yields better results than h-FEM at the same number of degree of freedom ([54]) when the true solution is smooth. Similarly, the combination of RPP shape functions of high reproducing order and a small number of patches (the counterpart of p-FEM) yields better results than the combination of RPP shape function of lower reproducing order and a large number of patches (the counterpart of h-FEM) in general.

Now we compare the use of the collocation method compared with the Galerkin method. The difference in the Galerkin method and the collocation method is essentially the way we solve for $u|_\Gamma$ and $q|_\Gamma$. To find $u \in \Omega$, we use the same integral equation. Therefore, it is sufficient to compare the approximated boundary values from each method.

Example 4.4.3. Consider Laplace's equation $\Delta u = 0$ on a square $\Omega = [0,4] \times [0,4]$ with Dirichlet boundary condition prescribed from the exact solution $u(x,y) = \mathcal{I}m\left(\frac{z^4}{4}\right) = (x^2 - y^2)(xy)$ on the entire boundary.

Table 4.5: Computed solutions $\tilde{u}$, the true solution u, relative errors in percentage ($(|(u-\tilde{u})/u| \times 100)$, of Example 4.4.2 at various points inside of the domain Ω. k stands for the reproducing order of the RPP shape functions.

(x, y)	type	$k = 4$ (DOF=40)	$k = 6$ (DOF=56)	$k = 8$ (DOF=72)	True Solution
$(0, 0.2)$	u	-0.0400311545 *0.105%*	-0.0399886387 *0.002%*	-0.0399893059 *0.00007%*	-0.0399893341
$(0, 0.2)$	$u_{,x}$	-0.0159970648 *0.008%*	-0.0159957370 *0.0002%*	-0.0159957363 *0.000016%*	-0.0159957336
$(0, 0.2)$	$u_{,xx}$	1.9927184902 *0.0359%*	1.9909074389 *0.0549%*	1.9930723738 *0.0537%*	1.9920019198
$(0.4, -0.8)$	u	-0.2436170604 *0.051%*	-0.2434902708 *0.0009%*	-0.2434925565 *0.00004%*	-0.2434926608
$(0.4, -0.8)$	$u_{,y}$	0.5532595636 *0.049%*	0.5535387893 *0.00068%*	0.5535351872 *0.00003%*	0.5535349960
$(0.4, -0.8)$	$u_{,yy}$	0.7343015084 *0.669%*	0.7278899705 *0.209%*	0.7302491944 *0.114%*	0.7294211024
$(0.99, 0)$	u	0.8335154579 *0.357%*	0.8304450311 *0.013%*	0.8305458079 *0.0009%*	0.8305530685
$(0.999, 0)$	u	0.8432689647 *0.343%*	0.8402652512 *0.015%*	0.8403801738 *0.001%*	0.8403892399
$(0.9999, 0)$	u	0.8439439846 *0.307%*	0.8409555723 *0.048%*	0.8410720063 *0.035%*	0.8413629129

From this example, we observe the following:

1. For this example, we use two PU functions with flat-tops on each side of Γ and test for RPP orders 2, 3 and 4.
2. The same basis functions are being used and we are solving a Dirichlet problem. Therefore, $\|u - \tilde{u}\|_{\infty,\Gamma}$ will be the same for the Galerkin method and the collocation method. Hence, we compare $\|q - \tilde{q}\|_{\infty,\Gamma}$ for each method.
3. The true solution is a degree 4 polynomial. However, evaluated on each side of the domain, $u|_\Gamma$ and $q|_\Gamma$ are at most a degree 3 polynomial. For this reason, we expect basis functions of RPP order 3 or greater to be able to capture the solution. Any basis function of lower RPP order will not be able to capture the solution. From the table, we see what we expect. We notice that when the RPP order is 2, both methods produce poor results and the Galerkin method is worse. If we increase the number of particles on each side, thus increasing the degrees of freedom, the accuracy will increase, but still will not be satisfactory. For RPP order 3 and 4, we see that the Galerkin method slightly outperforms the collocation method in terms of accuracy.
4. When integrating the fundamental solution or its derivative when the source point is near the region of integration, numerical accuracy deteriorates. These near singularities occur when calculating the entries of the coefficient matrices in the collocation method. To retain high accuracy, more integration points must be used. By construction, the Galerkin method does not encounter near singularities in the computation of the coefficient matrices. So, in computing the coefficient matrices, the Galerkin method requires less computation to evaluate a Boundary integral. However, when evaluating u at points inside Ω, near singularities still can occur and an increase in the number of integration points is needed to get the accuracy desired.
5. Even though the Galerkin method produces a symmetric stiffness matrix for the

Dirichlet problem, the amount of computation required to form this matrix is huge. For each entry, a double boundary integral must be calculated, whereas for the collocation method only a single boundary integral is calculated. Since the accuracy is about the same, and the computation is less, we only proceed with the collocation method for the rest of the examples.

Table 4.6: Absolute errors of computed traction boundary data $\tilde{q}$ in maximum norm for the Galerkin method (G) and the collocation method (C) and computed Dirichlet data $\tilde{u}$ for both in Example 4.4.3.

RPP order	DOF	$\|u-\tilde{u}\|_{\infty,\Gamma}$	$\|q-\tilde{q}\|_{\infty,\Gamma}$ (G)	$\|q-\tilde{q}\|_{\infty,\Gamma}$ (C)
2	24	3.0775E+00	12.0195E+00	1.9594E+00
3	32	2.6645E-14	4.3343E-13	1.1866E-12
4	40	2.7089E-14	1.1369E-12	1.8261E-12

Remark. In the Examples of this section, the normal derivatives (q) have no jumps inside any edges. In the case where q has a jump at a point inside an edge, that point should be treated as a vertex, as we will do in the next section to deal with BIEs containing singularities.

An elliptic problem on the L-shaped domain (Figure 4.5) has a singularity of type $r^{2/3}f(\theta)$ at the re-entrant corner point $(0,0)$.

Example 4.4.4. (Laplace's equation on the L-shaped domain) Consider $\triangle u = 0$ on $\Omega = [-1,1]\times[0,1]\cup[-1,0]\times[0,-1]$ with displacement (Dirichlet) boundary condition prescribed from the exact solution $r^{2/3}\sin(2\theta/3)$ along all boundary. The exact solution has a corner singularity at $(0,0)$ of intensity $2/3$.

We construct RSP shape functions to deal with the corner singularity of type $r^{2/3}$.

1. Label the six edges of Ω as follows (Figure 4.5): $\Gamma_1,\Gamma_2,\Gamma_3,\Gamma_4,\Gamma_5,\Gamma_6$, respectively, that are the line segments on $y=0, x=1, y=1, x=-1, y=-1, x=0$.

Dividing the edge Γ_1 into two patches $(0, b)$ and $(b, 1)$, we define PU functions on the edge Γ_1 as follows:

$$\psi_0(x) = \begin{cases} 1 & \text{if } x \in (0, b-\delta] \\ \phi^R_{g_n}(\frac{x-(b-\delta)}{2\delta}) & \text{if } x \in [b-\delta, b+\delta] \\ 0 & \text{if } x \notin (0, b+\delta], \end{cases} \tag{4.8}$$

$$\psi_1(x) = \begin{cases} \phi^L_{g_n}(\frac{x-(b+\delta)}{2\delta}) & \text{if } x \in [b-\delta, b+\delta] \\ 1 & \text{if } x \in [b+\delta, 1] \\ 0 & \text{if } x \notin [b-\delta, 1], \end{cases} \tag{4.9}$$

Then $\psi_0(x) + \psi_1(x) = 1$, for all $x \in \Gamma_1$.

2. Suppose we choose $N = 3$ in (4.5) and $\delta = 0.01$. Let $L_{0j}(\xi), j = 0, 1, \ldots, 6$, be the Lagrange interpolating polynomials associated to the nodes:

$$0 < \xi_{00} < \xi_{01} < \xi_{02} < \xi_{03} < \xi_{04} < \xi_{05} < \xi_{06} = (b+\delta)^{1/3}.$$

Let $L_{1j}(\xi), j = 0, 1, \ldots, 6$, be the Lagrange interpolating polynomials associated to the nodes:

$$(b-\delta)^{1/3} = \xi_{10} < \xi_{11} < \xi_{12} < \xi_{13} < \xi_{14} < \xi_{15} < \xi_{16} = 0.99 < 1.$$

For each $k = 0, 1$, and each $j = 0, 1, \ldots, ,$ define RSP shape functions to deal with the corner singularity of intensity $2/3$ by

$$\Phi_{kj}(x) = \psi_k(x) \cdot L_{kj}(x^{1/3}).$$

Then, for an approximation of boundary functions on Γ_1, we use

$$u|_{\Gamma_1} = \sum_{k=0}^{1} \sum_{j=0}^{6} u_{kj} \Phi_{kj}(x) \text{ and} \tag{4.10}$$

$$q|_{\Gamma_1} = \sum_{k=0}^{1} \sum_{j=0}^{6} q_{kj} \Phi_{kj}(x)/(x^{1/3}). \tag{4.11}$$

Note that $L_{0j}(x^{1/3}), j = 0, 1, \ldots, 6$, generates

$$1, x^{1/3}, x^{2/3}, x, x^{4/3}, x^{5/3}, x^2$$

and $L_{0j}(x^{1/3})/(x^{1/3}), j = 0, 1, \ldots, 6$, generates

$$x^{-1/3}, 1, x^{1/3}, x^{2/3}, x, x^{4/3}, x^{5/3}.$$

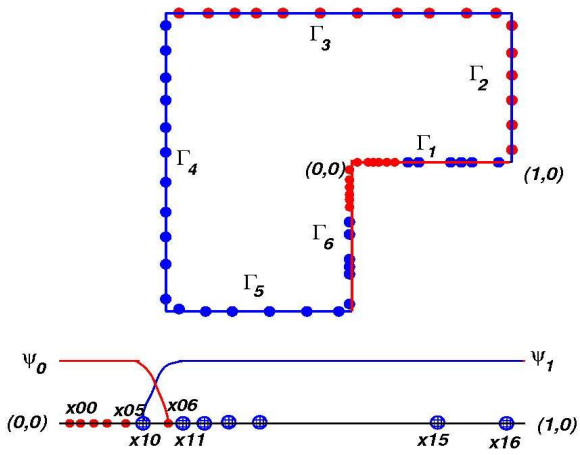

Figure 4.5: Diagram of the L-shaped domain with corner singularity(Top). Schematic diagram of two PU functions ψ_0, ψ_1 and 14 singular particles corresponding to RSP shape functions(Bottom).

Table 4.7: Errors in maximum norm of Laplace's equation on the L-shaped domain with Dirichlet boundary conditions prescribed by the true solution $u = r^{2/3}\sin(2\theta/3)$.

k	DOF		$\|u-\tilde{u}\|_{\infty,\Gamma}$	$\|q-\tilde{q}\|_{\infty,\Gamma}$	$\|u-\tilde{u}\|_{\infty,\Omega}$
4	60	RSBPM	3.766E-5	3.001E-3	1.291E-5
		RPBPM	4.031E-5	1.118E-0	1.140E-2
6	84	RSBPM	1.663E-6	2.983E-3	8.040E-6
		RPBPM	1.530E-6	0.848E-0	7.206E-3

These two sets of functions are able to approximate $r^{2/3}\sin(2\theta/3)$ and its derivative, respectively. Similarly, RSP shape functions are constructed to approximate the boundary functions along Γ_6. Let us note that the vertices $(0,0)$, $(1,0)$, $(0,-1)$ should not be particles for RSP shape functions.

3. We use RPP shape functions for an approximation of boundary functions on the edges $\Gamma_k, k = 2,3,4,5$. Similarly, vertices $(1,1), (-1,1), (-1,-1), (0,-1)$ should not be particles for RPP shape functions on $\Gamma_2, \Gamma_3, \Gamma_4, \Gamma_5$.
4. The error of the computed traction $\tilde{q}$ and the error of the computed solution $\tilde{u}$ in maximum norm on entire domain are shown in Table 4.7. Table 4.7 shows that the solutions obtained by using mapping techniques (RSBPM) are far better than those obtained by RPBPM that does not use mapping techniques.

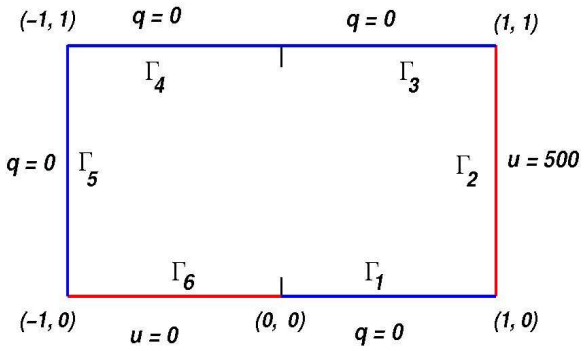

Figure 4.6: The rectangular domain for the Motz problem.

Consider the Motz problem that contains a jump boundary data singularity of type $\mathcal{O}(r^{1/2})$ at $(0,0)$. For numerical solutions of this problem, many computational techniques are suggested in the literature. Especially, we refer to ([1],[33]) which is closely related to this work.

Example 4.4.5. (Motz problem) Consider $\triangle u = 0$ on a rectangular domain $\Omega = [-1,1] \times [0,1]$ with mixed boundary conditions prescribed as follows:

$$\begin{aligned} u &= 0 \text{ on } \Gamma_6, \quad u = 500 \text{ on } \Gamma_2 \\ \frac{\partial u}{\partial n} &= 0 \text{ on } \Gamma_1 \cup \bigcup_{i=3}^{5} \Gamma_i, \end{aligned}$$

where $\Gamma_1 = [0,1] \times \{0\}, \Gamma_2 = \{1\} \times [0,1], \Gamma_3 = [0,1] \times \{1\}, \Gamma_4 = [-1,0] \times \{1\}, \Gamma_5 = \{-1\} \times [0,1], \Gamma_6 = [-1,0] \times \{0\}$, as shown in Figure 4.6. Then, the asymptotic expansion of the true solution in a polar coordinates centered at $(0,0)$ is of the form

$$u(r,\theta) = \sum_{k=1}^{\infty} A_k r^{\frac{2k-1}{2}} \cos\big((2k-1)\frac{\theta}{2}\big). \tag{4.12}$$

We construct the RSP shape functions to approximate singular boundary functions on Γ_1 and Γ_6 and the RPP shape functions to approximate smooth boundary functions on $\Gamma_2, \Gamma_3, \Gamma_4$ and Γ_5.

1. For example, we choose $N = 3$ in (4.5), $\delta = 0.05$ and $b = 0.25$. Let $L_{0j}(\xi), j = 0, 1, \ldots, 6$, be the Lagrange interpolating polynomials associated to the nodes:

$$0 < \xi_{00} < \xi_{01} < \xi_{02} < \xi_{03} < \xi_{04} < \xi_{05} < \xi_{06} = (b+\delta)^{1/2}.$$

where $\xi_{06} - \xi_{05} > (2\delta)^{1/2}$. Let $L_{1j}(\xi), j = 0, 1, \ldots, 6$, be the Lagrange interpolating polynomials associated to the nodes:

$$(b-\delta)^{1/2} = \xi_{10} < \xi_{11} < \xi_{12} < \xi_{13} < \xi_{14} < \xi_{15} < \xi_{16} = 0.99 < 1,$$

where $\xi_{11} - \xi_{10} > (2\delta)^{1/2}$.

Suppose ψ_0 and ψ_1 are PU functions defined by (4.8) and (4.9), respectively. For each $k = 0, 1$, and each $j = 0, 1, \ldots, 6$, we define singular approximation functions by

$$\Phi_{kj}(x) = \psi_k(x) \cdot L_{kj}(x^{1/2}).$$

Then, for an approximation of boundary functions on Γ_1, we use

$$u|_{\Gamma_1} = \sum_{k=0}^{1} \sum_{j=0}^{6} u_{kj} \Phi_{kj}(x) \tag{4.13}$$

$$q|_{\Gamma_1} = \sum_{k=0}^{1} \sum_{j=0}^{6} q_{kj} \left[\Phi_{kj}(x)/\sqrt{x}\right]. \tag{4.14}$$

2. Then, $L_{0j}(\sqrt{x}), j = 0, 1, \ldots, 6$ and $L_{1j}(\sqrt{x}), j = 0, 1, \ldots, 6$ are RSP shape functions corresponding to nodes $(\xi_{0j})^2, j = 0, 1, \ldots, 6$ and $(\xi_{1j})^2, j = 0, 1, \ldots, 6$, respectively, which reproduce

$$1, x, x^2, x^3, x^{1/2}, x^{3/2}, x^{5/2}, \tag{4.15}$$

over the interval $(0, 1]$.

Moreover, for each $k = 0, 1$, the set of functions $\{L_{kj}(\sqrt{x})/\sqrt{x} : j = 0, 1, \ldots, 6\}$ generate

$$x^{-1/2}, x^{1/2}, x^{3/2}, x^{5/2}, 1, x, x^2. \tag{4.16}$$

$u|_{\Gamma_1} \approx \mathcal{O}(x^{1/2})$ and $q|_{\Gamma_1} \approx \mathcal{O}(x^{-1/2})$. Thus, comparing (4.15) with (4.16), one can see that the particle shape functions, $\left[\Phi_{kj}(x)/\sqrt{x}\right], k = 0, 1; j = 0, 1, \ldots, 6$, can be used for the approximations of both $u|_{\Gamma_1}$ and $q|_{\Gamma_1}$ instead of (4.13) and (4.14).

3. Noting that for $x \in \Gamma_6 = (-1, 0)$, $0 < -x$ and hence RSP shape functions for particles on Γ_6 are constructed as follows: For each $k = 0, 1$, and each

$j = 0, 1, \ldots, 6$, let

$$\tilde{\Phi}_{kj}(x) = \psi_k(-x) \cdot L_{kj}((-x)^{1/2}). \tag{4.17}$$

Then, for an approximation of boundary functions on Γ_6, we use

$$u|_{\Gamma_6} = \sum_{k=0}^{1} \sum_{j=0}^{6} \tilde{u}_{kj} \tilde{\Phi}_{kj}(x) \tag{4.18}$$

$$q|_{\Gamma_6} = \sum_{k=0}^{1} \sum_{j=0}^{6} \tilde{q}_{kj} \psi_k(-x) \cdot \left[L_{kj}(\sqrt{(-x)})/\sqrt{(-x)} \right]. \tag{4.19}$$

The vertices $(0,0), (-1,0), (0,1)$ should not be particles for neither RSP nor RPP shape functions.

4. We use RPP shape functions for an approximation of boundary functions on the edges $\Gamma_k, k = 2, 3, 4, 5$. Similarly, vertices $(1,0), (1,1), (-1,1), (-1,0)$ should not be particles for RPP shape functions on $\Gamma_2, \Gamma_3, \Gamma_4, \Gamma_5$. That is, for particles on the edges that do not contain singularity, we assign RPP shape functions.

A true solution of the Motz problem exists and is given in ([51]). However, for the calculation of errors in Tables 4.8 and 4.9, we assume that the computed true solution u is the sum of first 50 terms in (4.12) and the true normal derivative, q, is the sum of the first 50 terms in

$$\begin{bmatrix} \frac{\partial u}{\partial x} \\ \\ \frac{\partial u}{\partial y} \end{bmatrix} = \frac{1}{2} \sum_{k=1}^{N} A_k (2k-1) r^{(2k-3)/2} \begin{bmatrix} \cos[(2k-3)\theta/2] \\ \\ -\sin[(2k-3)\theta/2] \end{bmatrix}, \tag{4.20}$$

with coefficients being used from Table 12 in ([40]). The coefficients in ([40]) approximate the boundary values better than those provided in ([26]), which were known to be the most accurate approximations of the coefficients.

Table 4.8 shows the maximum errors of q and u along the boundary. Table 4.9 shows the maximum errors of the computed solution $\tilde{u}$ in the whole domain. Tables 4.8 and 4.9 show that RSBPM effectively handles BIEs with a jump boundary data singularity. For comparing purposes, parts of Table A.II of [33] are reproduced in

Table 4.9. The maximum error $\|u - \tilde{u}\|_{\infty,\Omega}$ of the computed solutions obtained by RSBPM are compared with those results (Table A.II of [33]) obtained by the p-FEM coupled with Method of Auxiliary Mapping (MAM), developed by Babuška-Oh ([39]).

Moreover, from Table A.1 of [33], we observe the following results:

- $\|u - \tilde{u}\|_{\infty,\Omega} = 3.52$ at DOF$= 525,825$ using ELLPACK (second-order finite difference)
- $\|u - \tilde{u}\|_{\infty,\Omega} = 0.13$ at DOF$= 6,390$ using PLTMG6 (FEM code with adaptive mesh generation, linear elements)
- $\|u - \tilde{u}\|_{\infty,\Omega} = 6.12E-4$ at DOF$= 15,303$ using FESOP (locally developed FEM code using isoparametric quadratic elements)

These maximum errors in h-FEM and those errors in p-FEM with MAM of Table 4.9 show the effectiveness of MAM in the framework of the conventional FEM. It also implies that the conventional BEM may not be able to yield reasonable approximations when a BIE contains singularities. Therefore, we can claim that our method (RSBPM) to deal with singularity problems arising in BIEs is on a right track.

From Table 4.9, one can see that the accuracy of the proposed method seems to be less than that of p-FEM with MAM as the RPP order increases. This is because the shape functions become numerically unstable due to their oscillatory nature. In this example, particles were placed by convenience. Optimally placing the particles (including some particles which may go outside of the support of the PU functions) could improve the numerical solution to be of comparable acuracy with the MAM.

Several boundary element approaches dealing with singularities have been suggested in the literature. For example, like our method, the BEM is augmented with singular approximation functions in ([49],[58],[59]).

Table 4.8: Errors in maximum norm of q and u along the boundary of the Motz problem various RPP orders.

k	DOF		$\|u-\tilde{u}\|_{\infty,\Gamma}$	$\|q-\tilde{q}\|_{\infty,\Gamma}$
2	48	RSBPM	1.289E-0	3.996E-0
3	64	RSBPM	3.329E-2	1.553E-0
4	80	RSBPM	2.585E-3	2.688E-1
5	96	RSBPM	4.502E-4	5.557E-2
6	112	RSBPM	1.218E-4	6.317E-3
7	128	RSBPM	4.821E-5	1.555E-3
8	144	RSBPM	6.979E-6	2.876E-4
9	160	RSBPM	3.614E-6	1.563E-4
10	176	RSBPM	8.759E-7	3.645E-5

Table 4.9: Errors in maximum norm inside Ω for Motz problem various RPP orders. Patch-wise RSBPM is compared with the results of p-FEM using a mapping technique.

RSBPM			p-FEM with MAM		
RPP order k	DOF	$\|u-\tilde{u}\|_{\infty,\Omega}$	p-degree	DOF	$\|u-\tilde{u}\|_{\infty,\Omega}$
2	48	5.514E-1	2	143	8.62E-1
3	64	2.325E-2	3	247	8.10E-2
4	80	2.535E-3	4	399	1.05E-2
5	96	4.930E-4	5	599	7.56E-4
6	112	3.983E-5	6	847	8.42E-5
7	128	1.916E-5	7	1143	8.83E-6
8	144	3.444E-6	8	1487	1.00E-6
9	160	2.574E-6	9	1879	1.11E-7
10	176	6.651E-7	10	2319	2.22E-8

CHAPTER 5: MESHLESS BEM IN THREE DIMENSIONS

In this chapter, patch-wise RPBPM and RSBPM introduced previously are extended to the three dimensional Laplace equation. Once introduced, numerical examples will be presented.

5.1 Patch-wise RPBPM

We follow the same logic for the two dimensional case. Suppose $\partial\Omega = \bigcup_{k=1}^{n} F_k$ is the union of the faces of a polyhedral domain Ω. Partition each face F_k into the disjoint union of quadrangular (and if necessary triangular) patches Q_{k_j}, $j = 1, \ldots, N(k)$. On each patch, construct a partition of unity, $\Psi_{k_j}(x)$ using the generalized product partition of unity method described in section 2.3. For quadrangular patch Q_{k_j}, construct a map from a reference rectangle $\hat{R}$ into $\mathrm{supp}(\Psi_{k_j})$

$$\varphi_{k_j} : \hat{R} \to \mathrm{supp}(\Psi_{k_j})$$

such that points in $\hat{R}$ are mapped at least δ distance away from the boundary of F_k. Plant particles $\hat{\xi}_{k_{j_l}}$ and construct the Lagrange interpolation polynomials, $\hat{L}_{k_{j_l}}$, $l = 1, \ldots, M(k_j)$ in the reference domain. Physical particles and interploation functions are $x_{k_{j_l}} = \varphi_{k_j}(\hat{\xi}_{k_{j_l}})$ and $L_{k_{j_l}} = \hat{L}_{k_{j_l}} \circ \varphi_{k_j}^{-1}$, $l = 1, \ldots, M(k_j)$ respectively, as shown in Figure 5.1. Basis functions are the product of the partition of unity and the Lagrange polynomials

$$\Phi_{k_{j_l}}(x) = \Psi_{k_j}(x) \times L_{k_{j_l}}(x).$$

Upon construction of these basis functions, we follow the method described in the previous chapter.

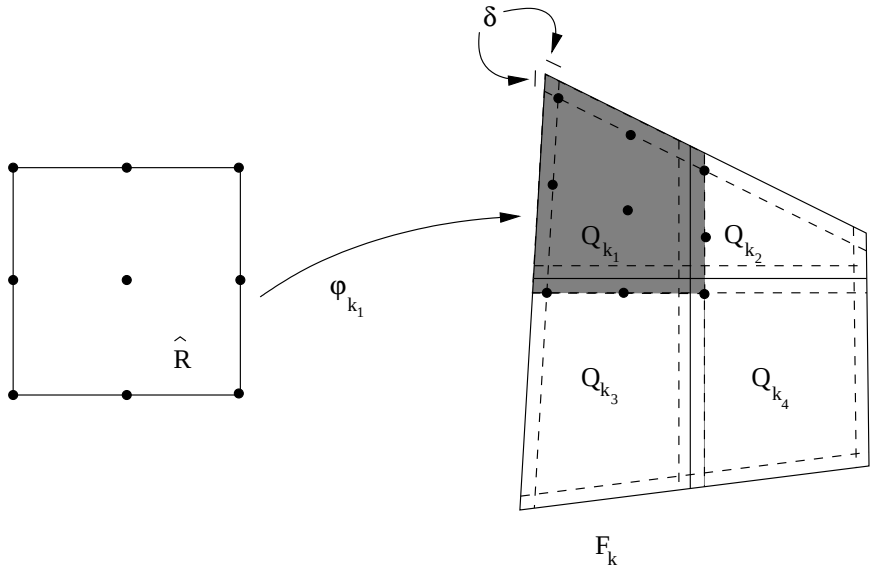

Figure 5.1: Partition of F_k into 4 quadrangular patches $Q_{k_1}, \ldots, Q_{k_4}$ and particle placement on Q_{k_1}. The mapping φ_{k_1} maps from $\hat{R}$ to Q_{k_1}. The shaded region is support of the partition of unity function Ψ_{k_1}, corresponding to the patch Q_{k_1}.

5.2 Patch-wise RSBPM

As before, follow the theory of the $d = 2$ case. That is, construct basis functions in the neighborhood of the singularity that resemble the singularity and use patch-wise RPBPM everywhere else. Suppose Ω is a polyhedral domain. Consider solutions to the Laplace equation on Ω of the form

$$u(x, y, z) = u_{\text{smooth}}(x, y, z) + u_{\text{sing}}(x, y, z)$$

where $u_{\text{smooth}}(x, y, z)$ is a smooth function and $u_{\text{sing}}(x, y, z)$ contains an edge singularity of the type

$$u_{\text{sing}}(r, \theta, z) = r^{\alpha} \sin(\alpha\theta) f(z)$$

where (r, θ, z) are the cylindrical coordinates centered at the origin, $f(z)$ is a smooth function, and $0 < \alpha < 1$. Without loss of generality, consider the case where the singularity is located along the line $r = 0$.

To deal with this singularity, partition $\partial\Omega$ into polygons such that $\partial\Omega = \bigcup_{k=1}^{n} F_k$. In partitioning $\partial\Omega$ special care is taken so that the edge singularity intersects only

the edges or vertices of any F_k. That is the singularity only appears on an edge or a vertex of a given F_k as seen in Figure 5.2. Essentially, the edge singularity is treated as an artificial boundary.

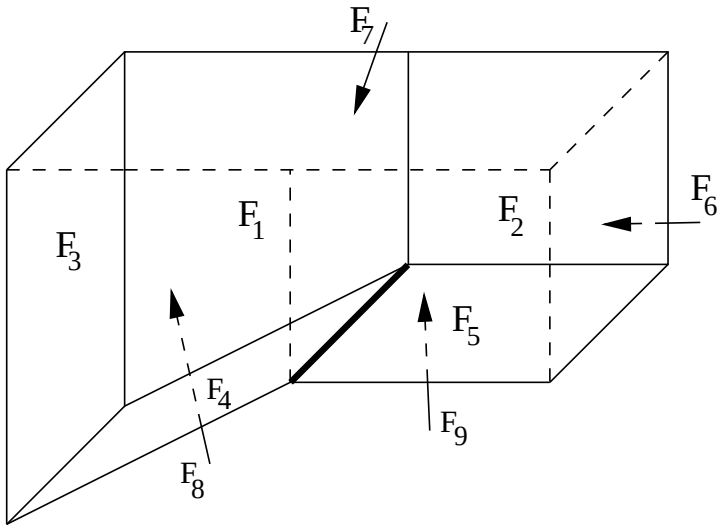

Figure 5.2: Partition of $\partial\Omega$ into $\bigcup_{k=1}^{9} F_k$ with edge singularity in bold. For $k = 1, 2, 8, 9$, the singularity appears on a vertex of F_k. For $k = 4, 5$, the singularity appears on an edge of F_k. For $k = 3, 6, 7$, the singularity does not appear on F_k.

When the singularity intersects F_k at a vertex, i.e. $k = 1, 2, 8, 9$ in Figure 5.2, use the singular map

$$T_{\text{top}}(\hat{r}, \hat{\theta}) = \left(\hat{r}^{\frac{1}{\alpha}}, \frac{\hat{\theta}}{\alpha} \right), \qquad 0 < \alpha < 1.$$

Consider F_2 which is a rectangle on the top face of Figure 5.2. In order to construct RPP shape functions of RPP order k, consider N particles $\hat{P}_j, j = 1, \ldots, N = (k+1)(k+2)/2$, that are inside the sector

$$\{(\hat{r}, \hat{\theta}) : 0 < \hat{r} < w; 0 < \hat{\theta} < \frac{\pi\alpha}{2}\},$$

in the (ξ, η) coordinate system where w is the width of the patch in the physical domain. Let $\hat{\phi}_j(\xi, \eta), j = 1, \ldots, N$, be RPP shape functions of RPP order k corresponding to these particles. That is,

$$\sum_{j=1}^{N} f(\hat{P}_j)\hat{\phi}_j(\xi,\eta) = f(\xi,\eta) \tag{5.1}$$

for any monomial $f(\xi,\eta) = \xi^{\alpha_1}\eta^{\alpha_2}$, where $0 \le \alpha_1 + \alpha_2 \le k$. Let $P_j = T_{top}(\hat{P}_j)$, $\phi_j(x,y) = \hat{\phi}_j(T_{top}^{-1}(x,y))$, for $j = 1,\ldots,N$. Then by Theorem 4.1 of [47], when $\alpha = \frac{1}{2}$, $\phi_j, j = 1,\ldots,N$, satisfy the Kronecker delta property at $P_j, j = 1,\ldots,N$, and generate the following singular functions and polynomials:

$$r^{\alpha+l}\sin(\alpha\theta + l), \quad r^{\alpha+l}\cos(\alpha\theta + l), \quad l = 0,\ldots,[k\alpha] \tag{5.2}$$

$$x^{\alpha_1}y^{\alpha_2}, \quad 0 \le (\alpha_1+\alpha_2) \le [k\alpha], \quad \alpha_1 \ge 0, \alpha_2 \ge 0, (\alpha_1,\alpha_2) \in \mathbb{Z}^2. \tag{5.3}$$

where $[k\alpha]$ is the largest integer $\le k\alpha$. See Figure 5.3.

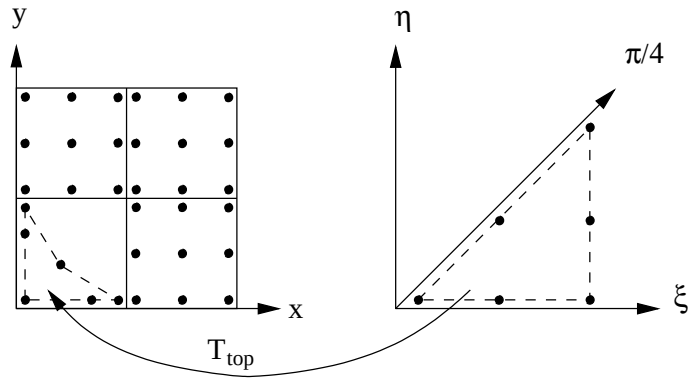

Figure 5.3: Schematic Diagram for construction of RSP shape functions on top and bottom faces to deal with the edge singularity.

When the singularity intersects F_k along an edge, i.e. $k = 4, 5$ in Figure 5.2, use the singular map

$$T_{\text{side}}(\hat{r},\hat{z}) = (\hat{r}^{\frac{1}{\alpha}},\hat{z}).$$

Consider F_5 which is a rectangle on the front face of Figure 5.2. Here, it is desirable to construct approximation functions that resemble the singularity in $u_s \approx O(r^{\alpha})$ and $\dfrac{\partial u_s}{\partial n} \approx O(r^{\alpha-1})$. Partition F_5 into 4 quadrangular patches as seen in Figure 5.4. The two patches intersecting the singularity, Q_1 and Q_3, use the singular mape T_{side} to construct RSP shape functions.

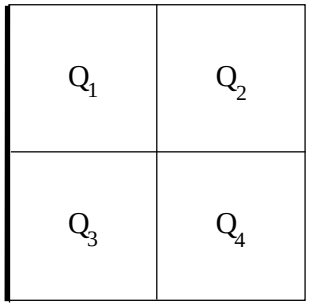

Figure 5.4: Partition of F_5 into 4 patches $Q_1, \ldots, Q_4$. Q_1 and Q_3 require the use of RSP shape functions. Q_2 and Q_4 use RPP shape functions. The edge singularity is located along the left edge

Consider $N = (k+1)^2$ particles in the (ξ, η) domain $\hat{P}_j, j = 1, \ldots, N$ and let $\hat{\phi_j}(\xi, \eta), j = 1. \ldots, N$ be the RPP shape functions of order k corresponding to these particles.

Let $P_j = T_{\text{side}}(\hat{P}_j), \phi_j(x, z) = \hat{\phi}_j(T^{-1}_{\text{side}}(x, z)), j = 1, \ldots, N$. By Theorem 4.1 of [47], when $\alpha = \frac{1}{2}$, $\phi_j, j = 1, \ldots, N$, satisfy the Kronecker delta property at $P_j, j = 1, \ldots, N$, and generate the following singular functions and polynomials:

$$x^{\alpha+l} z^{\alpha_2}, \quad 0 \leq l + \alpha_2 \leq [k\alpha] \tag{5.4}$$

$$x^{\alpha_1} z^{\alpha_2}, \quad 0 \leq \alpha_1 + \alpha_2 \leq [k\alpha] \tag{5.5}$$

where $[k\alpha]$ is the largest integer $\leq k\alpha$. Use these shape functions for u_{sing}. To construct shape functions for $\dfrac{\partial u_{\text{sing}}}{\partial n}$ use $\dfrac{\phi_j(x, z)}{x}$. For $\alpha = \frac{1}{2}$, these will generate the following singular functions and polynomials:

$$x^{\alpha+l-1} z^{\alpha_2}, \quad 0 \leq l + \alpha_2 \leq [k\alpha] \tag{5.6}$$

$$x^{\alpha_1 - 1} z^{\alpha_2}, \quad 0 \leq \alpha_1 + \alpha_2 \leq [k\alpha] \tag{5.7}$$

On all other F_k use patch-wise RPBP shape functions and proceed as described earlier.

5.3 Numerical Examples

In this section, the three-dimensional extension of RPBPM is applied to the 3-dimensional Laplace equation.

Example 5.3.1. Consider the 3-dimensional Laplace equation on a cube $\Omega = [0,1]^3$ when the true solutions are

$$u_1(r,\theta,z) = zr^4 \sin 4\theta; \quad u_2(r,\theta,z) = zr^2 \sin 2\theta; \quad u_3(r,\theta,z) = z\sqrt{r}\sin\theta/2,$$

and Dirichlet boundary conditions are imposed along $\partial\Omega$ by their true solutions. Then u_1 and u_2 are polynomials, and u_3 has an edge singularity along the z-axis.

Patch-wise RPBPM yields the results in Tables 5.1 and 5.2. In order to see the effect of adaptive particle distribution in handling the edge singularity, consider two particle distributions on the boundary: uniform distribution by dividing each face into four patches and adaptive particle distribution with adaptive partitions as shown in Figure 5.5.

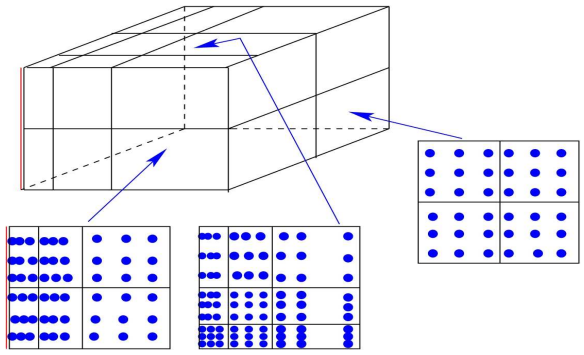

Figure 5.5: Schematic Diagram for graded boundary patches to deal with the edge singularity.

Application of 3-dimensional RPBPM to these problems gives the following:

1. Like the 2-dimensional counterpart, the traction of $u_1(x,y,z)$ and $u_2(x,y,z)$ have jumps between the faces $z = 0$ and $y = 1$ ($z = 0$ and $x = 1$). Since the true solutions are polynomials, RPBPM almost exactly captures the true traction in Tables 5.1 and 5.2. From the results in the 3rd and the 4th columns

Table 5.1: Absolute errors of computed tractions in maximum norm. q and $\tilde{q}$ are the true and the computed tractions, respectively. Each face is partitioned into four patches.

$\|q - \tilde{q}\|_{\mathrm{r},\infty}$				
Rpp order	DOF	$zr^4 \sin 4\theta$	$zr^2 \sin 2\theta$	$z\sqrt{r} \sin \theta/2$
2	216	0.240E+00	2.127E-13	0.818E+00
3	384	1.101E-12	5.107E-13	0.695E+00
4	600	7.475E-12	4.177E-12	0.522E+00

of Tables 5.1 and 5.2, one can see that the accuracy is slightly decreased, as the RPP order of approximation functions is increased because the instability of evaluations of higher degree polynomials. Notice that the local approximation functions of our methods are global polynomials truncated by partition of unity functions with flat-top to have compact support.

2. $u_3(x, y, z)$ contains an edge singularity. Applications of RPBPM to these problems do not yield any reasonable numerical solutions (the 5th columns of Tables 5.1 and 5.2). Adaptive particle distribution along the edge singularity give a small improvement (Table 5.2). However, massive adaptive particle distributions would not give a big improvement either because the gradients of partition of unity functions would be greatly increased on the patches near the singularity in such small patches. Therefore, as it was demonstrated with the two-dimensional examples, RSBPM is one of the best methods to deal with boundary integral equations containing singularities.

The results obtained by 3-dimensional RSBPM (described above) applied to Laplace's equation containing the edge singularity is given in Table 5.3. Comparing the errors in the 5th column of Table 5.2 (RPBPM with densely distributed particles along the singular edge) with those errors in the third column of Table 5.3 (3-dimensional RSBPM with RSP shape functions), one can see that RSBPM yields much more accurate results with lower degrees of freedom.

Table 5.2: Absolute errors of computed tractions in maximum norm. q and $\tilde{q}$ are the true and the computed tractions, respectively. Particles are densely planted along the singular edge as shown Figure 5.5.

$\|q - \tilde{q}\|_{\Gamma,\infty}$				
Rpp order	DOF	$zr^4 \sin 4\theta$	$zr^2 \sin 2\theta$	$z\sqrt{r} \sin \theta/2$
2	342	0.216E+00	2.975E-12	0.626E+00
3	608	9.741E-12	5.026E-12	0.532E+00
4	950	2.402E-11	1.915E-11	0.344E+00

Table 5.3: Absolute Errors of computed tractions by RSBPM in maximum norm. q and $\tilde{q}$ are the true and the computed tractions, respectively. u and $\tilde{u}$ are the true displacement and the interpolated displacement when the particles are interpolation points.

True solution is $u(x, y, z) = z\sqrt{r} \sin(\theta/2)$			
RPP order	DOF	$\|q - \tilde{q}\|_{\Gamma,\infty}$	$\|u - \tilde{u}\|_{\Gamma,\infty}$ (interpolation error)
2	210	9.383E-03	1.869E-03
3	372	8.951E-03	6.862E-04
4	580	2.881E-03	1.913E-04

Example 5.3.2. Consider the Laplace equation on the cube $[0,1]^3$ whose true solution is

$$u(x,y,z) = zr^{\alpha}\sin\alpha\theta + x^2 - y^2 + z.$$

Here $\alpha = \frac{1}{2}, r = \sqrt{x^2+y^2}, \theta = \arctan\left(\frac{y}{x}\right)$, and Dirichlet boundary conditions are imposed along $\partial\Omega$.

Here u is the sum of a singular function that has an edge singularity along the z-axis and a smooth function. The same background mesh was used as in the previous example splitting each face of the cube into four patches using RPBPM and RSBPM with RPP order 2,3 and 4. RPBPM does not produce accurate results due to the singular function. For RSBPM, notice that RPP order 2 and 3 cannot capture the solution. This is because the map T_{side} decreases the RPP order by half which disables RPP order 2 and 3 from generating 2nd degree polynomials. Therefore, with $\alpha = \frac{1}{2}$, RPP order 4 can reproduce second degree polynomials and provides the best results for this example.

Table 5.4: Results of Example 5.3.2 by using patch-wise RPBPM.

RPP order	DOF	$\|q-\tilde{q}\|_{\Gamma,\infty}$	$\|u-\tilde{u}\|_{\Gamma,\infty}$ (interpolation error)
2	216	0.798E+00	3.861E-02
3	384	0.674E+00	2.707E-02
4	600	0.504E+00	1.995E-02

Table 5.5: Results of Example 5.3.2 by using patch-wise RSBPM.

RPP order	DOF	$\|q-\tilde{q}\|_{\Gamma,\infty}$	$\|u-\tilde{u}\|_{\Gamma,\infty}$ (interpolation error)
2	210	0.711E+00	7.777E-02
3	372	0.251E+00	1.747E-02
4	580	3.884E-03	1.913E-04

Example 5.3.3. Consider the Laplace equation on the three dimensional L-shaped domain, depicted in Figure 5.6, whose true solution is

$$u(r, \theta, z) = zr^{\alpha} \sin \alpha\theta, \text{ where } \alpha = \frac{2}{3},$$

and Dirichlet boundary conditions are imposed along $\partial\Omega$. Then u has an edge singularity along the z-axis.

For this example, the top ($z = 1$) and the bottom ($z = 0$) were split into three square faces each, along with the other faces for a total of 12 faces, as shown in Figure 5.6. The faces where ($x = -1$) and ($y = -1$) were partitioned into 8 patches, the other faces were partitioned into 4 patches. The accuracy of RPBPM and RSBPM are compared with respect to using RPP order 2, 3 and 4. Notice that RSPBM outperforms RPBPM in this instance.

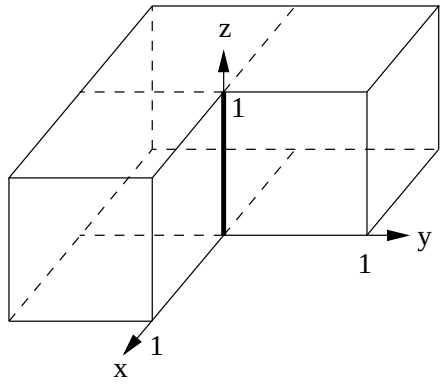

Figure 5.6: L-shaped domain for Example 5.3.3.

Table 5.6: Results of Example 5.3.3 by using patch-wise RPBPM.

RPP order k	Num. of particles	$\|q - \tilde{q}\|_{\Gamma,\infty}$	$\|u - \tilde{u}\|_{\Gamma,\infty}$ (interpolation error)
2	504	0.300	1.809E-02
3	896	0.234	1.002E-02
4	1400	0.154	6.666E-03

Example 5.3.4. Consider the Laplace equation on $[-1, 1] \times [-1, 1] \times [0, 1]$ with a crack face on the xz-axis where $x \geq 0$, as seen in Figure 5.7. The true solution is

Table 5.7: Results of Example 5.3.3 by using patch-wise RSBPM.

RPP order k	Num. of particles	$\|q - \tilde{q}\|_{\Gamma,\infty}$	$\|u - \tilde{u}\|_{\Gamma,\infty}$ (interpolation error)
2	485	7.005E-02	2.166E-03
3	860	1.052E-02	5.362E-04
4	1340	4.248E-03	1.318E-04

$$u(r, \theta, z) = zr^{\alpha} \sin \alpha\theta, \text{ where } \alpha = \frac{1}{2}$$

and Dirichlet boundary conditions are imposed along $\partial\Omega$. Then u has an edge singularity along the z-axis.

For a cracked domain, in general, u may have a jump discontinuity along the positive x-axis. Thus, using the BIE for this domain will not be able to produce a solution. For this reason, split Ω along the plane $y = 0$ into Ω_1 and Ω_2 and treat them as separate domains, as shown infigure 5.8. Let $u_1(x)$ be the solution inside Ω_1 and $u_2(x)$ be the solution in Ω_2 and divide $\partial\Omega_1$ and $\partial\Omega_2$ into eight squares and one rectangle each, the same way as was done in Figure 5.2. Compute the coefficient matrices for each sub-domain. On the interface, assume the interface condition:

$$\begin{aligned} u_1|_{\text{interface}} &= u_2|_{\text{interface}}, \\ \frac{\partial u_1}{\partial n}|_{\text{interface}} &= \frac{\partial u_2}{\partial n}|_{\text{interface}}. \end{aligned}$$

Dirichlet boundary conditions were imposed everywhere on each sub-domain, except for the interface where the above two interface conditions were used. Then, the linear system was solved for $\frac{\partial u_1}{\partial n}$ and $\frac{\partial u_2}{\partial n}$. Each square face was divided into 4 patches and the rectangles were divided into 8 patches. The results are presented using RSBPM and RPBPM with RPP order 2, 3 and 4.

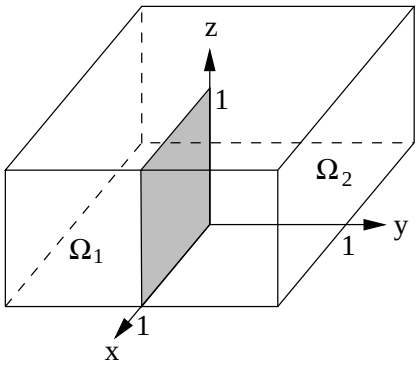

Figure 5.7: Cracked domain for Example 5.3.4. The shaded area is the location of the crack.

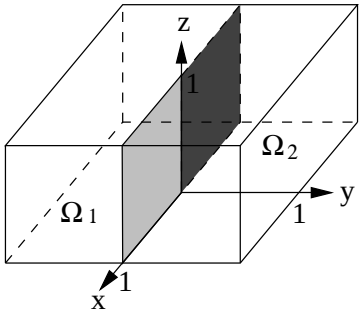

Figure 5.8: Cracked domain for Example 5.3.4. The darker shaded area is the location of the interface between Ω_1 and Ω_2.

Table 5.8: Results of Example 5.3.4 by using patch-wise RPBPM.

RPP order k	Num. of particles	$\|q-\tilde{q}\|_{\Gamma,\infty}$	$\|u-\tilde{u}\|_{\Gamma,\infty}$ (interpolation error)
2	720	0.702E+00	4.716E-02
3	1280	0.573E+00	4.127E-02
4	2000	0.383E+00	3.464E-02

Table 5.9: Results of Example 5.3.4 by using patch-wise RSBPM.

RPP order k	Num. of particles	$\|q-\tilde{q}\|_{\Gamma,\infty}$	$\|u-\tilde{u}\|_{\Gamma,\infty}$ (interpolation error)
2	696	1.971E-02	2.902E-03
3	1232	1.091E-02	8.051E-04
4	1920	5.301E-03	1.913E-04

CHAPTER 6: HELMHOLTZ EQUATION IN TWO DIMENSIONS

We will now move to another type of elliptic equation in $\mathbb{R}^2$, Helmholtz equation. Helmholtz equation is sometimes called the reduced wave equation because it is the governing equation for time harmonic wave equations. We will investigate the numerical solution of Helmholtz equation with regards to polygonal and circular domains.

Let Ω be a bounded domain with boundary Γ assumed to be piecewise smooth. For wave number k, Helmholtz equation is the following:

$$\Delta u(x) + k^2 u(x) = 0 \quad in \quad \Omega. \tag{6.1}$$

The fundamental solution, $G_k(x, P) = \frac{i}{4} H_0^{(1)}(k|x-P|)$, of Helmholtz equation satisfies

$$\Delta G_k(x, P) + k^2 G_k(x, P) = -\delta(x - P). \tag{6.2}$$

Where $H_0^{(1)}(z)$ is the Hankel function of order zero of the first kind.

$$H_n^{(1)}(z) = J_n(z) + iY_n(z)$$

Where $J_n(z)$ and $Y_n(z)$ are the Bessel functions of the first and second kinds respectively. For integer n, $J_n(z)$ has the power series representation

$$J_n(z) = \sum_{m=0}^{\infty} \frac{(-1)^m}{m!(m+n)!} \left(\frac{z}{2}\right)^{2m+n}$$

and contains no singularities. For integer n, $Y_n(z)$ has the power series representation

$$\begin{aligned} Y_n(z) &= \frac{2}{\pi} J_n(z) \left(\ln \frac{z}{2} + \gamma\right) - \frac{1}{\pi} \sum_{m=0}^{n-1} \frac{(n-m-1)!}{m!} \left(\frac{z}{2}\right)^{2m-n} \\ &+ \frac{1}{\pi} \sum_{m=1}^{\infty} \frac{(-1)^{m-1} \left(H_m + H_{m+n}\right)}{m!(m+n)!} \left(\frac{z}{2}\right)^{2m+n}, \end{aligned}$$

where $\gamma = 0.57721$ is the Euler-Mascheroni constant and $H_n = \sum_{m=1}^{n} \frac{1}{m}$ is a harmonic number. Notice that Y_n has a logarithmic singularity at the origin causing $H_n^{(1)}$ to

have a logarithmic singularity at the origin. It will be useful to extract this logarithmic singularity away from everything else by using this formula

$$Y_n(z) = \frac{2}{\pi} J_n(z) \ln z + f(z). \tag{6.3}$$

Here, $f(z)$ represents everything else not multiplied by the logarithm.

This is the same kind of singularity that the fundamental solution of Laplace's equation contains. Now, note that $u(x)$ and $G_k(x, P)$ satisfy the same BIE as the Laplace equation:

$$c(P)u(P) = \int_\Gamma \frac{\partial u(x)}{\partial n} G_k(x, P) ds(x) - \int_\Gamma \frac{\partial G_k(x, P)}{\partial n} u(x) ds(x),$$

where

$$c(P) \quad = \quad \begin{cases} 0 & \text{if } P \notin \Omega \\ 1 & \text{if } P \in \Omega \\ \frac{1}{2} & \text{if } P \in \Gamma \text{ and } \Gamma \text{ is smooth at } P \\ \frac{\alpha}{2\pi} & \text{if } P \in \Gamma \text{ and } \Gamma \text{ is not smooth at } P \end{cases}$$

and $\mathbf{n}$ is the outward unit normal vector.

Now we will suppose we have a parameterization of the boundary $x(t)$ where $t \in [a, b]$. Set $r(t, s) = |x(t) - x(s)|$ where $x(s) = P$. Denote $\tilde{f}(t) = f(x(t))$ and set $q(x) = \frac{\partial u}{\partial n}(x)$. Then we can see the fundamental solution in parameter space as

$$\tilde{G}_k(t, s) = \frac{i}{4} H_0^{(1)}(kr(t, s))$$

and its normal derivative

$$\frac{\partial \tilde{G}_k}{\partial n}(t, s) = -\frac{ik}{4} H_1^{(1)}(kr(t, s)) \frac{\partial r(t, s)}{\partial n}.$$

Let us now define the layer potential integral operators, the single layer potential

$$Sq(P) := \int_\Gamma G_k(x, P) q(x) ds(x) = \int_a^b \tilde{G}_k(t, s) \tilde{q}(t) |x'(t)| dt$$

and the double layer potential

$$Du(P) := \int_\Gamma \frac{\partial G_k(x,P)}{\partial n} u(x) ds(x) = \int_a^b \frac{\partial \tilde{G}_k}{\partial n}(t,s)\tilde{u}(x)|x'(t)|dt.$$

For ease of notation and calculation we will introduce a splitting of the kernels into singular and nonsingular parts for specific domains. Now, the BIE can be written in a much more compact form

$$c(P)u(P) + Du(P) = Sq(P).$$

We will be approximating the solution of this BIE using a collocation method. We will discretize u and q to approximate the solution of the BIE of Helmholtz equation under various circumstances. So consider the particles y_i corresponding to the particle basis functions $\phi_i(x)$ introduced in chapter 4, for $i = 1, \ldots,$ DOF. We will then approximate $u(x) \approx \sum_{i=1}^{\text{DOF}} u_i\phi_i(x)$ and $q(x) \approx \sum_{i=1}^{\text{DOF}} q_i\phi_i(x)$. Most of the time we are concerned with complex valued solutions so in this case u_i and $q_i \in \mathbb{C}$. Then, the discrete BIE is

$$\sum_{i=1}^{\text{DOF}} \left(c(P)\phi_i(P) + D\phi_i(P)\right) u_i = \sum_{i=1}^{\text{DOF}} S\phi_i(P)q_i.$$

Next, we will look at how we can accurately compute the double and single layer potentials for polygonal and circular domains.

6.1 Polygonal Domains

Consider a polygon Ω with boundary $\Gamma = \cup_{k=1}^n \Gamma_k$ where $\Gamma_k = (x_k - x_{k-1})t + x_{k-1}$ where $t \in [0,1]$ and x_k are the n vertices of the polygon Ω. Denote $L_k = |x_k - x_{k-1}|$. We wish to use patch-wise RPP shape functions to approximate the solution of the BIE of Helmholtz equation. Construction of particles and their corresponding particle shape functions are similar to those for the Laplace equation. The only thing that differs is the computation of the integrals.

6.1.1 Single Layer Potential

Now, lets examine the computation of the single layer potential. Consider the approximation function $f(x)$ where $\text{supp}(f) \subset \Gamma_j$ and the particle $P \in \Gamma$. Using the parameterization of Γ_j we have the following:

$$\begin{aligned} Sf(P) &= \int_{\Gamma_j} G_k(x,P) f(x) ds(x) \\ &= \int_0^1 \frac{i}{4} H_0^{(1)}(k|x(t)-P|) \tilde{f}(t) L_j dt. \end{aligned}$$

If $P \notin \text{supp}(f)$, then there is no singularity and we may use the standard Gaussian quadrature to compute this integral. If $P \in \text{supp}(f)$, using the parameterization of Γ_j and setting $P = x(s)$, we partition the integration region as follows

$$\begin{aligned} Sf(P) &= \int_0^1 \frac{i}{4} H_0^{(1)}(kr(t,s)) \tilde{f}(t) L_j dt \\ &= \int_0^s \frac{i}{4} H_0^{(1)}(kr(t,s)) \tilde{f}(t) L_j dt + \int_s^1 \frac{i}{4} H_0^{(1)}(kr(t,s)) \tilde{f}(t) L_j dt \\ &:= I_1(s) + I_2(s). \end{aligned}$$

Now each integral has a singularity at one endpoint of the interval. Just consider the first integral $I_1(s)$, the second will follow the same logic. On this interval, we will change variables $u = \frac{s-t}{s}$ and then we may write

$$r(t,s) = |x(t) - x(s)| = |L_j t + x_{j-1} - (L_j s + x_{j-1})| = L_j |t-s| = L_j s u.$$

Then the integral becomes

$$I_1(s) = \int_0^1 \frac{i}{4} H_0^{(1)}(kL_j s u) \tilde{f}(s(1-u)) L_j s du.$$

Notice that the singularity is now at the point $u = 0$. Now we will split the kernel of the integral into singular and nonsingular parts. We want to exploit the fact that Y_0 has a logarithmic singularity. By (6.3), we write the kernel

$$K(u,s) = \frac{iL_j s}{4} H_0^{(1)}(kL_j s u) = K_1(u,s) \ln u + K_2(u,s),$$

where

$$\begin{aligned} K_1(u,s) &= -\frac{L_j s}{2\pi} J_0(L_j k s u), \\ K_2(u,s) &= K(u,s) - K_1(u,s)\ln u. \end{aligned}$$

$K_1(u,s)$ and $K_2(u,s)$ are analytic and it just remains to see what happens when $u = 0$. From the power series form of $Y_0(z)$ we see $K_2(u,s)$ has the form

$$\begin{aligned} K_2(u,s) = \left(\frac{iL_j s}{4} - \frac{L_j s}{2\pi}\left(\gamma + \ln\frac{L_j k s}{2}\right)\right) J_0(L_j k s u) \\ + \frac{2}{\pi}\sum_{m=1}^{\infty} \frac{(-1)^{m-1} H_m}{m!^2}\left(\frac{L_j k s u}{2}\right)^{2m}. \end{aligned}$$

Now, we can easily see that

$$\begin{aligned} K_1(0,s) &= -\frac{L_j s}{2\pi}, \\ K_2(0,s) &= \frac{L_j s}{4}\left(i - \frac{2}{\pi}\left(\gamma + \ln\frac{k L_j s}{2}\right)\right). \end{aligned}$$

If we let $g(u) = \tilde{f}(s(1-u))$, then

$$\begin{aligned} I_1(s) &= \int_0^1 K(u,s) g(u) du \\ &= \int_0^1 K_1(u,s) g(u) \ln u du + \int_0^1 K_2(u,s) g(u) du \\ &\approx \sum_{k=1}^{N_{lg}} K_1(U_k, s) g(U_k) W_k + \sum_{k=1}^{N_g} K_2(u_k, s) g(u_k) w_k, \end{aligned}$$

where N_g and N_{lg} are the number of Gaussian quadrature and logarithmic quadrature points respectively, u_k and U_k are the Gaussian quadrature and logarithmic Gaussian quadrature points respectively, and w_k and W_k are the weights for Gaussian quadrature and logarithmic Gaussian quadrature points respectively. We may compute $I_2(s)$ in a similar way and after that, we can compute the single layer potential.

Using this, for boundary patricles P_j and patch-wise RPP shape functions ϕ_k, we will compute the matrix $\mathcal{S} = [(\mathcal{S}_{j,k})]$ that approximates the single layer potential where $j, k = 1, \ldots, \text{DOF}$ and

$$\mathcal{S}_{j,k} = S\phi_k\left(P_j\right).$$

6.1.2 Double Layer Potential

Consider the approximation function $f(x)$ where $\text{supp}(f) \subset \Gamma_j$ and the particle $P \in \Gamma_i$. Using the parameterization of Γ_j we see the following:

$$\begin{aligned} Df(P) &= \int_{\Gamma_j} \frac{\partial G_k}{\partial n}(x,P) f(x) ds(x) \\ &= \int_0^1 -\frac{ik}{4} H_1^{(1)}(k|x(t)-P|) \frac{\partial |x(t)-P|}{\partial n} \tilde{f}(t) L_j dt. \end{aligned}$$

There are only two cases to consider. If $j \neq i$, then there is no singularity since P is not on Γ_j and the integration may be computed using the standard Gaussian quadrature. If $j = i$, $Df(P) = 0$ since $\frac{\partial |x-P|}{\partial n} = 0$ when the field and source point are on the same segment. Using this, for boundary patricles P_j and patch-wise RPP shape functions ϕ_k, we will compute the matrix $\mathcal{D} = [(\mathcal{D}_{j,k})]$ that approximates the double layer potential where $j, k = 1, \ldots, \text{DOF}$ and

$$\mathcal{D}_{j,k} = D\phi_k\left(P_j\right).$$

For the both the single and double layer potentials in the polygonal domain, it should be noted that when the source point and field point are close to each other but not on the same boundary, the integral becomes almost singular and the accuracy of numerical integration decreases. To overcome this, we have tried increasing the number of integration points and subdividing the integration interval. Both are effective, but computationally inefficient.

6.2 Circular Domains

Immediately, we run into some problems with the circular domain. First, the boundary is now curved and no longer piecewise linear. This leads to a different type of logarithmic singularity that the logarithmic Gaussian quadrature rule cannot

handle so well. This also leads to having to deal with a singularity in the double layer potential. Another problem has to do with the approximation of periodic functions with RPP basis functions.

6.2.1 Particle Shape Functions

The meshfree particle shape functions introduced thus far usually generate polynomials in the reference domain i.e. the parameter space. Therefore, on a circle with radius R centered at the origin, we may parameterize it in the usual fashion $x(t) = (R\cos t, R\sin t)$ for $t \in [0, 2\pi]$. Then, these basis functions would generate polynomials in t, that is $1, t, t^2, \ldots, t^N$. For any function $f(x, y)$, on the boundary of the circle, the function is $f(R\cos t, R\sin t)$. We need to have basis functions that are better suited to approximate trigonometric functions.

Meshfree shape functions can approximate triginometric functions but must use a high RPP order. From ([12]), it was shown that

$$\phi_\infty(x) = \lim_{K\to\infty} \phi_{[-K,K],0,2K-1}(x) = \frac{\sin(\pi x)}{\pi x}. \tag{6.4}$$

Using (6.4) and complex variables,

$$\Psi_N(x) = \frac{\sin \pi x \cot \frac{\pi x}{N}}{N}$$

was developed. $\Psi_N(x)$ can be considered a meshfree trigonometric shape function. To use this basis function, we will place equally spaced nodes in $[0, 2\pi)$ such that $h = \frac{2\pi}{N}$ and $t_j = jh$ where $j = 0, \ldots, N-1$. Then we define

$$\psi_j(t) = \Psi_N\left(\frac{t}{h} - j\right), \qquad j = 0, \ldots, N-1.$$

It should be noted that this function is identical to the Lagrange basis for trigonometric interpolation with equally spaced nodes. These functions have the desired Kronecker delta property and have the ability to approximate trigonometric functions on the circle. However, they no longer have compact support.

For this parameterization of the circle, for any point $x = (R\cos t, R\sin t) = c(t)$

on the boundary of the circle and $P = (Q\cos s, Q\sin s)$ inside the circle we may write

$$|x - P| = \sqrt{R^2 + Q^2 - 2RQ\cos(t-s)}$$

and since the normal direction is in the radial direction we may write

$$\frac{\partial|x-P|}{\partial n} = \frac{\partial|x-P|}{\partial R} = \frac{R - Q\cos(t-s)}{|x-P|}.$$

As P moves to the boundary we may simplify these expressions and write

$$r(t,s) = \quad 2R \quad \left|\sin\left(\frac{t-s}{2}\right)\right|$$

$$\frac{\partial r(t,s)}{\partial n} = \qquad \left|\sin\left(\frac{t-s}{2}\right)\right|.$$

Since these approximation functions are no longer polynomials but trig functions, it is more useful to use the trapezoidal integration scheme verses Gaussian quadrature. Another nice thing about having periodic basis functions on a circular domain is that the matrices discretizing the single and double layer potentials become circulant, meaning we only need to compute one row of each, which will save a lot of computational expense. Following the same idea as in ([19]), we will examine the layer potentials.

6.2.2 Single Layer Potential

For the circle of radius R, and boundary node $P = c\left(\frac{2\pi s}{N}\right)$, let the kernel of the operator be defined as

$$L(t,s) := \frac{iR}{4}H_0^{(1)}(kr(t,s)).$$

For the approximation function $f(x)$, the single layer potential takes the form

$$Sf(P) \quad = \quad \int_0^{2\pi} L(t,s)\tilde{f}(t)dt.$$

We wish to decompose the kernel into singular and nonsingular parts. Knowing the structure of the logarithmic singularity which comes from the bessel function of the second kind and (6.3), we set

$$L(t,s) := L_1(t,s)\ln\left(4\sin^2\left(\frac{t-s}{2}\right)\right) + L_2(t,s),$$

where

$$\begin{aligned} L_1(t,s) &:= -\frac{R}{4\pi}J_0(kr(t,s)), \\ L_2(t,s) &:= L(t,s) - L_1(t,s)\ln\left(4\sin^2\left(\frac{t-s}{2}\right)\right). \end{aligned}$$

$L_1(t,s)$ and $L_2(t,s)$ are actually analytic, but we need to check what values they have when $t = s$ in particular, $L_2(t,s)$. Using the power series expansion of $Y_0(z)$ we see that $L_2(t,s)$ has the form

$$\begin{aligned} L_2(t,s) = \frac{R}{2}\left(\frac{i}{2} + \frac{1}{\pi}\left(\ln\left(\frac{2}{Rk}\right) - \gamma\right)\right)J_0(kr(t,s)) \\ -\frac{R}{2\pi}\sum_{m=1}^{\infty}\frac{(-1)^{m-1}H_m}{m!^2}\left(\frac{kr(t,s)}{2}\right)^{2m}. \end{aligned}$$

From this formula and above, one can see that as t approaches s:

$$\begin{aligned} L_1(s,s) &= -\frac{R}{4\pi}, \\ L_2(s,s) &= \frac{R}{2}\left(\frac{i}{2} + \frac{1}{\pi}\left(\ln\left(\frac{2}{Rk}\right) - \gamma\right)\right). \end{aligned}$$

For integration, we will use the trapezoidal rule. That is for any periodic function $f(t)$

$$\int_0^{2\pi} f(t)dt \approx \frac{\pi}{n}\sum_{j=0}^{2n-1} f(t_j),$$

where $t_j = \frac{\pi j}{n}$, and $j = 0, 1, \ldots, 2n-1$. To handle the singularity, we employ a the quadrature rule found in ([19]):

$$\int_0^{2\pi} f(t)\ln\left(4\sin^2\left(\frac{t-s}{2}\right)\right)dt \approx \sum_{j=0}^{2n-1} R_j^{(n)}(s)f(t_j) \text{ where } 0 \le s \le 2\pi,$$

where

$$R_j^{(n)}(s) = -\frac{2\pi}{n}\sum_{m=1}^{n-1}\frac{1}{m}\cos m(s-t_j) - \frac{\pi}{n^2}\cos n(s-t_j) \text{ where } j = 0, 1, \ldots, 2n-1.$$

Using all of these tools, we can compute the single layer potential.

$$\begin{aligned} Sf(P) &= \int_0^{2\pi} L(t,s)\tilde{f}(t)dt \\ &= \int_0^{2\pi} L_1(t,s)\ln\left(4\sin^2\left(\frac{t-s}{2}\right)\right)\tilde{f}(t)dt + \int_0^{2\pi} L_2(t,s)\tilde{f}(t)dt \\ &\approx \sum_{j=0}^{2n-1}\left(R_j^{(n)}(s)L_1(t_j,s) + \frac{\pi}{n}L_2(t_j,s)\right)f(t_j). \end{aligned}$$

Now, for boundary particles P_j and meshfree shape functions ψ_k, we will compute the matrix $\mathcal{S} = [\mathcal{S}_{j,k}]$ that approximates the single layer potential where $j, k = 0, 1, \ldots, N-1$ and

$$\mathcal{S}_{j,k} = S\psi_k(P_j).$$

Since $\mathcal{S}$ is a circulant matrix, only the first row corresponding to $P_j = 0$ needs to be computed. This relation gives

$$\mathcal{S} = \begin{bmatrix} \mathcal{S}_{0,0} & \mathcal{S}_{0,1} & \ldots & \mathcal{S}_{0,N-2} & \mathcal{S}_{0,N-1} \\ \mathcal{S}_{0,N-1} & \mathcal{S}_{0,0} & \ldots & \mathcal{S}_{0,N-3} & \mathcal{S}_{0,N-2} \\ \ldots & & & & \\ \ldots & & & & \\ \mathcal{S}_{0,1} & \mathcal{S}_{0,2} & \ldots & \mathcal{S}_{0,N-1} & \mathcal{S}_{0,0} \end{bmatrix}.$$

6.2.3 Double Layer Potential

For the circle of radius R, and boundary node $P = c\left(\frac{2\pi s}{N}\right)$, let the kernel of the double layer potential operator be defined as

$$K(t,s) := -\frac{ikR}{4}H_1^{(1)}(kr(t,s))\frac{\partial r(t,s)}{\partial n}.$$

For the approximation function $f(x)$, the double layer potential takes the form

$$Df(P) \;=\; \int_0^{2\pi} K(t,s)\tilde{f}(t)dt.$$

We wish to decompose the kernel into singular and nonsingular parts. Knowing the structure of the logarithmic singularity which comes from from the bessel function of the second kind and (6.3), we set

$$K(t,s) := K_1(t,s)\ln\left(4\sin^2\left(\frac{t-s}{2}\right)\right) + K_2(t,s)$$

where

$$\begin{aligned} K_1(t,s) &:= \frac{kR}{4\pi}J_1(kr(t,s))\frac{\partial r(t,s)}{\partial n} \\ K_2(t,s) &:= K(t,s) - K_1(t,s)\ln\left(4\sin^2\left(\frac{t-s}{2}\right)\right) \end{aligned}$$

$K_1(t,s)$ and $K_2(t,s)$ are actually analytic, but we need to check what values they have when $t = s$ in particular, $K_2(s,s)$. Clearly $K_1(s,s) = 0$ and since

$$\lim_{z\to 0} zH_1^{(1)}(z) = \frac{2}{i\pi}$$

we deduce that

$$K_2(s,s) \;=\; -\frac{1}{4\pi}.$$

For integration, we will use the trapezoidal rule following the same steps as for the single layer potential. Using all of these tools, we can compute the double layer potential.

$$\begin{aligned} Df(P) &= \int_0^{2\pi} K(t,s)\tilde{f}(t)dt \\ &= \int_0^{2\pi} K_1(t,s)\ln\left(4\sin^2\left(\frac{t-s}{2}\right)\right)\tilde{f}(t)dt + \int_0^{2\pi} K_2(t,s)\tilde{f}(t)dt \\ &\approx \sum_{j=0}^{2n-1}\left(R_j^{(n)}(s)K_1(t_j,s) + \frac{\pi}{n}K_2(t_j,s)\right)f(t_j) \end{aligned}$$

For boundary particles P_j and meshfree shape functions ψ_k, we will compute the ma-

trix $\mathcal{D} = [\mathcal{D}_{j,k}]$ that approximates the single layer potential where $j, k = 0, 1, \ldots, N-1$ and

$$\mathcal{D}_{j,k} = D\psi_k(P_j).$$

Since $\mathcal{D}$ is a circulant matrix, only the first row corresponding to $P_j = 0$ needs to be computed. This relation gives

$$\mathcal{D} = \begin{bmatrix} \mathcal{D}_{0,0} & \mathcal{D}_{0,1} & \ldots & \mathcal{D}_{0,N-2} & \mathcal{D}_{0,N-1} \\ \mathcal{D}_{0,N-1} & \mathcal{D}_{0,0} & \ldots & \mathcal{D}_{0,N-3} & \mathcal{D}_{0,N-2} \\ \ldots & & & & \\ \ldots & & & & \\ \mathcal{D}_{0,1} & \mathcal{D}_{0,2} & \ldots & \mathcal{D}_{0,N-1} & \mathcal{D}_{0,0} \end{bmatrix}.$$

6.3 Photonic crystals

A photonic crystal is a low-loss periodic dielectric medium that can be used for optical control and manipulation. People design and construct photonic crystals with photonic band gaps which prevent propagation of waves with certain frequencies. In order for a photonic crystal to have a photonic band gap, the crystal should be designed with some periodicity creating a lattice type of structure([18]). We will now consider the propagation of electromagnetic waves through a two dimensional lattice of photonic crystals in which the direction of propagation is in the xy-plane. Consider a lattice of photonic crystal cylinders and a plane wave propagating in the direction $(1, 0)$, see Figure 6.1.

Certain frequencies of light will be blocked from passing through this lattice. If some rods are removed, defects in the lattice are created and the waves will begin to propagate where the rods were removed. People use this idea to create photonic nanodevices such as waveguides. Mathematically, we may consider each cylinder a domain Ω_i and the space outside the cylinders $\Omega_{\text{ext}} = (\cup\Omega_i)^c$.

The governing equations of electromagnetic scattering by photonic crystals in the frequency domain are the time harmonic Maxwell's equations

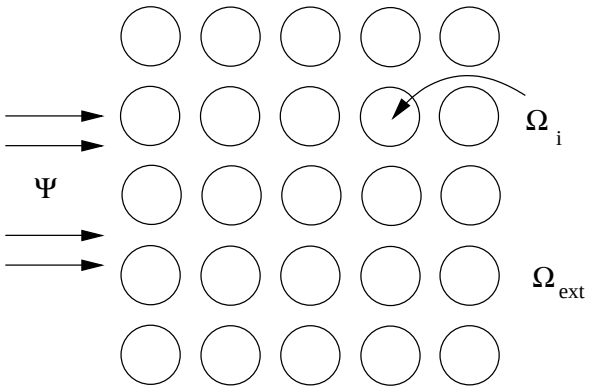

Figure 6.1: Sketch of a plane wave, Ψ, and a photonic crystal lattice.

$$\nabla \times \mathbf{E}(x) = \frac{i\omega}{c}\mathbf{H}(x) \tag{6.5}$$

$$\nabla \times \mathbf{H}(x) = -\frac{i\omega}{c}\varepsilon(x)\mathbf{E}(x) \tag{6.6}$$

$$\nabla \cdot \mathbf{E} = 0 \tag{6.7}$$

$$\nabla \cdot \mathbf{H} = 0 \tag{6.8}$$

where $\mathbf{E}$ is the electric field, $\mathbf{H}$ is the magnetic field, c is the speed of light in a vacuum, ε is the dielectric permittivity. For transverse magnetic (TM) waves one can deduce that $\mathbf{E} = (0, 0, E_z)$ and $\mathbf{H} = (H_x, H_y, 0)$, and for transverse electric (TE) waves one can deduce that $\mathbf{E} = (E_x, E_y, 0)$ and $\mathbf{H} = (0, 0, H_z)$. For both of these cases, Maxwell's equations reduce to Helmholtz equation

$$\Delta u + \varepsilon k^2 u = 0$$

where $k = \frac{\omega}{c}$.

In Ω_{ext} the total wave u_{ext} satisfies the Helmholtz equation with the wave number k_{ext}. Here, the total wave is as follows:

$$u_{\text{ext}} = u_{\text{inc}} + u_{\text{sc}}, \tag{6.9}$$

where u_{inc} is the incident wave and u_{sc} is the scattered wave respectively, each of which also satisfies Helmholtz equation with k_{ext}. The scattered wave also satisfies the Sommerfield radiation condition

$$\lim_{r\to\infty}\sqrt{u_{\rm sc}}\left(\frac{\partial u_{\rm sc}}{\partial n}-iku_{\rm sc}\right)=0$$

which guarantees the scattered wave is outgoing.

In Ω_i the total wave u^i satisfies the Helmholtz equation with wave number k_i.

On the interface between the cylinders Ω_i and the exterior we have the following boundary conditions.

$$\begin{aligned} u_{\rm ext} &= u^i \quad \text{and} \\ \frac{\partial u_{\rm ext}}{\partial n} &= \nu^{-1}\frac{\partial u^i}{\partial n} \end{aligned}$$

$i=1,\ldots,{\rm N_D}$. Where $\nu=1$ for TM waves and $\nu=\frac{\varepsilon_{\rm int}}{\varepsilon_{\rm ext}}$ for TE waves. Now let us develop the BIEs for lattices of photonic crystals.

6.3.1 Exterior Field

In what follows, we let $\mathbf{u}=[u_1,u_2,\ldots,u_{\rm DOF}]^T$ where $u_j=u(P_j)$ is the value of u at boundary node P_j. Outside of the cylinders we have the boundary integral equation for $u=u_{\rm ext}$

$$c(P)u(P)-\int_{\partial\Omega_{\rm ext}}\frac{\partial G_k}{\partial n}(x,P)u(x)ds(x)+\int_{\partial\Omega_{\rm ext}}\frac{\partial u}{\partial n}(x)G_k(x,P)ds(x)=0,$$

where the signs on the single and double layer potentials have changed due to the fact that we are in an unbounded domain and we are using the convention that the normals are pointing outward. $\partial\Omega_{\rm ext}=\cup\partial\Omega_i$ which means we can expand the BIE into

$$c(P)u(P)-\sum_{i=1}^{\rm N_D}\int_{\partial\Omega_i}\frac{\partial G_k}{\partial n}(x,P)u(x)ds(x)+\sum_{i=1}^{\rm N_D}\int_{\partial\Omega_i}\frac{\partial u}{\partial n}(x)G_k(x,P)ds(x)=0.$$

Let $q=\frac{\partial u}{\partial n}$ and then move back to the integral operator notation and set

$$\begin{aligned} D_iu(P) &= \int_{\Omega_i}\frac{\partial G_k}{\partial n}(x,P)u(x)ds(x) \quad \text{and} \\ S_iq(P) &= \int_{\Omega_i}G_k(x,P)\frac{\partial u}{\partial n}(x)ds(x), \end{aligned}$$

so that the BIE is now

$$c(P)u(P) - \sum_{i=1}^{\mathrm{N_D}} D_i u(P) + \sum_{i=1}^{\mathrm{N_D}} S_i q(P) = 0.$$

Let $u(x) = \sum_{j=1}^{\mathrm{N_D}} \sum_{k=1}^{\mathrm{DOF}} \phi_{j_k}(x) u_{j_k}$ and $q(x) = \sum_{j=1}^{\mathrm{N_D}} \sum_{k=1}^{\mathrm{DOF}} \phi_{j_k}(x) q_{j_k}$ and let $P = y_{lm}$ be the particles, where $l = 1, \ldots, \mathrm{N_D}$,$m = 1, \ldots, \mathrm{DOF}$. Upon plugging this in we use the fact that the particle shape functions $\phi_{j_k}(x)$ satisfy the Kronecker delta property, each shape function is only defined on one circle, and since the nodes are on the boundary, $c(P) = \frac{1}{2}$ and hence we have the following:

$$\frac{1}{2} \sum_{i=1}^{\mathrm{N_D}} \sum_{k=1}^{\mathrm{DOF}} \delta_{(lm)(ik)} u_{ik} - \sum_{i=1}^{\mathrm{N_D}} \sum_{k=1}^{\mathrm{DOF}} D_i \phi_{ik}(y_{lm}) u_{ik} + \sum_{i=1}^{\mathrm{N_D}} \sum_{k=1}^{\mathrm{DOF}} S_i \phi_{ik}(y_{lm}) q_{ik} = 0.$$

We can now represent the BIE as a $(\mathrm{N_D} \times \mathrm{N_D})$ block matrix equation with blocks of $(\mathrm{DOF} \times \mathrm{DOF})$ as follows:

$$\left(\frac{1}{2} I - \mathcal{D}_{\mathrm{ext}}\right) \mathbf{u} + \mathcal{S}_{\mathrm{ext}} \mathbf{q} = 0, \tag{6.10}$$

where the blocks are

$$\mathcal{D}_{\mathrm{ext}}(a,b) = [D_b \phi_{bm}(y_{an})] \text{ and } \mathcal{S}_{\mathrm{ext}}(a,b) = [S_b \phi_{bm}(y_{an})],$$

$$\text{where } a, b = 1, \ldots, \mathrm{N_D} \quad \text{and } m, n = 1, \ldots, \mathrm{DOF}.$$

Note that when $a = b$, these integrations are singular and hence the operator splitting techniques mentioned above should be followed. Also note, one can also exploit the symmetries of the lattice and save computational cost by doing so.

6.3.2 Interior Field

For the interior field we have the following BIE for $u = u^i$ in each cylinder

$$c(P)u(P) + \int_{\partial\Omega_i} \frac{\partial G_k}{\partial n}(x,P) u(x) ds(x) - \int_{\partial\Omega_i} \frac{\partial u}{\partial n}(x) G_k(x,P) ds(x) = 0,$$

where $i = 1, \ldots, \mathrm{N_D}$. In operator form, this becomes

$$c(P)u(P) + D_i u(P) - S_i q(P) = 0, \text{ for } i = 1, \ldots, N_D.$$

With the same assumptions for the exterior field, this becomes a block diagonal matrix equation

$$\left(\frac{1}{2}I + \mathcal{D}_{\text{int}}\right)\mathbf{u} - \mathcal{S}_{\text{int}}\mathbf{q} = 0 \tag{6.11}$$

where

$$\mathcal{D}_{\text{int}}(a,b) = \begin{cases} D_a\phi_{am}(y_{an}) & \text{if } a = b \\ 0 & \text{if } a \neq b \end{cases}$$

$$\mathcal{S}_{\text{int}}(a,b) = \begin{cases} S_a\phi_{am}(y_{an}) & \text{if } a = b \\ 0 & \text{if } a \neq b \end{cases}$$

and $a, b = 1, \ldots, \mathrm{N_D}$ and $m, n = 1, \ldots, \mathrm{DOF}$. Note that these integrations are also singular and the operator splitting techniques mentioned above should be applied.

6.3.3 Interface

For the exterior field we have a matrix equation for u_{ext} and for the interior field we have a matrix equation for $u^i, i = 1, \ldots, N_D$, we need to combine the two by the interface conditions. For u_{inc} and u_{sc} defined by (6.9), note that since we assume u_{inc} satisfies Helmholtz equation outside of Ω_i, (6.10) is also valid for u_{sc}. That is,

$$\left(\frac{1}{2}I - \mathcal{D}_{\text{ext}}\right)\mathbf{u}_{\text{sc}} + \mathcal{S}_{\text{ext}}\mathbf{q}_{\text{sc}} = 0. \tag{6.12}$$

Next, from the interface conditions, we see for $i = 1, \ldots, N_D$

$$u^i = u_{\text{inc}} + u_{\text{sc}} \text{ on } \Gamma_i.$$

Using this, we may rewrite (6.11) in terms of u_{sc} and the known field u_{inc}. That is,

$$\left(\frac{1}{2}I + \mathcal{D}_{\text{int}}\right)\mathbf{u}_{\text{sc}} - \mathcal{S}_{\text{int}}\mathbf{q}_{\text{sc}} = -\left(\frac{1}{2}I + \mathcal{D}_{\text{int}}\right)\mathbf{u}_{\text{inc}} + \mathcal{S}_{\text{int}}\mathbf{q}_{\text{inc}}. \tag{6.13}$$

Combining (6.12) and (6.13), we have an equation that we may solve for the scattered field

$$\begin{bmatrix} \left(\frac{1}{2}I - \mathcal{D}_{\text{ext}}\right) & \mathcal{S}_{\text{ext}} \\ \\ \left(\frac{1}{2}I + \mathcal{D}_{\text{int}}\right) & -\mathcal{S}_{\text{int}} \end{bmatrix} \begin{bmatrix} \mathbf{u}_{\text{sc}} \\ \\ \mathbf{q}_{\text{sc}} \end{bmatrix} = \begin{bmatrix} 0 \\ \\ -\left(\frac{1}{2}I + \mathcal{D}_{\text{int}}\right)\mathbf{u}_{\text{inc}} + \mathcal{S}_{\text{int}}\mathbf{q}_{\text{inc}} \end{bmatrix} \tag{6.14}$$

The matrix of this linear system is full and non-symmetric. One may use a direct or iterative solver to solve this system. When solving for a large number of unknowns it is advised to use an iterative solver because of the speed. Upon solving, and finding $\mathbf{u}_{\text{sc}}$ and $\mathbf{q}_{\text{sc}}$ one may use the integral equations derived for the exterior and interior to find the value of the total wave everywhere.

6.4 Numerical Examples

We wish to test our methods for photonic crystal lattices, with and without defects. First we must test the accuracy of our proposed method to solve Helmholtz equation.

Example 6.4.1. Let Ω be the circle of radius $r_0 = \frac{1}{2}$ μm centered at the origin. Dielectric permittivities are $\varepsilon = 4$ inside the circle and $\varepsilon = 1$ outside the circle. Suppose we have an incident wave $u_{\text{inc}}(x) = e^{i(2\pi x)}$. We want to find $u_{\text{ext}} = u_{\text{inc}} + u_{\text{sc}}$ of (6.9) and u_{int} by solving the following scattering problem

$$\begin{aligned} \Delta u_{\text{ext}} + (2\pi)^2 u_{\text{ext}} &= 0 && \text{outside } \Omega, \\ \Delta u_{\text{int}} + 4(2\pi)^2 u_{\text{int}} &= 0 && \text{inside } \Omega, \\ u_{\text{ext}} &= u_{\text{int}} && \text{on } \Gamma, \\ \frac{\partial u_{\text{ext}}}{\partial n} &= \frac{\partial u_{\text{int}}}{\partial n} && \text{on } \Gamma, \\ \lim_{r\to\infty} \sqrt{u_{\text{sc}}}\left(\frac{\partial u_{\text{sc}}}{\partial n} - iku_{\text{sc}}\right) &= 0. \end{aligned}$$

This represents the scattering of a plane wave by a photonic crystal made up of a single rod. We test our method on this problem using $N = 4, 8, 16, 32$ particle shape functions.

An analytic solution exists for the TM mode from ([9, 10]), we compare our approximate solution with this true solution.

$$E_z(r,\theta) = e^{i\omega}\sum_{n=-\infty}^{+\infty} C_n^{tot} J_n(k_{\text{int}} r)e^{in\theta} \text{ where } r \le r_0,$$

$$E_z(r,\theta) = e^{i\omega}\sum_{n=-\infty}^{+\infty} \left(i^{-n}J_n(k_{\text{ext}} r) + C_n^{scat} H_n^{(2)}(k_{\text{ext}} r)\right) e^{in\theta} \text{ where } r > r_0,$$

and the coefficients are defined as

$$C_n^{tot} = i^{-n}\frac{\frac{k_{\text{ext}}}{\mu_{\text{ext}}} J_n'(k_{\text{ext}} r_0)H_n^{(2)}(k_{\text{ext}} r_0) - \frac{k_{\text{ext}}}{\mu_{\text{ext}}} H_n'^{(2)}(k_{\text{ext}} r_0)J_n(k_{\text{ext}} r_0)}{\frac{k_{\text{int}}}{\mu_{\text{int}}} J_n'(k_{\text{int}} r_0)H_n^{(2)}(k_{\text{ext}} r_0) - \frac{k_{\text{ext}}}{\mu_{\text{ext}}} H_n'^{(2)}(k_{\text{ext}} r_0)J_n(k_{\text{int}} r_0)},$$

and

$$C_n^{scat} = i^{-n}\frac{\frac{k_{\text{ext}}}{\mu_{\text{ext}}} J_n'(k_{\text{ext}} r_0)J_n(k_{\text{int}} r_0) - \frac{k_{\text{int}}}{\mu_{\text{int}}} J_n'(k_{\text{int}} r_0)J_n(k_{\text{ext}} r_0)}{\frac{k_{\text{int}}}{\mu_{\text{int}}} J_n'(k_{\text{int}} r_0)H_n^{(2)}(k_{\text{ext}} r_0) - \frac{k_{\text{ext}}}{\mu_{\text{ext}}} H_n'^{(2)}(k_{\text{ext}} r_0)J_n(k_{\text{int}} r_0)},$$

where (r,θ) are the polar coordinates centered at the origin and r_0 is the radius of the cylinder. We will now compare our method to this exact solution.

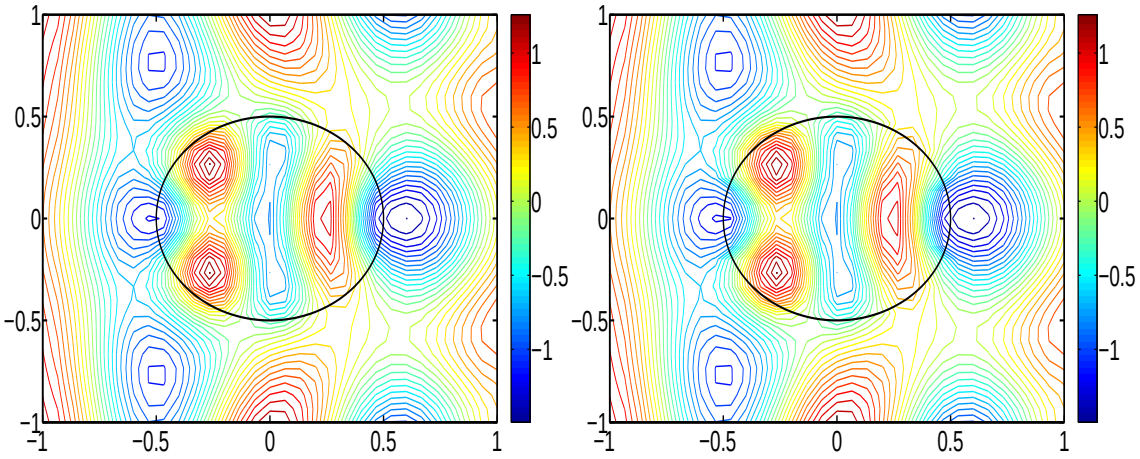

(a) Exact solution (b) N=32

Figure 6.2: Contour plot of E_z in computational domain [-1 μm,1 μm] $\times$ [-1 μm,1 μm] for a cylinder with r=0.5 μm with $k = 2\pi$ and $\varepsilon = 4$.

From Figures 6.2 and 6.3, we see that our numerical solution converges to the true solution. We also note that compared to ([10]), to obtain an accurate numerical

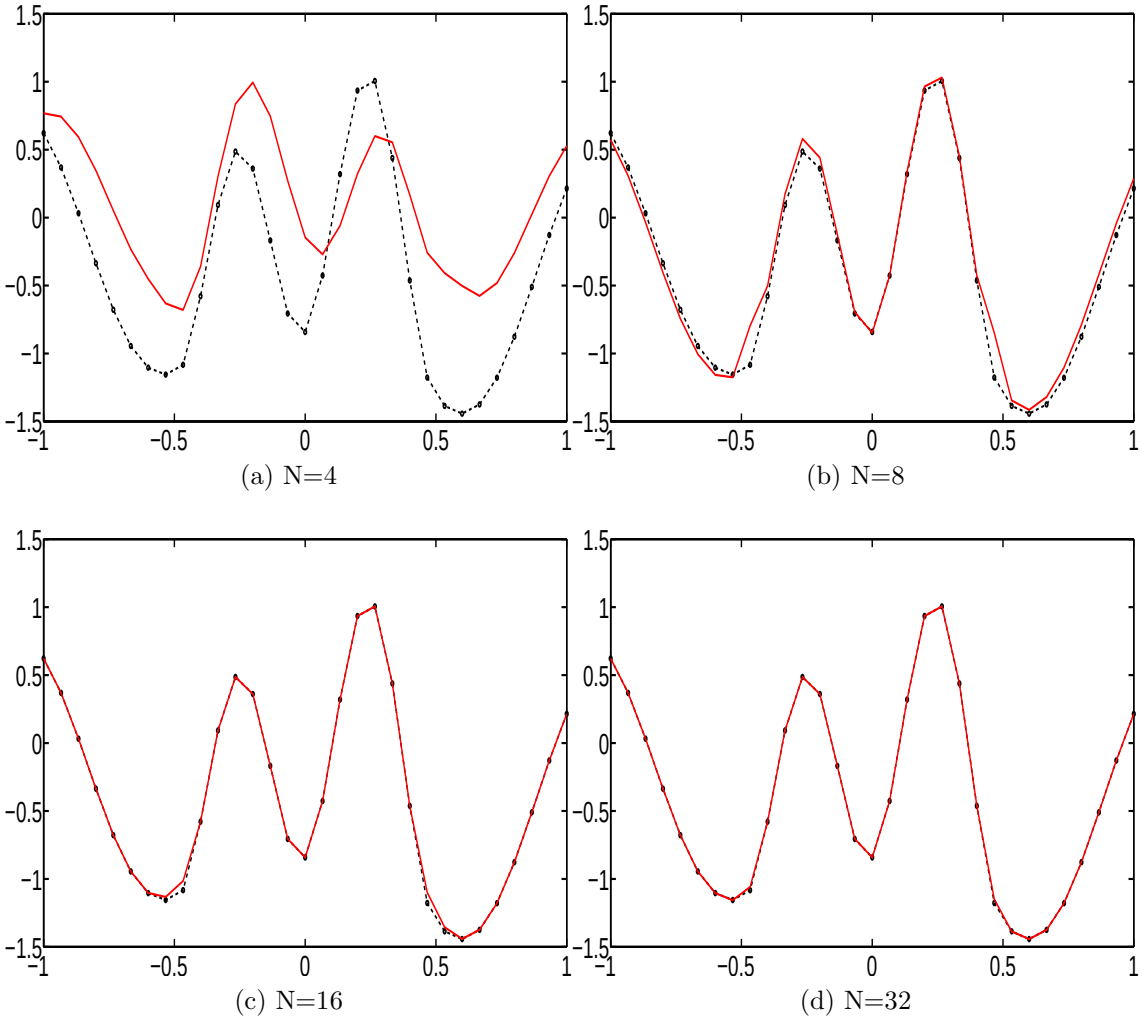

(a) N=4 (b) N=8

(c) N=16 (d) N=32

Figure 6.3: Plot of E_z along x-axis from [-1 μm, 1 μm] for a cylinder with r=0.5 μm with $k = 2\pi$ and $\varepsilon = 4$. True solution is dashed line and the approximate solution is solid. N is the number of shape functions used to approximate the solution.

solution, we require less degrees of freedom. From the figures, it appears that using $N = 32$ with this method out performs using 80 quadrature points with the Nyström method.

Next, we will test the accuracy of these meshless shape functions on polygonal domains. First, we wish to check the accuracy of this method applied to Helmholtz equation when the true solution is a polynomial solution. We do this by solving the inhomogeneous Helmholtz equation with Dirichlet boundary conditions.

$$\Delta u(x) + k^2 u(x) = f(x) \quad \text{in} \quad \Omega \tag{6.15}$$

$$u(x) = g(x) \quad \text{on } \Gamma. \tag{6.16}$$

To solve the inhomogeneous Helmholtz equation using BEM, one must use a different BIE. This comes from the fact that we have a nonzero load function. The BIE corresponding to the inhomogeneous Helmholtz equation is

$$c(P)u(P) = \int_\Omega f(x)G_k(x,P)dx + \int_\Gamma \frac{\partial u(x)}{\partial n} G_k(x,P)ds(x) - \int_\Gamma \frac{\partial G_k(x,P)}{\partial n} u(x)ds(x).$$

One may notice, this BIE contains a weakly singular domain integral. To approximate the domain integral, we used the Duffy transform with logarithmic Gaussian quadrature.

Example 6.4.2. Consider the inhomogeneous Helmholtz equation (6.15) in $\Omega = [0,1]^2$ with $k = 2$ whose true solution is $u(x) = z^4$ where $z = x + iy$. We solve this problem by using the collocation method with use of particle shape functions with RPP order 2, 3, and 4 respectively.

Table 6.1: Errors in maximum norm of the real parts of q and u on Γ and error in maximum norm of the real part of u in Ω for RPP orders $2, 3$, and 4 for Example 6.4.2.

p	DOF	$\|u - \tilde{u}\|_{\infty,\Gamma}$	$\|q - \tilde{q}\|_{\infty,\Gamma}$	$\|u - \tilde{u}\|_{\infty,\Omega}$
2	24	1.941E-02	3.535E-02	4.726E-03
3	32	1.792E-03	3.546E-03	4.883E-04
4	40	5.329E-15	1.643E-13	2.072E-13

The true solution is a fourth order polynomial. As Table 6.1 shows, RPP order 2 and 3 do not show reasonable results eventhough our method with RPP order 4 almost exactly captures the true solution.

Example 6.4.3. We apply our method to Helmholtz equation when the true solution

is not a polynomial.

$$\Delta u(x) + k^2 u(x) = \quad 0 \qquad \text{in } \Omega = [-0.5, 0.5]^2 \tag{6.17}$$

$$u(x) = \quad g(x) \quad \text{on } \Gamma. \tag{6.18}$$

We let the true solution take the form of a plane wave $u(x) = e^{i(kx)}$ with $k = 2$ and impose the Dirichlet condition everywhere on the boundary. We use two flat-top partition of unity functions on each side of the boundary. We test patch-wise RPBPM with RPP order 2, 4, 6, and 8.

Table 6.2: Errors in maximum norm of the real parts of q and u on Γ and error in maximum norm of the real part of u in Ω for RPP orders $2, 4, 6$, and 8 for Example 6.4.3.

p	DOF	$\|u - \tilde{u}\|_{\infty,\Gamma}$	$\|q - \tilde{q}\|_{\infty,\Gamma}$	$\|u - \tilde{u}\|_{\infty,\Omega}$
2	24	4.265E-03	7.426E-03	1.165E-03
4	40	5.414E-05	2.358E-04	1.017E-05
6	56	3.138E-07	2.057E-06	7.294E-08
8	72	1.050E-09	7.318E-09	2.491E-10

From Table 6.2 we notice as the RPP order increases, so does the accuracy of our solution.

We will look at the use of our method for the simulation of electromagnetic scattering by lattices of photonic crystals.

First, we will consider a square lattice of circular cylinders. We show the contour plots of the full lattice, the lattice with a line defect, and with two point defects. For this lattice, each rod has diameter of 1 μm and is spaced 2 μm in both x and y directions and has permittivity constant $\varepsilon = 9$. The wavelength of the incident wave u_{inc} is $\lambda = 1$ μm and we used $N = 20$ particle shape functions for each rod. From Figure 6.4a, we see for the full lattice, the incoming wave is almost completely blocked from the lattice by the band gap. We also notice for the line defect, we have a good amount of transmission of the wave through the empty row, as shown in Figure 6.4b. For the lattice with two point defects, Figure 6.4c, we see that the wave effectively

gets trapped in the two cavities.

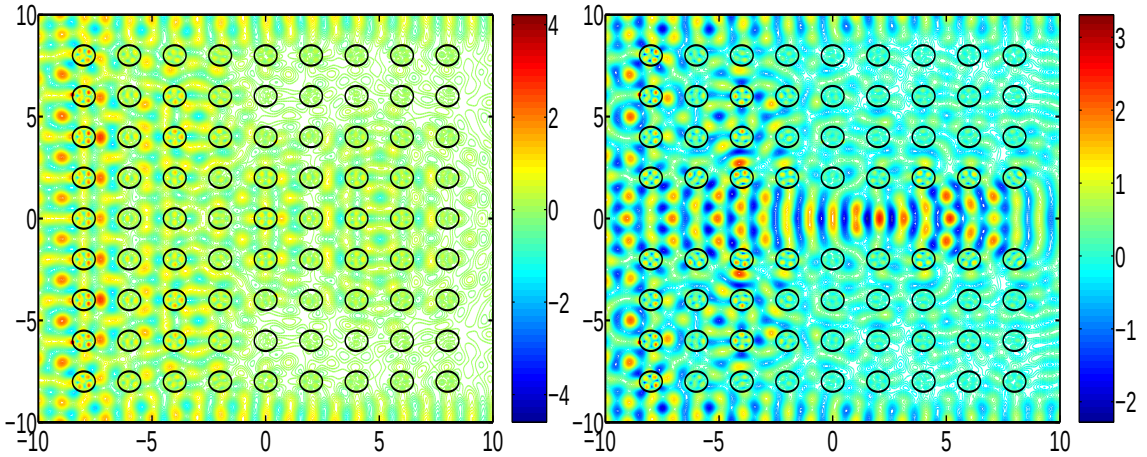

(a) Full lattice (81 rods).

(b) Full lattice with line defect (72 rods).

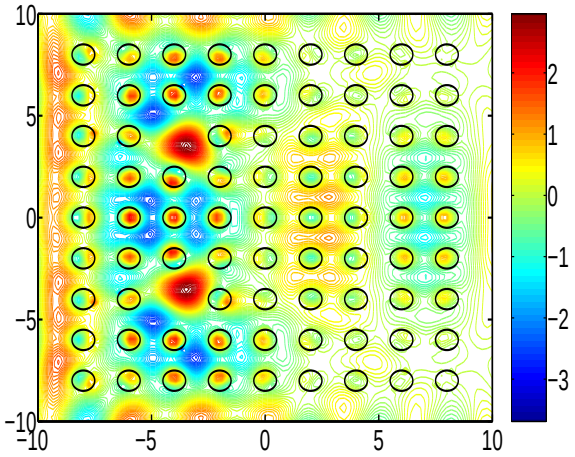

(c) Full lattice with two point defects (79 rods).

Figure 6.4: Square lattice of circular cylinders.

Second, we consider a hexagonal lattice of circular cylinders. We show the contour plots of the full lattice, the lattice with a line defect, and with several point defects mimicing a line defect. For this lattice, each rod has diameter of 1 μm and is spaced 2 μm in both x direction and each row is spaced 2 μm in both x direction and permittivity constant $\varepsilon = 9$. The wavelength of the incident wave u_{inc} is $\lambda = \pi$ μm and we used $N = 20$ particle shape functions for each rod. From Figure 6.5a, we see for the full lattice, the incoming wave is almost completely blocked from the lattice by the band gap. From Figure 6.5b, we also notice for the line defect, we have a good

amount of transmission of the wave through the empty row. Notice for the row of several point defects, the wave is transmitted through the lattice as if there were a damped line defect as seen in Figure 6.5c.

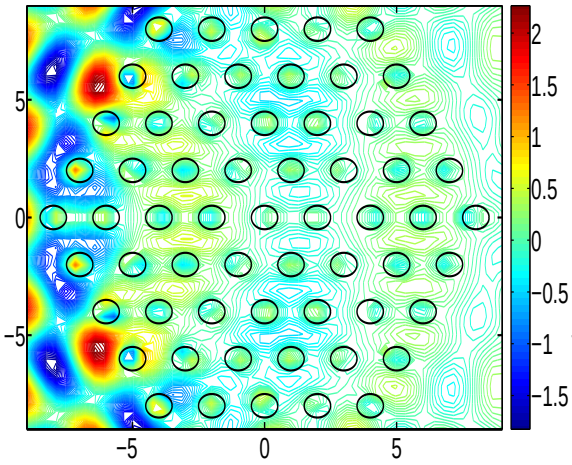

(a) Full lattice (61 rods).

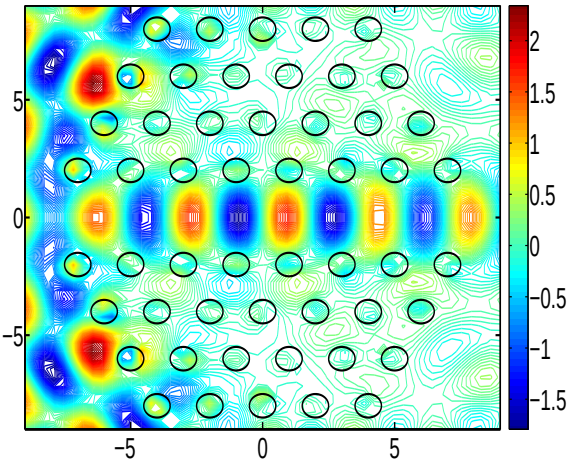

(b) Full lattice with line defect (52 rods).

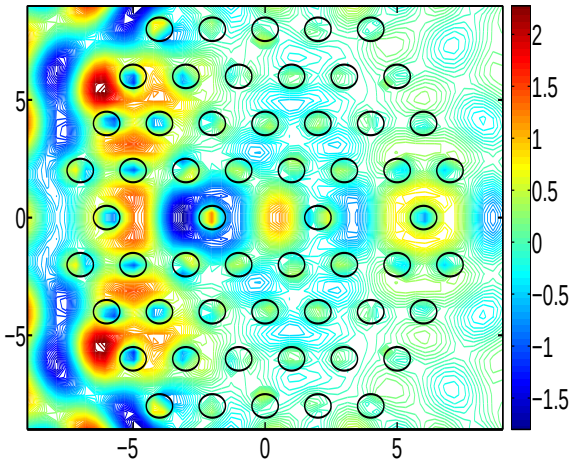

(c) Full lattice with several point defects (56 rods).

Figure 6.5: Hexagonal lattice of circular cylinders.

Finally, we will consider a square lattice of square cylinders. We show the contour plots of the full lattice and the lattice with a line defect. Here, each square has width 1 μm and is spaced 2 μm in both x and y directions from each other. The wavelength of the incident wave u_{inc} is $\lambda = 1$ μm and the permittivity constant $\varepsilon = 9$ and we used DOF $= 24$ basis functions for each square. Due to the lack of analytic solution, we do

not know how accurate these solutions are. We know there are singularities at each corner of the square, thus using RSP shape functions could improve the solution.

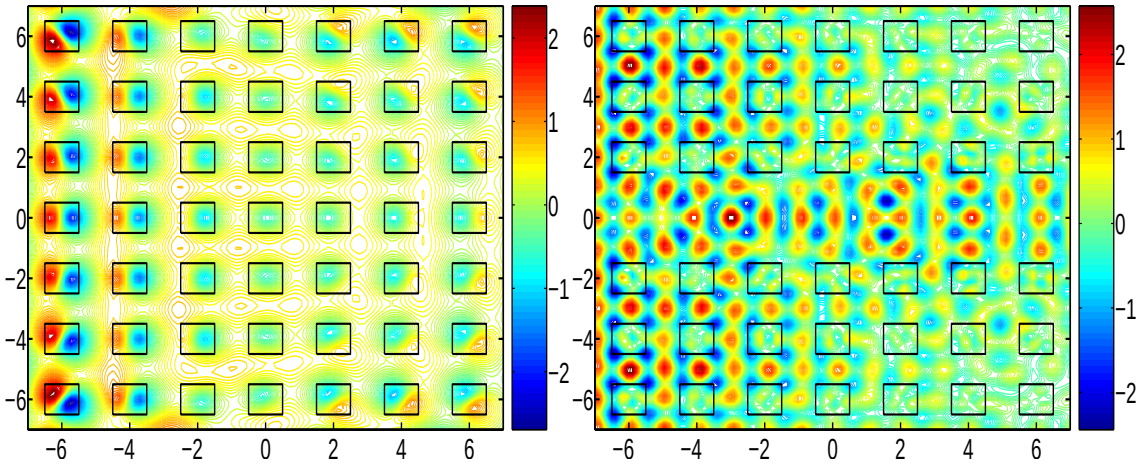

(a) Full lattice (49 rods). (b) Full lattice with line defect (42 rods).

Figure 6.6: Square lattice of square cylinders.

It should be noted, when we wish to evaluate the field at a point near the boundary, the integrals become nearly singular and accuracy at that point will deteriorate, to alleviate that difficulty we place more integration points there or refine the mesh. It is not efficient, but it increases the accuracy. Work is now being done for better ways to handle this difficulty.

CHAPTER 7: MESHLESS METHODS FOR THIN PLATES

7.1 Variational Form of the Classical Plate Theory

In this section, we derive the variational form to be used for the classical plate theory. Let Ω be a bounded domain in $\mathbb{R}^2$ with piecewise smooth boundary, which represents the mid-plane of a plate, which we assume to be of thickness d ($d << diam(\Omega)$)(see, Figure 7.1). We represent the 3-dimensional plate as $\hat{\Omega} = \{(x, y, z) \in \mathbb{R}^3 | (x, y) \in \Omega, |z| < d/2\}$.

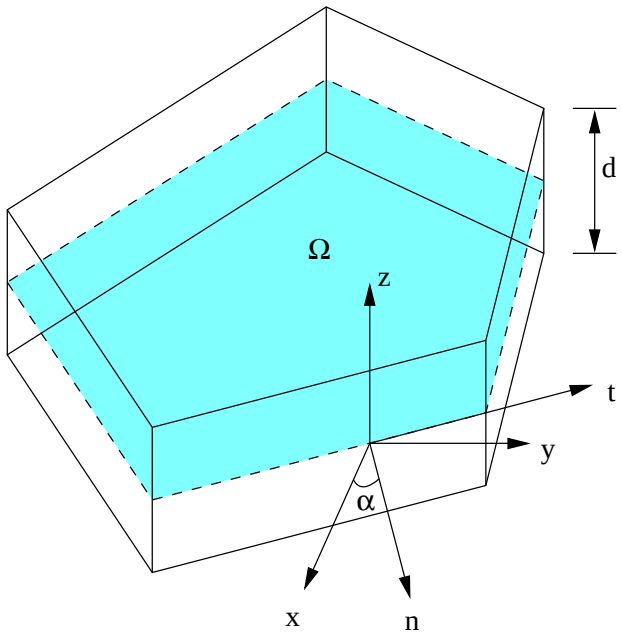

Figure 7.1: 3-dimensional plate $\hat{\Omega}$ and 2-dimensional mid-plane Ω.

The classical (Kirchhoff) plate theory is one in which the displacement field is based on the Kirchhoff hypothesis: (1) Straight lines perpendicular to the middle surface before deformation remain straight after deformation; (2) The transverse normals do not experience elongation (i.e. they are inextensible); (3) The transverse

normals such that they remain perpendicular to the middle surface after deformation ([50],[54],[55]). From this hypothesis, $\epsilon_{zz} = 0$ and the transverse shear strains are zero: $\epsilon_{xz} = \epsilon_{yz} = 0$. Suppose (u, v, w) denote the total displacement of a point along the xyz-coordinate system and (u_0, v_0, w_0) denote the values of u, v and w at the point $(x, y, 0)$. Then these conditions imply

$$u(x,y,z) = u_0 - z\frac{\partial w}{\partial x}, \quad v(x,y,z) = v_0 - z\frac{\partial w}{\partial y}, \quad w(x,y,z) = w_0. \tag{7.1}$$

Substituting the displacement functions of (7.1) into the virtual work formulation, we have ([54],[55])

$$\mathcal{B}(w,v) = \mathcal{F}(v), \text{ for } w, v \in H^2(\Omega), \tag{7.2}$$

where

$$\mathcal{B}(w,v) = D\iint_\Omega \begin{bmatrix} \dfrac{\partial^2 w}{\partial x^2} \\ \dfrac{\partial^2 w}{\partial y^2} \\ \dfrac{\partial^2 w}{\partial x \partial y} \end{bmatrix}^T \begin{bmatrix} 1 & \nu & 0 \\ \nu & 1 & 0 \\ 0 & 0 & 2(1-\nu) \end{bmatrix} \begin{bmatrix} \dfrac{\partial^2 v}{\partial x^2} \\ \dfrac{\partial^2 v}{\partial y^2} \\ \dfrac{\partial^2 v}{\partial x \partial y} \end{bmatrix} dxdy, \tag{7.3}$$

$$\mathcal{F}(v) = \iint_\Omega p(x,y)v dxdy + \int_\Gamma M_n \frac{\partial v}{\partial n} dt - \int_\Gamma \left(Q_n + \frac{\partial M_{nt}}{\partial t}\right) v dt \tag{7.4}$$

where ν and E are the Poisson's ratio and the Young's modulus of an isotropic elastic material, respectively, and

$$\begin{aligned}
D &= \frac{Ed^3}{12(1-\nu^2)}, p = \frac{\partial Q_x}{\partial x} + \frac{\partial Q_y}{\partial y}, \\
M_x &= D\left(\frac{\partial^2 w}{\partial x^2} + \nu\frac{\partial^2 w}{\partial y^2}\right), M_y = D\left(\nu\frac{\partial^2 w}{\partial x^2} + \frac{\partial^2 w}{\partial y^2}\right), \\
M_{xy} &= D(1-\nu)\frac{\partial^2 w}{\partial x \partial y} = -M_{yx}, \\
Q_x &= D\left(\frac{\partial^3 w}{\partial x^3} + \frac{\partial^3 w}{\partial x \partial y^2}\right), Q_y = D\left(\frac{\partial^3 w}{\partial y^3} + \frac{\partial^3 w}{\partial x^2 \partial y}\right), Q_n = Q_x \cos\alpha + Q_y \sin\alpha, \\
M_n &= [M_x, M_y, M_{xy} - M_{yx}][\cos^2\alpha, \sin^2\alpha, \sin\alpha\cos\alpha]^T, \\
M_{nt} &= [-M_x + M_y, M_{xy}][\sin\alpha\cos\alpha, (\cos^2\alpha - \sin^2\alpha)]^T.
\end{aligned}$$

Here α is the angle between the x-axis and the normal axis of the normal-tangential coordinate system as shown in Figure 7.1. The conventional boundary conditions in

Table 7.1: Boundary conditions in classical plate theory.

Type of support	Essential (Geometric) B.C.	Natural (Force) B.C.
clamped	$w = 0, \quad \partial w/\partial n = 0$	None
simple Support	$w = 0$	$M_n = 0$
free	None	$M_n = M_{nt} = Q_n = 0$
symmetry	$\partial w/\partial n = 0$	$Q_n + \partial M_{nt}/\partial t = 0$
antisymmetry	$w = 0$	$M_n = 0$

the classical theory of plate are listed in Table 7.1.

Let $\mathcal{V}^{RPP}$ be an approximation space constructed by use of the generalized partition of unity functions Ψ_l^P and the reference shape functions $\hat{\phi}_k$ to be constructed in the next section. That is,

$$\mathcal{V}^{RPP} = \text{span}\{\Psi_l^P \cdot [\hat{\phi}_k \circ T_l^{-1}] : l = 1, 2, \ldots, N; k = 1, 2, \ldots, N_l\}, \tag{7.5}$$

where Ω is partitioned into the N numbers of patches $Q_1, \ldots, Q_N$ and T_l is the patch mapping from a reference patch into ω_l^δ, the support of the generalized product PU function Ψ_l^P, which is associated with the physical patch Q_l. The approximation space $\mathcal{V}^{RPP}$ has the following properties: (1) high regularity of each member; (2) the Kronecker delta property at almost all particles; (3) reproducing polynomial property of high order on the patches with no intersections with clamped boundaries.

The proposed meshfree particle method for the plate problems is the Galerkin method with use of $\mathcal{V}^{RPP}$ as follows: Find $w \in \mathcal{V}^{RPP}$ such that

$$\mathcal{B}(w, v) = \mathcal{F}(v), \text{ for all } v \in \mathcal{V}^{RPP}. \tag{7.6}$$

7.2 Particle Shape Functions with Kronecker Delta Property to Deal With Essential Boundary Conditions

It is necessary to construct different shape functions for different boundary conditions, as can be noted from the table above. In this section, we will construct shape functions to deal with simply supported and clamped boundary conditions. Let $\hat{T}$ and $\hat{R}$, respectively, denote the reference triangle with vertices $(0, 0), (1, 0), (0, 1)$, and

the reference rectangle $[0,1] \times [0,1]$.

7.2.1 Shape Functions for Imposing Simply Supported Boundary Conditions

Without loss of generality, we consider the construction of patch-wise smooth RPP shape functions with compact support that have the polynomial reproducing order 3. Higher orders can be constructed similarly.

The barycentric coordinates of $\hat{T}$ are $L_1(\xi,\eta) = 1-\xi-\eta$; $L_2(\xi,\eta) = \xi$; and $L_3(\xi,\eta) = \eta$. The following ten functions are the Lagrange interpolation shape functions of RPP order 3 that correspond to three vertices, six lateral nodes, and one interior node, respectively:

$$\hat{\phi}_1 = L_1(3L_1-1)(3L_1-2)/2; \hat{\phi}_2 = L_2(3L_2-1)(3L_2-2)/2;$$

$$\hat{\phi}_3 = L_3(3L_3-1)(3L_3-2)/2; \hat{\phi}_4 = (9/2)L_1L_2(3L_1-1);$$

$$\hat{\phi}_5 = (9/2)L_1L_3(3L_1-1); \hat{\phi}_6 = (9/2)L_2L_1(3L_2-1); \hat{\phi}_7 = (9/2)L_2L_3(3L_2-1);$$

$$\hat{\phi}_8 = (9/2)L_3L_1(3L_3-1); \hat{\phi}_9 = (9/2)L_3L_2(3L_3-1); \hat{\phi}_{10} = 27L_1L_2L_3. \tag{7.7}$$

In what follows, the k-th Lagrange interpolating polynomial of degree $n-1$ associated with n-distinct nodes $\xi_1,\ldots,\xi_n$ is denoted by $L_{n,k}(\xi) = \prod_{i=1,i\neq k}^{n} \frac{\xi-\xi_i}{\xi_k-\xi_i}$. Let $L_{4,j}(\xi), j = 1,2,3,4$, be the Lagrange interpolation polynomials of order 3 corresponding to nodes $0, 1/3, 2/3, 1$, respectively. On $\hat{R}$ we have 16 RPP shape functions of order 3:

$$\hat{\phi}_k(\xi,\eta) = L_{4,i}(\xi)\cdot L_{4,j}(\eta), k = 4(i-1)+j, 1 \leq i,j \leq 4, \tag{7.8}$$

The RPP shape functions defined by (7.7) and (7.8) can now be mapped to the physical domain Ω to make smooth local approximation functions on triangular or quadrangular patches in Ω. For example, let $T_l : \hat{R} \to Q_l$ be a smooth patch mapping and $\Psi_l^P(x,y)$ be the generalized product PU corresponding to Q_l. Then

$$\Psi_l^P(x,y)\cdot\hat{\phi}_k(T_l^{-1}(x,y)), \quad k = 1,\ldots,16$$

are smooth functions with compact support $\omega_l = \text{supp}(\Psi_l^P) \supseteq Q_l$. To handle the simple support boundary condition, shape functions that are not 0 on $\partial\Omega$ are discarded

and not used in the approximation space $\mathcal{V}^{RPP}$. All functions in $\mathcal{V}^{RPP}$ satisfy this boundary condition.

7.2.2 Shape Functions for Imposing Clamped Boundary Conditions

We will present the construction of shape functions on $\hat{R}$. We now consider a n^{th} order modified Lagrange polynomial $M_{n+1,k}(\xi) = \xi L_{n+1,k}(\xi), k = 1, \ldots, n+1$ on $[0, 1]$. Here, we notice that $M_{n+1,k}(0) = 0$ for $k = 1, \ldots, n+1$ and $M'_{n+1,k}(0) = 0$ for $k = 2, \ldots, n+1$. Now, the reference shape functions are

$$^1\hat{\phi}_k(\xi, \eta) = M_{n+1,i}(\xi) L_{n+1,j}(\eta)$$

for quadrangular patches with one clamped side where $k = (n+1)(i-1) + j$, $i = 2, \ldots, n+1$, and $j = 1, \ldots, n+1$ and

$$^2\hat{\phi}_k(\xi, \eta) = M_{n+1,i}(\xi) M_{n+1,j}(\eta)$$

for quadrangular patches with two clamped sides where $k = (n+1)(i-1) + j$, $i = 2, \ldots, n+1$, and $j = 2, \ldots, n+1$.

For example, let $T_l : \hat{R} \to Q_l$ be a smooth patch mapping from the reference square to a quadrangular patch with one clamped side such that T_l maps $\xi = 0$ to the clamped side of Q_l. Here we will use the order 3 reference shape functions $^1\hat{\phi}_k(\xi, \eta)$ where $k = 1, \ldots, 12$. Let $\Psi^P_l(x, y)$ be the $\mathcal{C}^1$-generalized product PU corresponding to Q_l.

$$\Psi^P_l(x, y) \cdot^1 \hat{\phi}_k(T_l^{-1}(x, y)), \quad k = 1, \ldots, 12$$

are $\mathcal{C}^1$-functions with compact support $\omega_l = \text{supp}(\Psi^P_l) \supseteq Q_l$. In order to satisfy the clamped boundary condition, shape functions are not 0 on $\partial\Omega$ are excluded from the approximation space $\mathcal{V}^{RPP}$, so that all functions in $\mathcal{V}^{RPP}$ satisfy the clamped boundary condition.

For $\hat{T}$, shape functions are constructed similarly by modifying the Lagrange interpolation polynomials by multiplying by ξ. However, special care must be taken so that the triangular patch only has one boundary intersecting with $\partial\Omega$.

7.3 Numerical Examples

Here, we use $\phi^R_{g2}(\frac{x+\delta}{2\delta})$ in Eqn.(2.12) with $\delta = 0.05$ for the construction of generalized product PU functions whose first order derivatives are continuous.

Example 7.3.1. With material constants $\nu = 0.3$, $E = 10^9$ N/m^2, $a = 0.6m$, $d = 0.001m$, $p = 100.0$N (These material constants are the same as those in [27]). We test the proposed meshfree particle methods to the following cases:

A: Clamped rectangular plate with point load at the center(Table 7.2)

B: Clamped rectangular plate with uniform load(Table 7.3)

C: Simply supported rectangular plate with point load at the center(Table 7.4)

D: Simply supported rectangular plate with uniform load(Table 7.5)

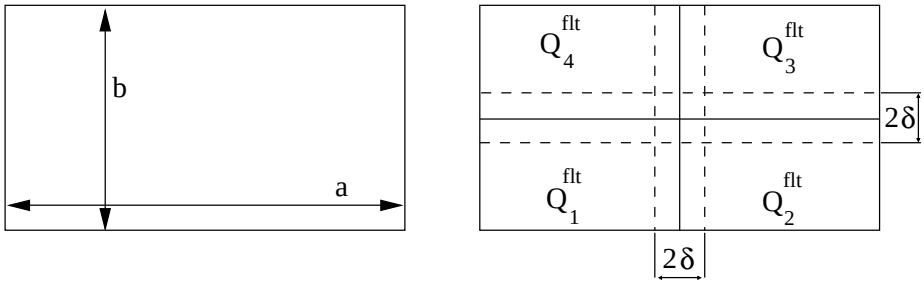

Figure 7.2: Rectangular plate and partition into four patches. Q_j^{flt} is the flat-top part of supp(Φ_j^P). Here, $\delta = 0.05$.

In Tables 7.2,7.3,7.4, and 7.5,

- $\beta = \dfrac{\omega_{\max} D}{Pa^2}$, where P is load, w_{max} is the vertical displacement at the center point, a and b are the two side lengths of a rectangular plate shown Figure 7.2.
- the results in the rows "$\beta_{\text{RPP }4}$" and "$\beta_{\text{RPP }6}$" are those obtained by our method with use of particle shape functions of RPP order 4 and RPP order 6, respectively. The results in the row "β_{Liu}" are those in ([28],[27]) and the results in the row "$\beta_{\text{Timoshenko}}$" are the analytic solutions in ([56]).

From these tests, we observe the following

1. Tables 7.2 and 7.4 show that even though our method use much smaller number of particles (144 in $\beta_{\text{RPP }6}$ and 256 in β_{Liu}), our method yields better results than

the moving least squares (MLS) method employed in ([28]). Actually, the results in the row "$\beta_{\text{RPP }4}$" that use 36 particles are similar to those number in "β_{Liu}" that use $256(16 \times 16)$ uniformly spaced particles.

2. Implementing RPP shape functions satisfying clamped BC and constructing generalized product PU functions for the proposed meshfree particle method is simple.
3. Tables 7.3 and 7.5 show that in the case of uniform load, the results in the row "$\beta_{\text{RPP }4}$" show that our method using 36 particles for clamped BC (64 particles for simply supported BC) yields already enough accuracy.
4. The numerical solutions for the plate with uniform load is slightly better than those for the plate with point load. That is because analytic solutions of plates with point load have a mild singularity (of type $r^2 \log r$) at the center point.

Table 7.2: Values of β for various ratios of b/a corresponding to a point load of P at the origin for a clamped plate.

b/a	DOF	1.0	1.2	1.4	1.6	1.8	2.0
$\beta_{\text{RPP 4}}$	36	0.00553	0.00637	0.00679	0.00696	0.00700	0.00697
$\beta_{\text{RPP 6}}$	100	0.00559	0.00645	0.00689	0.00709	0.00716	0.00719
β_{Liu}	256	0.00552	0.00637	0.00680	0.00698	0.00703	0.00704
$\beta_{\text{Timoshenko}}$	∞	0.00560	0.00647	0.00691	0.00712	0.00720	0.00722

Table 7.3: Values of β for different ratios of b/a corresponding to a uniform load of P for a clamped plate.

b/a	DOF	1.0	1.2	1.4	1.6	1.8	2.0
$\beta_{\text{RPP 4}}$	36	0.00126	0.00172	0.00205	0.00227	0.00240	0.00247
$\beta_{\text{RPP 6}}$	100	0.00127	0.00172	0.00207	0.00230	0.00245	0.00253
$\beta_{\text{Timoshenko}}$	∞	0.00126	0.00172	0.00207	0.00230	0.00245	0.00254

Table 7.4: Values of β for different ratios of b/a corresponding to a point load of P at the origin for a simply supported plate.

b/a	DOF	1.0	1.2	1.4	1.6	1.8	2.0
$\beta_{\text{RPP 4}}$	64	0.01154	0.01348	0.01478	0.01559	0.01607	0.01633
$\beta_{\text{RPP 6}}$	144	0.01157	0.01353	0.01483	0.01567	0.01618	0.01648
β_{Liu}	256	0.01157	0.01344	0.01476	0.01556	0.01603	0.01632
$\beta_{\text{Timoshenko}}$	∞	0.01160	0.01353	0.01484	0.01570	0.01620	0.01651

Table 7.5: Values of β for different ratios of b/a corresponding to a uniform load of P for a simply supported plate.

b/a	DOF	1.0	1.2	1.4	1.6	1.8	2.0
$\beta_{\text{RPP 4}}$	64	0.00406	0.00565	0.00708	0.00830	0.00930	0.01010
$\beta_{\text{RPP 6}}$	144	0.00406	0.00565	0.00708	0.00831	0.00932	0.01013
$\beta_{\text{Timoshenko}}$	∞	0.00406	0.00564	0.00705	0.00830	0.00931	0.01013

CHAPTER 8: CONCLUSIONS

For numerical solutions of BIEs, three meshless BEMs were introduced: meshfree reproducing polynomial boundary particle method (RPBPM), patch-wise reproducing polynomial boundary particle method, and patch-wise reproducing singularity boundary particle method(RSBPM). The first two methods are for BIEs without singularities and the third is for BIEs with singularities.

We tested all of these methods with the Laplace equation in two dimensions. Even though the domain for each test problem is a square, these methods will work in the same way for a general polygonal domain. Through a numerical example, we noted that the collocation method is more practical than the Galerkin method for patch-wise RPBPM.

We extended patch-wise RPBPM and RSPBM to the three dimensional Laplace equation with and without singularities. Our results show that patch-wise RSBPM is one of the most effective methods to deal with three dimensional singularity problems.

Patch-wise RSBPM is virtually the one-dimensional counterpart of the Method of Auxiliary Method(MAM) in p-FEM. It has been proven that the p-FEM together with MAM is effective in dealing with singularity problems. However, MAM fails when it is coupled with h-FEM in which piecewise linear approximation functions are employed. Similarly, the reproducing singularity boundary particle method is more effective when the mapping technique is coupled with RPP shape functions with high reproducing order.

We tested patch-wise RPBPM on the Helmholtz equation and obtained similar results as that of the Laplace equation. Using the trapezoidal rule and different shape functions, we extended our method to circular domains. We noticed that

using the collocation method with particle shape functions for circular domains gives an accurate approximate solution to Helmholtz equation with less degrees of freedom than the Nyström method.We also have seen that our method works well for modeling wave propagation through photonic crystals.

For thin plate problems, the shape functions constructed to satisfy the simply supported and clamped boundary conditions respectively, were introduced. The use of these combined with the generalized product PU function and RPP shape functions yields promising results as demonstrated in chapter 7.

In closing, meshfree particle methods are a powerful tool in the numerical solution of PDE.

For other PDEs such as the elasticity equations and the biharmonic equation, the fundamental solutions are known and hence our methods are applicable to several areas of science and engineering. In the future, patch-wise RPBPM and RSBPM will be applied to solve practical science and engineering problems. Extension of these methods to general curved domains is also planed.

REFERENCES

[1] M. Arad, Z. Yosibash, G. Ben-Dor, and A. Yakhot: *Computing Flux Intensity Factors by a Boundary Method for elliptic equations with singularities,* Commum. Numer. Meth. Engng. 14 (1998) 657-670.

[2] K. Atkinson, The Numerical Solution of Integral Equations of the Second Kind, Cambridge University Press 1997.

[3] S. Atluri and Shen, S.: The Meshless Method, Tech Science Press, 2002.

[4] I. Babuška, U. Banerjee, J.E. Osborn: *Survey of meshless and generalized finite element methods:A unified approach,* Acta Numerica, Cambridge Press (2003) 1-125.

[5] I. Babuška, Banerjee, U., Osborn, J.E.: *Meshless and generalized finite element methods: Survey of some Major Results,* Meshfree Methods For Partial Differential Equations, Lecture notes in Computational Science and Engineering 26, Springer, 2003.

[6] I. Babuška, Banerjee, U., Osborn, J.E.: *On the approximability and the selection of particle shape functions,* Numer. math. 96 (2004) 601-640.

[7] Belytschko, T., D. Organ, Y. Krongauz: *A coupled finite element-element-free Galerkin method*, Comput. Mech. 17 (3) (1995) 186-195.

[8] S. Brenner, R. Scott: The mathematical thoery of finite element methods, Springer,1994.

[9] W. Cai and S. Deng,*An upwinding embedded boundary method for Maxwell's equations in media with material interfaces: 2D case* J. Comp. Phys. 190, 159 (2003).

[10] M.H. Cho, Y.P. Lee, W. Cai *Modeling of 2D Photonic Crystals with a Boundary Integral Equation*,J. Korean Phys. Soc. 51, 1507-1512 (2007).

[11] P.G. Ciarlet : *The Finite Element Method for Elliptic Problems,* North-Holland, 1978.

[12] C. Davis, J.G. Kim, H.S. Oh, M.H. Cho,*Meshfree Particle Methods in the frame work of Boundary Element Methods for Helmholtz Equation*, to appear.

[13] C. A. Duarte, J. T. Oden: *An hp adaptive method using clouds,* Computer methods in App. Mech. Engrg, Vol. 139 (1996) 237-262.

[14] M. G. Duffy: *Quadrature Over a Pyramid or Cube of Integrands with a Singularity at a Vertex* , SIAM J. Numer. Anal. 19, (1982) 1260-1262.

[15] M. Griebel, M.A. Schweitzer: *A particle-Partition of Unity Methods Part VII: Adaptivity,* Meshfree Methods for partial Differential Equations III, Lect. Notes in Compu. Science and Engr. 57, Springer 2007.

[16] W. Han, X. Meng:*Error analysis of reproducing kernel particle method*, Comput. Meth. Appl. Mech. Engrg. 190 (2001) 6157-6181.

[17] P. Hunter and A. Pullan, FEM and BEM Notes, Dept. of Eng Science, Univ. of Auckland, (2001).

[18] J. D. Joannopoulos, S. G. Johnson, J. N. Winn, and R. D. Meade, Photonic Crystals: Molding the Flow of Light. Second Edition. (Princeton University Press, Princeton, 2008).

[19] R. Kress, Linear Integral Equations, Springer-Verlag, 1989.

[20] C. Lacour:*Non-conforming domain decomposition method for plate and shell problems,* Tenth International Conference on Domain Decomposition Methods, AMS Contemporary Mathematics 218 (1998) 304-310.

[21] P. Lascaux, P. Lesaint: *Some nonconfroming finite element for the plate bending problem,* Rev. Francaise Automat. Informat. Recherche Operationnelle Ser. Rouge Anal, Numer., 9(R-1) (1975) 9-53.

[22] S. Li, W. K. Liu : Meshfree Particle Methods, Springer-Verlag 2004.

[23] S. Li, W. K. Liu: *Reproducing Kernel hierarchical partition of unity, Part I: Formulations,* International Journal for Numerical Methods in Engineering, Vol. 45, (1999) 251-288.

[24] S. Li, Lu, H., Han, W., Liu, W.K., and Simkins, D.C.Jr. :*Reproducing Kernel Element Method: Part II. Globally Conforming I^m/C^n hierarchies,* Computer Methods in App. Mech. and Engrg, Vol. 193 (2004) 953-987.

[25] X. Li and J. Zhu :*A Galerkin boundary node method and its convergence analysis,* J. Compu. and Appl. Math. 230 (2009) 314-328.

[26] Z-C. Li, R. Mathon and P. Sermer, *Boundary methods for solving elliptic problems with singularities and interfaces*, SIAM J. Numer. Anal., 24(3), 487-498 (1987).

[27] G. R. Liu, X. L. Chen :*A meshfree method for static and free vibration analysises of thin plates of complicated shape,* J. Sound and Vibration, 241(5), (2001) 839-853.

[28] G. R. Liu, Mehsfree Methods, second edition, CRC Press, 2010.

[29] W.K. Liu, Jun, S., and Zhang, Y. F.: *Reproducing Kernel Particle Methods*, International Journal for Numerical Methods in Fluids, vol. 20, (1995) 1081-1106.

[30] W.K. Liu, Liu, S. Jun, S. Li, Adee, J. and Belytschko, T.: *Reproducing Kernel Particle Methods for Structural Dynamics,* International Journal for Numerical Methods in Engineering, vol. 38, (1995) 1655-1679.

[31] W.K. Liu, Li, S. and Belytschko, T.: *Moving Least Square Reproducing Kernel Method Part I: Methodology and Convergence,* Computer Methods in Applied Mechanics and Engineering, Vol. 143, (1997) 422-453.

[32] W.K. Liu, Han, W., Lu, H., Li, S., and Cao, J. :*Reproducing Kernel Element Method: Part I. Theoretical formulation,* Computer Methods in App. Mech. and Engrg, Vol. 193 (2004) 933-951.

[33] T. R. Lucas and H.-S. Oh :*The Method of Auxiliary Mapping for the Finite Element Solutions of Elliptic problems Containing Singularities* , J. Comp. Physics 108 (1993) 327-342.

[34] L. Marcinkowski: *Motar element method for some discretizations of a plate problem,* Tech. Report RW99-13 61, Institute of Applied Mathemtics and Mechanics, Warsaw Univ, 1999.

[35] J. M. Melenk, I. Babuška :*The partition of unity finite element method:Theory and application* , Comput. Methods Appl. Mech. Engr. 139 (1996) 239-314.

[36] *Meshfree Methods for partial Differential Equations I,* Lect. Notes in Compu. Science and Engr. 57, Edited by Griebel, M., Schweitzer, M.A., Springer 2007.

[37] *Meshfree Methods for partial Differential Equations III,* Edited by Griebel, M., Schweitzer, M.A., Lect. Notes in Compu. Science and Engr. 26, Springer 2003.

[38] Y. X. Mukherjee and S. Mukherjee: *Boundary Node method for potential problems,* Int. J. Numer Meth. Eng. 40 (1997) 797-815.

[39] H.-S. Oh, I. Babuška: *The Method of Auxiliary Mapping For the Finite Element Solutions of Plane Elasticity Problems Containing Singularities,* J. of Computational Physics, 121, pp. 193-212 (1995).

[40] H.-S. Oh, C. Davis, J. G. Kim, and Y. H. Kwon: *Reproducing Polynomial Boundary Particle Methods for Numerical Solutions of Boundary Integral Equations,* Computational Mechanics, 48 (2011) 27-45.

[41] H.-S. Oh, J. W. Jeong, and W.T. Hong: *The generalized product partition of unity for the meshless methods,* J. Compu. Phys. 229, (2010) 1600-1620.

[42] H.-S. Oh, J.W. Jeong: *Almost Everywhere Partition of Unity to deal with Essential Boundary Conditions in Meshless Methods,* Comput. Methods Appl. Mech. Engrg. 198 (2009) 3299-3312.

[43] H.-S. Oh, J. W. Jeong : *Reproducing Polynomial (Singularity) Particle Methods and Adaptive Meshless Methods for Two-Dimensional Elliptic Boundary Value Problems,* Comput. Methods Appl. Mech. Engrg. (2008).

[44] H.-S. Oh, J. G. Kim, W.T. Hong *The Piecewise Polynomial Partition of Unity Shape Functions for the Generalized Finite Element Methods,* Comput. Methods Appl. Mech. Engrg. 197 (2008) 3702-3711.

[45] H.-S. Oh, J.G. Kim, J.W. Jeong :*The Closed Form Reproducing Polynomial Particle Shape Functions for Meshfree Particle Methods*, Comput. Methods Appl. Mech. Engrg. 196 (2007) 3435-3461.

[46] H.-S. Oh, J. G. Kim, J.W. Jeong: *The smooth piecewise polynomial particle shape functions corresponding to patch-wise non-uniformly spaced particles for meshfree particles methods,* Comput Mech 40 (2007) 569-594.

[47] H.-S. Oh, J.W. Jeong, J. G. Kim: *The Reproducing Singularity Particle Shape function for problems containing singularities,* Comput Mech 41 (2007) 135-157.

[48] H.-S. Oh, J.W. Jeong, W. T. Hong: *Genealized product Partition of Unity for the meshless methods,* J. Comput. Phys, 229 (2010)1600-1620.

[49] E.T. Ong, K. M. Lim: *Three-dimensional singular boundary elements for corner and edge singularities in potential problems,* Eng. Anal. Bound. Elem. 29 (2005) 175-189.

[50] J. N. Reddy, Theory and Analysis of elastic plates and shells, second edition, 2007, CRC press.

[51] J. B. Rosser and N. Papamichael, *A power series solution of a harmonic mixed boundary value problem*, MRC Technical Summary, Rept. 1405, University of Wisconsin, 1975.

[52] T. Stroubolis, K. Copps, and I. Babuska: *Generalized Finite Element method*, Comput. Methods Appl. Mech. Engrg., 190 (2001) 4081-4193.

[53] T. Stroubolis, L. Zhang, and I. Babuska: *Generalized Finite Element method using mesh-based handbooks:application to problems in domains with many voids*, Comput. Methods Appl. Mech. Engrg., 192 (2003) 3109-3161.

[54] B. Szabo, I. Babuska, Finite Element Analysis, John Wiley, 1991.

[55] R. Szilard: Theories and Applications of Plate Analysis, John Wiley, 2004.

[56] S. Timoshenko, S. Woinowsky-Krieger, Theory of Plates and Shells, McGraw-Hill, 1959.

[57] A. Toselli, O. Widlund, Domain Decomposition Methods- Algorithms and Theory, Springer 2005.

[58] C. Xenophontos, M. Elliotis, G. Georgiou : *A singular function boundary integral methods for Laplacian problems with boundary singularities,* SIAM J. Sci. Comput. 28 (2006) 517-532.

[59] B. I. Yun: *The boundary element method for potential problems with singularities,* J. KSIAM, 3 (1999) 17-28.